Technische Universität München

Fakultät für Chemie

Lehrstuhl für Physikalische Chemie

Linear and nonlinear chiroptical activity

in the gas phase and at surfaces

Farinaz Mortaheb

Abstract

Chirality plays a pivotal role in nature and especially in human beings' life. Hence, a profound understanding of chiral systems is essential. The human body consists of chiral systems which interact and react to the foreign chiral systems with the proper configurations. Numerous drugs in the pharmaceutical industry are also chiral and produced in racemic mixtures. Such mixtures need to be enantiomerically purified in order to obtain the correct enantiomer for specific purpose and usage. The alternative to produce enantiopure substances is asymmetric catalysis, where the catalytic reaction is in favour of one of the enantiomers. The importance of high-quality enantiopure products leads to the demand for fast and sophisticated analytical methods with high enantioselectivity. The analysis methods are usually based on circular dichroism (CD) or optical rotatory dispersion (ORD). These methods are well-established for the solutions, where solvents' influence is inevitable. However, analysis of the volatile chiral products is possible in the gas phase by means of a mass spectrometer analyzer via circular dichroism - resonance-enhanced multiphoton ionization – mass spectrometry (CD-REMPI-MS).

In this thesis, CD-REMPI-MS is used to analyze the vibronic transitions of chiral molecules as well as the role of vibrational modes in anisotropy factors. Furthermore, in order to inspect the non-volatile chiral molecules, a laser desorption source was developed, where a laser beam was used to bring the molecules into the gas phase to be analyzed. The adapted set-up is now even capable of simultaneously analyzing volatile and non-volatile chiral molecules in the gas phase.

Moreover, enantiospecific desorption by circularly polarized light was demonstrated. The proof of principle of enantiospecific desorption was shown with the help of the nonlinear chiroptical technique, second harmonic generation-circular dichroism (SHG-CD). The demonstrated method holds great potential for the purpose of enantiomeric enrichment in the pharmaceutical industry.

Zusammenfassung

Chiralität spielt eine zentrale Rolle in der Natur und im Leben der Menschen, weswegen ein tiefes Verständnis chiraler Systeme essentiell ist. Der menschliche Körper ist zum Beispiel ein solches chirales System, das auch auf andere äußerliche chirale Systeme reagiert. Viele Medikamente aus der pharmazeutischen Industrie beinhalten chirale Substanzen, die erst als racemische Mischung hergestellt werden. Aus diesen Mischungen muss anschließend das richtige Enantiomer gewonnen werden. Die Alternative zur Herstellung von enantiomerenreinen Substanzen ist die asymmetrische Katalyse, bei der während der katalytischen Reaktion ein Enantiomer favorisiert wird. Die Bedeutung von hochqualitativen, enantiomerenreinen Substanzen führt zur Nachfrage nach schnellen Analysemethoden mit einer hohen Selektivität für Enantiomere. Solche Analysemethoden basieren im Allgemeinen auf dem Zirkulardichroismus (CD) und der optischen Rotationsdispersion (ORD). Allerdings sind diese weitestgehend in Lösung etabliert wo der Einfluss des Lösungsmittels unvermeidbar ist. Dennoch ist die Analyse von flüchtigen chiralen Produkten in der Gasphase mittels Zirkulardichroismus-Resonanzverstärkter Mehrphotonenionisation-Massenspektrometrie (CD-REMPI-MS) möglich.

In dieser Doktorarbeit wurden die vibronischen Übergänge von Chiralen Molekülen und ihre Rolle für den Anisotropiefaktor untersucht. Außerdem wurde eine Laserdesorptionsquelle entwickelt, um nichtflüchtige Moleküle studieren zu können. Die Moleküle werden dabei mittels eines Lasers in die Gasphase überführt. Der erweiterte Aufbau ist nun sogar in der Lage, flüchtige und nichtflüchtige Moleküle gleichzeitig zu untersuchen.

Darüber hinaus wurde zum ersten Mal die enantiospezifische Desorption durch zirkular polarisiertes Licht gezeigt. Dieser Grundsatzbeweis der enantiospezifischen Desorption wurde mittels der nichtlinearen chiroptischen Technik „second harmonic generation-circular dichroism" (SHG-CD) gezeigt. Die vorgestellte Methode besitzt zudem großes Potential in Hinsicht auf die Anreicherung eines Enantiomers für die pharmazeutische Industrie.

Acknowledgement

I would like to express my sincere gratitude to my advisor Prof. Ueli Heiz for his support of my Ph.D. study and his guidance. He showed great kindness and care throughout my study and research. Besides my advisor, I would like to thank Dr. Aras Kartouzian, my mentor, whose help and supervision lit up my way within my study. I could not have imagined myself to have any better mentor for my Ph.D. study. I am grateful for all the discussions we have had to push the project to the fruitful end. I also would like to thank Prof. Ulrich Boesl for all the kind words and scientific discussions. Although he was retired his passion for science still goes on.

I also want to thank my predecessor Jörn Lepelmeier for all his efforts to teach me what he knew and make the work environment a friendly place for a newcomer. By that, I would like to thank my lab mate Alexander Von Weber, who helped me whenever I needed a hand to handle the heavy stuff. His joyful nature was lightening the tiredness of the work. I also want to mention Matthias Jakob, the other lab mate of mine for his presence and his stories which really brought so many laughs to our small subgroup. I am thankful to all the students who have been working in our subgroup for their help.

I am very thankful towards Heiz' group members with whom I shared a lot of memorable moments and laughter. I also want to thank electronic and mechanical workshops for all their help and favors and also for fulfilling my urgent and sudden requests, kindly.

I would like to show my gratitude to my collaborators who helped me throughout my thesis and made a nice and fruitful collaboration possible, Katrin Oberhofer, Dr. Hristo Iglev, Prof. Reinhard Kienberger and Prof. Fabrizio Santoro.

Last but not least, I would like to thank my best friend ever, Mandana Moshrefzadeh, who was by my side like a family during all the sad and happy moments of my life.

I would like to express my special and huge gratitude to my beloved family, my mom, dad, siblings and late grandparents. Their trust and supports were a great deal and I could not have achieved what I have today without their sacrifices, love and supports, although they were far away from me.

Table of Contents

1. Introduction

The word 'Chirality' was derived from the Greek word for hand in the late 19th century and is a geometrical property which describes handedness. A molecule is called chiral when it cannot be superimposed on its mirror image, and the molecule and its mirror image are called enantiomers (*1, 2*). It took almost a century after the discovery of chirality, to recognize its significance in the pharmacy, agriculture, chemical industry and explicitly nature (*3*). The human body contains many homochiral compounds which makes it a spectacular chiral selector (*4*). The receptor sites in the human body interact with molecules possessing the compatible handedness. Consequently, a great number of chiral molecules is used in drugs (*3*). Even though the opposite enantiomers have similar physical and chemical properties, they interact differently with chiral systems and for example, undergo different metabolism in the human body. Due to this fact, one enantiomer can have a healing effect, whereas, the other one may show severe side or toxic effects. For instance, Dopa or dihydroxyl-3,4phenylalanine is one of the molecules that has a toxic effect just in one of the enantiomers. For many years, a racemic mixture of L/D-Dopa was used in the drug industry, which is a 50:50 mixture of the two enantiomers. This led to the side effects such as vertigo, headache, and abdominal pain caused by D-Dopa (*5*). This indicates the drastically increasing demands for enantiopure compounds instead of the racemic mixtures, especially in the pharmaceutical industry. But until the early 1990s, the products of the syntheses were still racemic and the demands for enantiopure products kept increasing, over the decades (*1*).

On that account, the developments of the efficient chiral separation, enantiomeric enrichment and single enantiomer synthesis methods were undisputable. An alternative and remarkable development was the synthesis of chiral compounds via asymmetric catalysis, where, a chiral man-made catalyst is used to accelerate the reactions which result in enantiomeric excess (ee) of the favorable enantiomer (*3, 6*). The early achievement of such an approach was the synthesis of L-Dopa with the DIPAMP-Rh catalyst via asymmetric hydrogenation, reported by the group of Knowles (*7*). Although most of the asymmetric catalysis synthesis is homogenous, there have been recently numerous studies on the heterogeneous asymmetric catalysis because of their advantages over the homogeneous counterpart including better efficiency, selectivity and no need for recycling (*8*).

Owing to the great importance of the enantiopurity of the compounds, appropriate analysis methods are indispensable in order to qualify the enantioselectivity of the asymmetric heterogeneous catalysts and the enantiomeric excess (ee) of the products. Most of the enantioselective techniques are based on circular dichroism (CD) (*9*) as well as optical rotatory dispersion (ORD) (*10*). CD, itself, results from a different interaction of the opposite enantiomers with different handedness of circularly polarized light. This phenomenon can be combined with different spectroscopic techniques, such as resonance-enhanced multiphoton ionization - mass spectrometry (REMPI-MS) (*11-13*) which is performed in the gas phase. Therefore, CD-REMPI-MS is an ideal method to analyze the volatile products of the heterogeneous asymmetric catalysis, as shown in Fig.1a. In order to study non-volatile products, the molecules are brought into the gas phase by laser desorption (*14-17*), as illustrated in Fig.1c1 and c2. In this thesis, the volatile and non-volatile chiral molecules are studied by means of CD-REMPI-MS in combination with laser desorption. This work also demonstrates the potential of these techniques as the enantiosensitive analytical tools in the heterogeneous asymmetric catalysis.
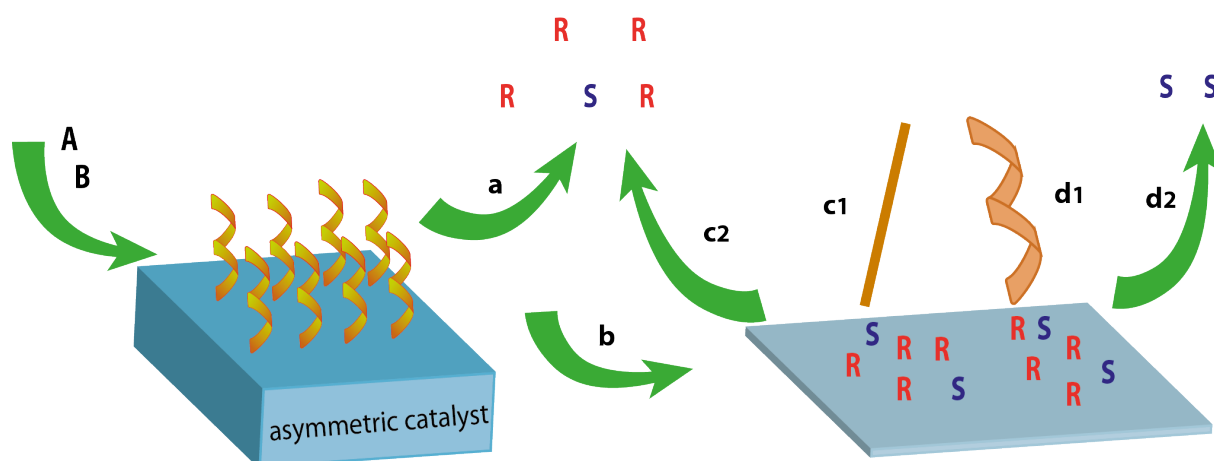
Figure 1- Enantiopure synthesis via the asymmetric catalysis. A and B are the educts introduced to the asymmetric catalyst. After the reaction, a) volatile products are analyzed in the gas phase via CD-REMPI-MS, and b) non-volatile products are brought into the gas phase by the laser (c1) and analyzed in the gas phase via CD-REMPI-MS (c2). Enantiospecific desorption by circularly polarized light (d1) removes one of the enantiomers in the mixture (d2).

A variety of methods such as chiral separation and enantiomeric enrichment can be applied for a further enantio-purification of the products of the asymmetric catalysis or the racemic mixtures in the case of common symmetric catalysts (*18*). In this work, a new technique for purification of a mixture of chiral molecules is suggested which is based on laser desorption from the surface

and called enantiospecific desorption. In this method, circularly polarized light is used to enantioselectively remove one of the enantiomers in the mixtures which results in enantiomeric enrichment as shown in Fig.1d1 and d2. The optical activity evolution at the surface is measured by means of the nonlinear chiroptical technique, second harmonic generation-circular dichroism (SHG-CD).

2. Introduction into the theory

In 1848, the French scientist, Louis Pasteur discovered handedness or chirality while working with sodium ammonium tartrate. He manually discriminated between two enantiomers of the sodium ammonium tartrate crystals. Later, he found out that these enantiomers in solutions are rotating the plane of the linearly polarized light in opposite directions (*1, 19*). The only factor which separates enantiomers is their spatial arrangement. The spatial configuration of chiral molecules can be realized with the help of X-ray crystallography diffraction (*20*), whereas, their optical activities can be determined by ORD (optical rotatory dispersion) and CD (circular dichroism). In the following section, the latter one will be explained in more detail.

2.1.   Circularly polarized light and circular dichroism

The light is an electromagnetic wave formed of electric and magnetic fields. These fields are, perpendicular to each other and to the propagation axis. They propagate with the same speed and in the same direction. Since the electric field is a vector quantity, the route on which the tip of the vector of the electric field travels, shows the polarization of the light. In the case of linearly polarized light, the vectors of the electric field oscillate around the propagation axis and in the same plane. Whereas in the case of circularly polarized light, the magnitude of the field remains constant, but the end of electric field arrow draws a helix about the propagation direction.

Normally, the light generated from the laser is polarized. The polarized light consists of two linearly polarized components in the x- and y-directions, whereas the propagation is considered in z-direction. Circularly polarized light is created, where the magnitude of the components are equal (i.e. $E_{0x} = E_{0y} = E_0$), but they have a relative phase shift of $\pm 90°$, which is equal to $\pm \pi/2$ (*21*).

For - $\pi/2$, the equations of two components of the polarized light is described as:

$$\vec{E}_{x(z,t)} = \hat{\imath} \, E_0 \cos(Kz - \omega t) \tag{1}$$

$$\vec{E}_{y(z,t)} = \hat{\jmath} \, E_0 \cos(Kz - \omega t - \frac{\pi}{2}) \tag{2}$$

Where ω is the angular frequency and K is the wavenumber. E_y can be evolved to

$$\vec{E}_{y(z,t)} = \hat{j}\, E_0 \left[\cos(Kz - \omega t)\cos\frac{\pi}{2} + \sin(Kz - \omega t - \frac{\pi}{2})\,\sin\frac{\pi}{2}\right] \tag{3}$$

and consequently,

$$\vec{E}_{y(z,t)} = \hat{j}\, E_0 \sin(Kz - \omega t) \tag{4}$$

Thus, the E_x and E_y (E) are summed up as

$$E = E_0[\hat{i}\,\cos(Kz - \omega t) + \hat{j}\,\sin(Kz - \omega t)] \tag{5}$$

In the case of $\pi/2$, all the calculations need to be modified, which ends in:

$$E = E_0[\hat{i}\,\cos(Kz - \omega t) - \hat{j}\,\sin(Kz - \omega t)] \tag{6}$$

The handedness of the circularly polarized light is defined, corresponding to the sign of the phase shift. A virtual viewer should look against the propagation direction of the light (z), where the initial point is the light source and the terminal point is the person's eye. For - $\pi/2$ phase shift, the right-handedness in accordance with clockwise rotation can be determined, whereas for $\pi/2$ it is vice versa (*21, 22*).

In order to generate circularly polarized light, linearly polarized light needs to pass through a birefringent material. There, different components of light travel with different speeds, based on their axes along the fast and slow axes of the birefringent materials. The slow and fast axes denote the larger and smaller refractive indices of the birefringent material, respectively. A quarter wave plate (QWP) and a photo-elastic modulator (PEM) are examples, one can use to create circularly polarized light. A quarter wave plate is made of uniaxial crystal, which has birefringent properties. If linearly polarized light (electric field plane) enters the optics with 45°, corresponding to the fast and slow axes of the plate, it will be converted to circularly polarized light. Rotating the QWP by 90° will give the other handedness of the circularly polarized light. PEM is a transparent glass which is mechanically compressed or stretched along an axis. Thus, different refractive indices will be constructed along the axis, while the refractive index of the perpendicular axis of the glass body stays constant. Consequently, the components of the electric field travel along the two axes of PEM with different speeds, resulting in a phase shift. In case

of correct calibration, the phase shift would be equal to $\pm\pi/2$ and linearly polarized light is converted to circularly polarized light (*23*).

In spectroscopy, interaction happens between a molecule and a photon at a time. The molecules absorb, emit or scatter the photons. In the case of absorption, absorbance is defined regarding the Beer-Lambert law as:

$$A = \log_{10}(\frac{I_0}{I}) = \varepsilon C l \tag{7}$$

I_0 and I denote the intensity of the incident and the transmitted light, respectively. C is the concentration, l is the length or thickness of the sample through which light passes and ε is the extinction coefficient.

Absorption of an electromagnetic field by a molecule causes a transition between two states of the molecule. The direction of the net linear displacement of charges defines the polarization of the transition. Both the polarization and intensity of the transition are described by the transition momentum. The maximum absorption probability occurs when the transition momentum and the electric field are parallel. In the case of chiral molecules, since there exists no reflection plane, thus the rearrangement of the charges will not have that plane either. Moreover, the motion of the electrons forms a helix, by considering the fact that circularly polarized light traces the helices, one can realize that the behavior of chiral molecules towards left and right circularly polarized light will be different.

Circular Dichroism (CD) is defined according to the responses of molecules to left and right circularly polarized light. One can say:

$$CD = A_l - A_r \tag{8}$$
$$\Delta A = (\Delta\varepsilon) C l \tag{9}$$
$$\Delta\varepsilon = \varepsilon_l - \varepsilon_r \tag{10}$$

Where, A_l and A_r denote the absorptions of molecules when the incident light is left circularly polarized and right circularly polarized, respectively. A chiral molecule can have both negative and positive CD values for the different electronic transitions, influenced by the electron redistribution of different handedness. Normally, CD spectrometers illustrate CD spectra in units of ellipticity, θ, in millidegrees as a function of the wavelength (*24*). Thus,

$$CD = \Delta A = A_l - A_r = \frac{4\pi\theta \ (degrees)}{180 \ln 10} = \frac{\theta \ (millidegrees)}{32,982} \qquad (11)$$

Optical Rotation is another effect which may occur during the interaction between the light and chiral molecules. When a linear laser beam goes through a chiral system, the plane of the light is rotated. Optical rotation is described as the difference between refractive indices of left and right circularly polarized light, n_L and n_R, respectively. Optical Rotatory Dispersion (ORD), is the wavelength-dependent term of the optical rotation. Both CD and ORD provide information correspond to the ground state conformation of chiral molecules (*25*).

The interest in CD is coming from the fact that a better comprehension of the biological and several non-living systems, which are chiral and oriented, is essential. The innovative researches of Rosenfeld, Moffitt and Nakanishi (*26, 27*) indicated CD spectroscopy as a proper technique, by which the molecular secondary structural features can be investigated in a solution. The conventional CD spectra are based on the linear absorption (one-photon absorption) and subsequent response of chiral molecules. This response is observed often in the near and far UV region of the spectrum. A detailed description of this phenomenon embeds in the structure of chiral molecules. As mentioned before briefly, the helical motion of the displaced charges in chiral molecules, which is caused by the electromagnetic field, induces a magnetic transition dipole moment ($\vec{m}$) in molecules additional to the usual electric transition dipole moment ($\vec{\mu}$). Generally, both electric and magnetic dipole transition moments between the states of the chiral molecules play roles in the optical respond of chiral molecules (*28*). The fundamental theory behind the CD effect, lies in the rotation strength of the electronic transitions, calculated as:

$$R = Im \ \vec{\mu} \cdot \vec{m} \qquad (12)$$

Which shows the interaction between electric ($\vec{\mu}$) and magnetic ($\vec{m}$) dipole transition moments in molecules (*27, 29*). From experimental spectra, R can be estimated by getting an integral over the band in the CD spectra.

The traditional CD spectra are normally recorded in solutions, whereby the interactions with solvents affect the CD signal of the investigated chiral molecules. The solution shows the CD effects for the specific combination of the components of electric and magnetic dipole transition moments between the ground and excited states of the molecules. Such CD effects are not strong. Nonlinear response expands these spectroscopy methods so that chiral molecules whose linear

CD is small can yield greater nonlinear optical activity. Processes such as SHG-CD and SFG-CD as well as two-photon absorption CD (2PA-CD) have been used for that matter (*28, 30*). Combination of CD and REMPI-MS is a method which is applied in the gas phase and gives information close to 2PA-CD. Thus, this method holds enhanced chiroptical detection and is a suitable method to investigate the optical activity of volatile chiral molecules in the gas phase. The best example of such molecules is products of the heterogeneous asymmetric catalysis.

2.2. Circular dichroism - Resonance-enhanced multiphoton ionization (CD-REMPI)

As mentioned in the introduction, in the pharmaceutical industry, it is substantial to use pure enantiomers. To produce enantiomerically pure substances, asymmetric catalysis was developed and especially, homogeneous asymmetric catalysis has been well established. Although homogeneous asymmetric catalysis yields high enantioselectivity and catalytic activity, it possesses a few drawbacks, such as the recovery of the catalyst, high costs of the chiral catalyst and product contamination. Thereby, the heterogeneous asymmetric catalysis seems to be a promising substitution. Hence, the number of researches on such systems has been growing, rapidly (*31*). To analyze products of the heterogeneous asymmetric catalysis fast, sensitive and versatile techniques which may be applicable under various conditions are essential. The combination of CD and REMPI-MS is one of those methods to observe the optical activity of volatile products in the gas phase (*11-13*). CD-REMPI-MS is a highly selective analytical method which will be discussed in more detail, in this section.

- *Resonance-enhanced multiphoton ionization (REMPI)*

Resonance-enhanced multiphoton ionization (REMPI), has become one of the most well-established methods for the investigation of molecules in the gas phase. The achieved spectral information from the isolated molecules not only paves the path towards a better interpretation of intrinsic molecular properties but also supports the theoretical predictions (*32*).

A century ago, the ionization of an atom was considered to be a single step, through which the atom absorbs a photon with an energy higher than its ionization energy. Later on, the idea of the photoionization changed, due to the theoretical prediction and the application of laser in the ionization, so that the multiphoton ionization became the favorable process rather than one photon ionization (*33, 34*).

8

In 1931, Geoppert-Mayer suggested two-photon transition as the ionization process. However, this process possesses a small cross-section and to prove it experimentally one needed powerful radiation, which was not available at that time. Only after the invention of the laser, it became feasible to study multiphoton transitions in atoms and molecules (*35*). The common source for photoionization used to be Nd: YAG laser with 266 nm wavelength and 4.6 eV energy, which is generally not sufficient to overcome the ionization energy of molecules (for most of molecules ionization potentials are between 7 to 13 eV). Thus multiphoton ionization seemed to be an answer to the ionization process (*36, 37*).
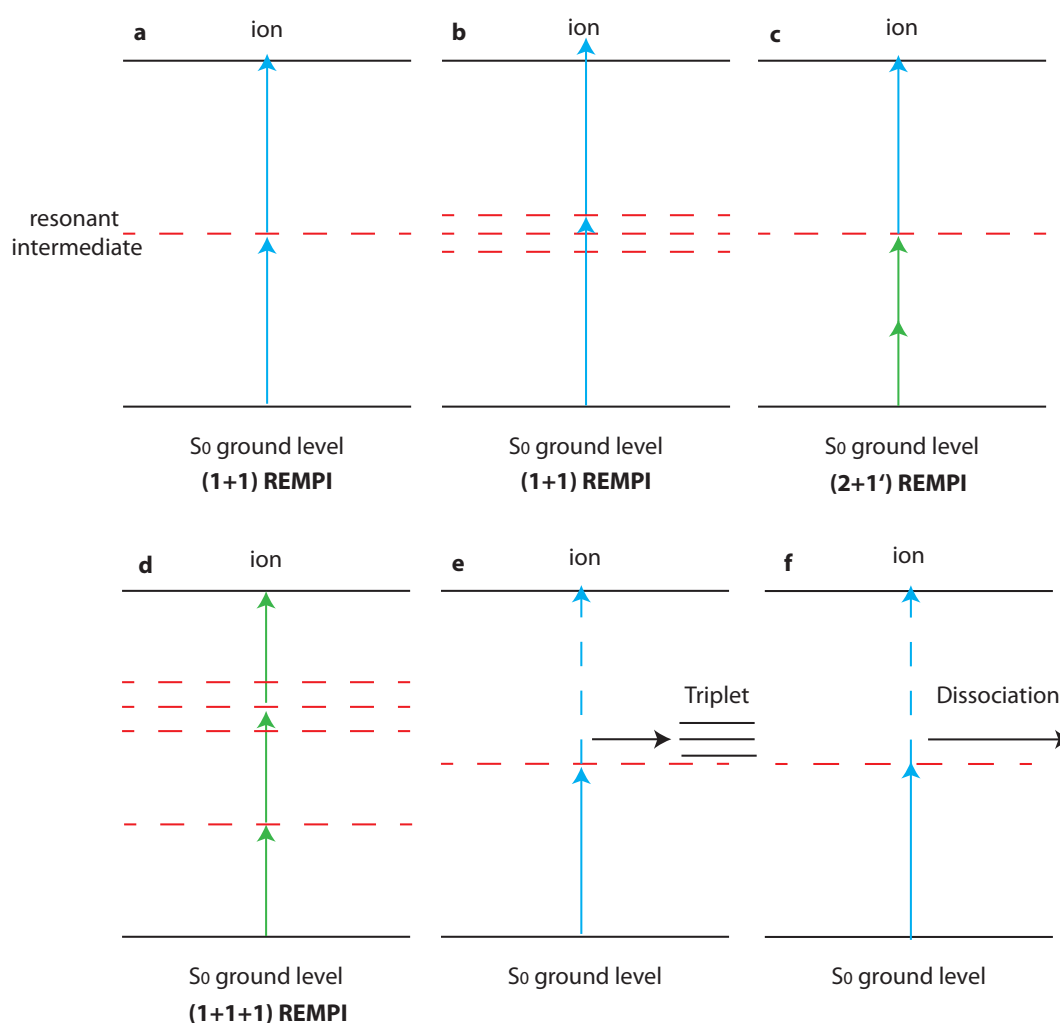

Figure 2- Various REMPI processes.

In order to perform REMPI, molecules need to absorb at least two photons. In REMPI, the intermediate states of the molecules, normally (poly) aromatic, are involved for the ionization

process, thus the ionization is resonant. In Fig.2, some of the schemes for ionization by (n+m) REMPI are depicted, where n and m represent the number of photons for excitation to the excited state and ionization steps, respectively. REMPI has been performed either with one colour (Fig.2a,b,d) or two colours (Fig.2c). In the former case, photons for the excitation and ionization steps are identical, whereas in the latter one they possess different wavelengths. (1+1) REMPI stands for one colour two photons ionization process (Fig.2a,b), through which one photon excites the molecule to the resonant intermediate states and the other one does the ionization process. (2+1′) REMPI denotes the ionization process where the molecule requires two photons with the same energy for the resonant excitation. From there, another photon with different energy is absorbed to complete the ionization process (Fig.2c). In this case, the ionization efficiency is lower, because of the non-resonant excitation to the virtual state with a very short lifetime of $< 10^{-15}$ s. For (1+1+1) REMPI (Fig.2d), where three photons with the same energies are required for the process, large laser pulse energies are essential in order to have high ionization rates. During (n+m) REMPI, if the excited molecule is depopulated (Fig.2e) or dissociated (Fig.2f) into a triple state at the intermediate state, the ionization efficiency will be reduced (*37-40*). On that account, molecules, with groups which go through depopulation process at the intermediate states such as chlorinated and brominated groups on the aromatic rings, yield less effective ionization compared with their unsubstituted counterparts. The efficiency of the non-resonant ionization compared to a resonant one is drastically lower, because of a low cross-section of the non-resonant ionization. Therefore, the absorption-excitation spectrum of an intermediate state in the molecule can be understood by the ionization cross-section. In order to have a proper understanding of the ionization process, knowledge about the electronic levels of the neutral molecules is essential.

The synergy between REMPI, supersonic beam and the mass-selective detector has been a great step in the field of analyzing volatile chiral molecules. The first REMPI-MS was performed on polyatomic molecular systems, in 1977. Being a soft photoionization method yielding no or small fragmentation makes REMPI a very efficient and precise method in combination with mass spectrometry. The laser spectroscopy techniques of large molecules in supersonic beams considers a unique method for investigation of energetics and excited state dynamics of isolated molecules (*41, 42*). Moreover, a proper wavelength choice for REMPI can lead to a selective ionization (*34, 37*).

The time-dependent perturbation theory explains the multiphoton ionization process in a better way by using the electric dipole approximation of the light field. First, some parameters should be defined; such as α, β, κ_r, κ_{nr} and I. α and β stand for the absorption rate constant and ionization absorption rate, respectively. If the multiphoton ionization consists of (n + m) photons, then n denotes the index of α, α_n, whereas m shows the number of photons used for the ionization step, therefore, β_m. The constants κ_r and κ_{nr} illustrate the one-photon spontaneous emission rate and the irreversible decay processes of the intermediate state, respectively. The former one, κ_r, is normally negligible compared to the other rates. The latter one includes internal conversion, intersystem crossing and dissociation. I is the light intensity, which together with the photon absorption cross-section (σ_i) provides α, β, via the following equations:

$$\alpha = \sigma_n \, I^n \tag{13}$$

$$\beta = \sigma_m \, I^m \tag{14}$$

Figure 3- Excitation and ionization steps of REMPI.
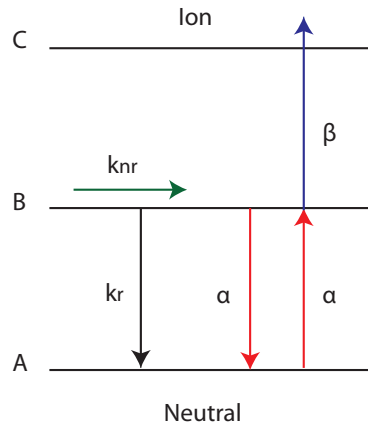
Now, by considering the excitation scheme for REMPI presented in Fig.3, the rate equation for the depopulation of the neutral ground state A, the population of the intermediate state B and the ion yield C, would be (*38*):

$$\frac{dA}{dt} = -\alpha \, A + (\alpha + \kappa_r)B \tag{15}$$

$$\frac{dB}{dt} = \alpha \, A - (\alpha + \kappa_r + \kappa_{rn} + \beta)B \tag{16}$$

$$\frac{dC}{dt} = \beta B \tag{17}$$

The ion concentration created from an initial ground state concentration of A_0, by a square laser pulse with the width of t_L (43), can be calculated via

$$C = \frac{\beta A_0}{\beta + \kappa_{rn}} \left[1 + \frac{L}{K - L} e^{-Kt_L} - \frac{K}{K - L} e^{-Lt_L} \right] \tag{18}$$

Where K and L are:

$$K = \frac{(2\alpha + \kappa_r + \kappa_{rn} + \beta) + \sqrt[2]{(2\alpha + \kappa_r + \kappa_{rn} + \beta)^2 - 4\alpha (\beta + \kappa_{rn})}}{2} \tag{19}$$

$$L = \frac{(2\alpha + \kappa_r + \kappa_{rn} + \beta) - \sqrt[2]{(2\alpha + \kappa_r + \kappa_{rn} + \beta)^2 - 4\alpha (\beta + \kappa_{rn})}}{2} \tag{20}$$

Regarding one intermediate state ionization, by assuming very low laser energy with α, β, but also κ_r and $\kappa_{nr} \ll 1/t_L$, C would be:

$$C = \frac{\alpha \beta A_0 t_L^2}{2} \tag{21}$$

In an exceptional case that $\kappa_{nr} \gg 1/t_L$, Eq.21 would be changed to:

$$C = \frac{\alpha \beta}{A_0 k_{rn} t_L} \tag{22}$$

In case of large laser intensity and α, $\beta \gg 1/t_L$, C would be calculated as:

$$C = \beta / (\beta + \kappa_{nr}) A_0 \tag{23}$$

Now, if (2 +1) photons ionization happens, α is small and β is large, depending on κ_{nr}, two equations can be derived; either

$$C = \alpha \beta / (\beta + \kappa_{nr}) A_0 t_L \text{ for } \kappa_{nr} \gg 1/t_L \tag{24}$$

or,

$$C = \alpha A_0 t_L \text{ for } \kappa_{nr} \ll 1/t_L \tag{25}$$

12

In a report by Boesl (*38*), they showed that the experimental values of cross-sections for multiphoton ionization are in accordance with the above formulas. For that matter, they used a number of organic molecules such as benzene, toluene, aniline, naphthalene and thiophene. One should be aware that only molecules with a suitable rotational population for the laser wavelength can absorb and overcome the ionization barrier. Due to the fact that the rotational envelope of an absorption band is a few cm^{-1}, and pulsed lasers have a bandwidth of 1cm^{-1} or less, therefore not all the neutral molecules are ionized. By having the supersonic expansion, these rotational envelopes are becoming narrower which results in a larger ion yield.

The laser intensity plays a crucial role in multiphoton ionization. Energies which are above the saturation of the absorption rate constant and ionization absorption rate lead to fragmentation rather than the increment in the ion yield. However, there are some exceptions for this; For example, in case of a non-radiative process (K_{nr}), higher intensities help with overcoming the latter process which depopulates the intermediate states (B). For a reasonable laser intensity, i.e. below the saturation of the resonant transition, the ion yield for (1+1) REMPI can be approximated as:

$$[M^+]\big/_{[M]} = \frac{1}{2}\,\sigma_1\sigma_2\,(^{P_{laser}}\big/_{\sigma_{laser}})^2 \tag{26}$$

Where, $[M^+]$ and $[M]$ are the number density of ions and molecules, respectively. σ_1 and σ_2 are the absorption cross-sections of the excitation and ionization, respectively. P_{laser} is the number of photons per laser pulse, while σ_{laser} stands for the laser beam cross-section (*44*).

The very high ion density has some disadvantages, especially if it is combined with TOF. This high density can lead to space charge effects, which induce large initial kinetic energy in ions and, consequently, decrease the mass resolution. In addition, space charge effects disturb the path of the ions and they follow variant trajectories. Finally, multiphoton ionization is generally a soft ionization technique if a low laser intensity is used (*15, 38*).

The combination of REMPI, cooled molecular beam (supersonic jet) and mass spectrometer provides the possibility to investigate separated single vibronic transitions. Due to the importance of the supersonic expansion process, this topic will be discussed in the following section.

- *Supersonic expansion*

As mentioned briefly before, molecular beams possess properties that make them suitable for molecular structure studies in the gas phase, especially in combination with REMPI. Having a cooled molecular beam avoids thermal dissociations as well as makes it possible to obtain high-resolution spectra. The supersonic expansion provides a cooled molecular beam with a narrow velocity distribution and a sufficiently low density, which gives a smaller number of collisions compared to the effusive beam (ca. 3:1) (*41, 45*).

The supersonic expansion can be achieved by a general valve. To explain the supersonic expansion, three phases can be considered. The first phase is before the expansion where carrier gas and molecules are in thermodynamic equilibrium in the gas line. The gained equilibrium is essential in order to have a well-defined temperature and pressure. The next phase is during the adiabatic expansion, where, no energy is exchanged between the gases and the environment. That demands sufficient pressure difference before and after the nozzle (valve). The last phase is after the expansion, where particle-particle collision is hindered, and a steady state is reached. Therefore, molecules are in the well-defined quantum state (generally at the lowest energy possible) and flying with a narrow velocity distribution as well as adequately low density which prevents any intermolecular interactions (*41, 46*).

To compare the velocity distribution between effusive and supersonic beam, one can consider the study on He gas, published by Smalley et al. (*41*). In the case of an effusive beam, the orifice diameter size (D) of the inlet needle is much smaller than the mean free path (λ_0) of the gas at the pressure P_0 inside the reservoir ($D \ll \lambda_0$). The flow from the effusive inlet is molecular, due to the fact that there are no significant collisions between gas molecules after the orifice. Therefore, the velocity distribution in the molecular beam is the velocity-weighted distribution of the reservoir temperature, and as a result, the distribution of internal molecular states is identical to the states in the reservoir. For the supersonic expansion, the nozzle of the valve (D) is much bigger than the mean free path of the gas (λ_0) at the reservoir pressure of P_0 ($D \gg \lambda_0$). Thus, molecules are going through many collisions while passing the nozzle. After the expansion, the enthalpy associated with all the collisions, converts into the mass flow, so that its velocity (u) increases, while the temperature drops. According to the classical speed of sound, a, (Eq.27), by decreasing T, consequently, a decreases. Therefore, the Mach number (Eq.28), M, increases, which is the ratio of mass flow velocity to the speed of sound.

$$a = \sqrt{\gamma \kappa T / m} \,,\, \gamma = C_p / C_v \tag{27}$$
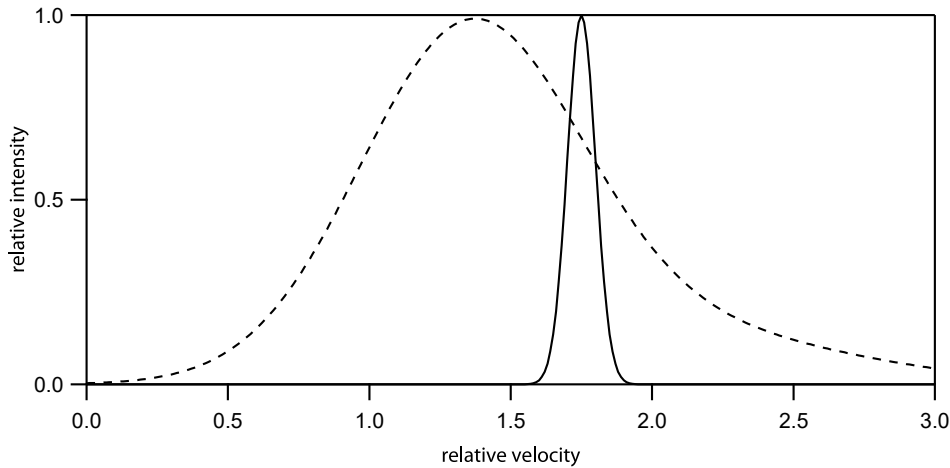
$$M \equiv u/a \tag{28}$$

Figure 4- Velocity distribution in the effusive beam (dashed line) and supersonic jet (solid line).

The velocity distributions behavior of the effusive and supersonic molecular beams for He are illustrated in Fig.4. As already explained, an effusive beam has a velocity-weighted Maxwell-Boltzmann distribution, while a supersonic beam has a velocity distribution in the direction of the mass flow. In the supersonic case, the peak of distribution was shifted to the higher velocity, thanks to the increment in the flow velocity. The width of the velocity distribution shows the discrepancy in the translational temperature for the beams. Since the supersonic beam is cooled, thus the velocity distribution is narrower in contrast to the effusive (*41, 47*).

The first achievement of the supersonic expansion is the cooling of the translational degrees of freedom. Depending on the rate that the equilibrium with the cold translational bath is obtained, the rotational and vibrational degrees of freedom also could be cooled. The rate of equilibrium between translations and rotations is relatively fast, whereas this rate is slower for vibrations and translations. Due to this fact, the rotational degree of freedom becomes cooled, but in the case of vibrational, it cannot be as complete as the rotational one. Thus, the result of the expansion is that the molecules which arrive at the collision-free region will be translationally and rotationally very cold.

Generally, for a supersonically cooled molecular beam, the number of up-taken molecules by the carrier gas is small so that the behavior of the pure gas for the mentioned expansion can be assumed. The question which might arise here is how cold can the molecular beam become? Under certain conditions of an adiabatic reversible flow, such as no shock waves or no shear forces, the expansion can be assumed as isentropic, therefore the isentropic equation of a state of an ideal gas can be applied to the system,

$$\frac{T}{T_0} = \frac{P}{P_0}^{(\gamma-1)/\gamma} = \frac{\rho}{\rho_0}^{\gamma-1} = \frac{1}{1 + \frac{1}{2}(\gamma - 1)M^2} \tag{29}$$

Here, T_0, P_0, and ρ_0 denote temperature, pressure and density in the reservoir, while T, P and ρ are the same parameters in the beam. $\gamma = C_p / C_v$ stands for the heat capacity ratio, and M is the Mach number. With the assumption of a molecular beam as a continuous medium, the Mach number as a function of distance after the nozzle is:

$$M = A\left(\frac{X}{D}\right)^{\gamma-1} \tag{30}$$

X is the distance from the nozzle of the valve, D is the nozzle diameter and A is a constant that is dependent on the heat capacity ratio and for a monoatomic gas is 3.26. As Mach number increases, T, P and ρ are decreasing (*41*).

To estimate the velocity of the pure substances, the conservation of energy will apply to the initial and the final states of the molecular beam. Thus,

$$\langle E\rangle = U_0 + P_0V_0 + \frac{N_A m\langle v_0\rangle^2}{2} = U_1 + P_1V_1 + \frac{N_A m\langle v_1\rangle^2}{2} \tag{31}$$

$\langle E\rangle$ is the average total molar energy; U stands for the internal molar energy, which is related to the random translational and internal motions of the particles. *PV* describes the pressure-volume work happening because of the change of the molar volume V of the fluid at the pressure P. The last part of the equation $(N_A m\langle v\rangle^2)/2$ defines the kinetic energy where $\langle v\rangle$ is a mean velocity, N_A is the Avogadro constant and m is the mass of the particle. Indices 0 and 1 are assigning the parameters to the state of the fluid within the reservoir and the final state of the supersonic beam at a large distance after the nozzle, respectively.

By taking into account the enthalpy definition ($H \equiv U + PV$) and assuming $\langle v_0 \rangle \approx 0$, the mean velocity of the expanded jet can be derived as:

$$\langle v_1 \rangle = \sqrt{\frac{2(H_0 - H_1)}{N_A m}} \tag{32}$$

Here, the change of enthalpy can be described by the help of the isobaric molar heat capacity, $C_P = \left(\frac{\partial H}{\partial T}\right)_P$, therefore, Eq.32 is evolved to:

$$\langle v_1 \rangle = \sqrt{\frac{2C_P(T_0 - T_1)}{N_A m}} \tag{33}$$

Which is valid just for an ideal gas. By introducing $\gamma = C_p / C_v$ and considering $C_p = C_V + R.C_V$, where C_V is heat capacity at a constant volume and R is the gas constant, Eq.33 is converted to:

$$\langle v_1 \rangle = \sqrt{\frac{2R\gamma(T_0 - T_1)}{(\gamma - 1)N_A m}} \tag{34}$$

And the direct influence of the molar isobaric heat capacity is avoided. Thanks to a significant difference between T_1 and T_0 ($T_1 \ll T_0$), one can neglect T_1 and, thus, derive the maximum velocity of the beam from Eq.34. Additionally, both heat capacities are constant for the monoatomic gas, therefore their ratio would be constant, too ($\gamma = C_p / C_v = \frac{5R/2}{3R/2} = 5/3$). Consequently, the final equation for the maximum velocity of an ideal gas flow after an adiabatic expansion, is simplified as:

$$\langle v_{max} \rangle = \sqrt{\frac{5RT_0}{N_A m}} \tag{35}$$

The other factor which plays a role in the cooling process of supersonic expansion is the used carrier gas. Amirav et al. reported that the cooling effect is increasing in the order of He < Ne < Ar < Kr < Xe for the large molecules. They also claimed that the rotational temperature drops to 5-7 K while this value goes to < 50K for vibrational ones at moderate Ar pressure of around 2.4-3.0 Torr. He with a lighter mass needs higher pressure and flow rate to accomplish the same cooling effects by forming four-body collisions compared to Ar (*48*).

- *Circular dichroism – resonance-enhancement multiphoton ionization (CD-REMPI):*

As explained in the previous section, a combination of REMPI, supersonic expansion and mass spectrometry opens up the access to a selective technique, whereby wavelength selectivity and mass selectivity are merged to analyze the molecule precisely in the gas phase. Having CD spectroscopy as the third pillar for such a technique makes it plausible to scope chiral molecules, with higher precision and selectivity, i.e. study the chiroptical activity of chiral molecules. This information in combination with theoretical predictions allows to figure out the absolute configuration of enantiomers. A specific polarization of light can only excite enantiomers with the right orientation in the gas phase; the ones with the same electric dipole moment direction as the electric field vector of the light (*44*). In the case of CD, then both electric and magnetic dipole transition moments will be involved. Having CD spectroscopy in the gas phase, suppresses the drawbacks of using solvents in the conventional methods of CD spectroscopy, while improves the spectral resolution. In order to achieve CD-REMPI, one can convert the linearly polarized light, used for the ionization, with the circularly polarized light.

To estimate CD effects, there exists another quantity, so-called g-value or anisotropy factor or asymmetry factor (*49*), defined as:

$$g = \frac{2\left(\varepsilon^{left} - \varepsilon^{right}\right)}{\left(\varepsilon^{left} + \varepsilon^{right}\right)} = \frac{4R}{D} = 4\frac{m\,\mu\,\cos\theta}{m^2 + \mu^2} \tag{36}$$

Where ε denotes the extinction coefficient, R stands for the rotational strength and D is the dipole strength. m and μ represent magnetic and electric dipole transition moments, respectively, while θ is the angle between them. For CD-REMPI, not absorption but ion current is considered to calculate g-value, thus, the Eq.36 is evolved into:

$$g = \frac{2\left(I^{left} - I^{right}\right)}{\left(I^{left} + I^{right}\right)} \tag{37}$$

In 2006, Loge et al. reported the first CD-REMPI-MS on 3-methyl-cyclopentanone, which was a new technique in enantioselective laser mass spectrometry. They showed that different handedness of circularly polarized light resulting in different ion yields for an enantiomer (*50*). In the same year, Li et al., performed CD-REMPI-MS in a jet on R-(+)-3-methyl-cyclopentanone

(*51*). This study motivated several theoretical works on two-photon CD (TPCD) (*52-54*). Later on, a new method was implemented into the CD-REMPI-MS, so-called twin peak, where a single laser pulse ionizes two molecular clouds and results in two slightly shifted mass spectra (see section 3.1.9) (*55-57*). This method overcame the pulse to pulse fluctuations of the laser. The concept of g-value saturation was also introduced (*56*), there, by increasing the fluence of the excitation laser, the g-value was decreasing (in both two-step and three-step CD-REMPI). That was explained by the saturation of the optical transition, meaning that even weak transitions are saturated, therefore, the small differences of absorption are vanished. Furthermore, Loge and Boesl showed (*58*), that the ionization step plays no role in CD effects, implied by obtaining no significant CD effects when linearly polarized light was used for the excitation steps and circularly polarized light for ionization (see Fig.5). Moreover, it was reported that the TPCD values are greater compared to the one-photon absorption ones (electronic circular dichroism, ECD). There have been many experimental and theoretical studies about this technique (*40, 44, 59, 60*) because of its potential application as a highly sensitive analytical tool.
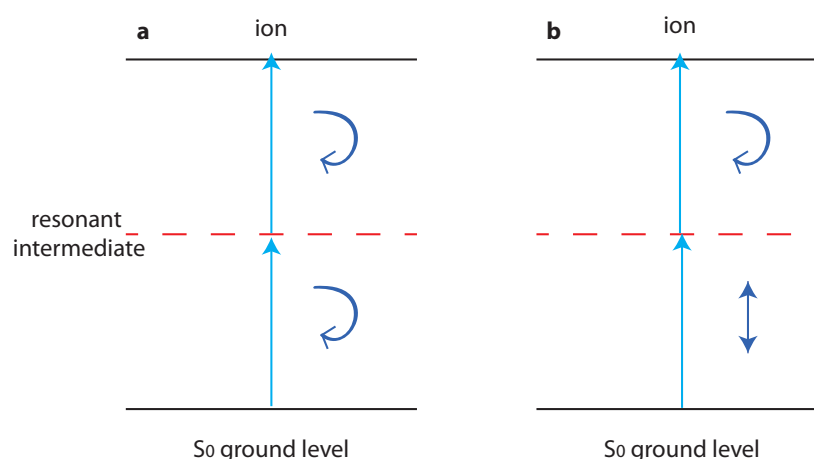

Figure 5- REMPI process. a) using Circularly polarized light for both excitation and ionization steps. b) using linearly polarized light for the excitation step and circularly polarized light for the ionization step.

The recent studies done by Lepelmeier et al., revealed that the rotational branches appeared to have no significant influences on the g-value measured on (deuterated (R)-(+)-3-methylcyclopentanone) [D$_4$]-(R)-(+)-3-MCP via (1+1+1)/(1+1´) CD-REMPI-MS (*12*), while in the other report they showed the significant role of the vibrational modes in obtained CD effects for R-(+)-1-phenylethanol via (1+1) CD-REMPI-MS (*13*). Their experimental and theoretical results showed the involvement of vibrational modes in changing the angle between the electric

and magnetic dipole transition moments (Eq.36), leading to the chiroptical inversion. In both contributions, it was reported that the g-values evaluated from the data obtained in the supersonic beam yielded larger values compared to the case of the effusive beam, for the correspondent wavenumber and its vibrational mode. That could be justified by the fact that in the effusive beam due to the broadening of transition bands, there exists the overlap of several vibrational modes, resulting in the corresponding averaged g-value. On the contrary, in a supersonic beam, because of the cooled molecular beam, narrow transition bands are achieved, hence, the chance of overlap for vibrational modes and consequent, g-values is small. On that account, performing CD-REMPI-MS technique in the cooled molecular beam may assist the scientists and theoreticians to have more profound insight into the configurations and electronic structures of the molecules, especially chiral molecules, in the gas phase. The limitation of CD-REMPI-MS is that it can only be applied to molecules in the gas phase. To overcome this limitation, laser desorption is combined with this technique in order to study non-volatile molecules which do not come easily into the gas phase. Therefore, the next section is devoted to laser desorption.

2.3.   Laser desorption (LD)

In order to perform the CD-REMPI-MS technique on non-volatile molecules, for example, products of the asymmetric catalysis, laser desorption is combined with CD-REMPI-MS. There a laser beam is employed to desorb the molecules from the surface and bring them into the gas phase. In this section, the laser desorption technique is discussed in more detail.

The idea of laser desorption was motivated by the high demands for analyzing biomolecules and large organic molecules in the gas phase. These molecules are generally non-volatile and have a low vapor pressure, meaning that they are not vaporized, willingly. Sometimes, non-volatile molecules are heated up in order to bring them into the gas phase, but there are some cases that become decomposed during the heating process. Thus, those molecules are the main target of laser desorption. Quite a few methods exist which combine desorption and ionization processes, including secondary ion mass spectroscopy, fast atom bombardment, plasma desorption, laser desorption, matrix-assisted laser/ionization, and so on (*61*).

Desorption of a molecule from a surface requires the breaking of the bonds between them. This goal can be achieved by heating the system to the temperature where molecules have enough energy to overcome the desorption energy, which is the case of thermal desorption (TD). If an electron is used for the desorption, the process is called electron impact desorption (EID) or

20

electron-stimulated desorption (ESD). In this process, electron impact causes transitions to the excited or ionized states of the molecules on the surface. The other applied method is field desorption (FD), where, a very large electric field is applied which makes tunneling possible for the adsorbate from its ground to its ionic states. This process results in the removal of ions from the surface. The method, which is the scope of this thesis, is photo-desorption (PD) or nowadays called, laser desorption (LD), where excitation happens with the help of the laser light (*62*).

In this report, the focused is more on the two-step process where neutral molecules are desorbed and then ionized through REMPI and detected in a mass spectrometer. This procedure has the advantage that a larger number of desorbed molecules can be detected compared to the one-step process where desorption and ionization steps are merged. In addition, one can separately and independently tune the intensities applied for the desorption and ionization processes. The combination of laser desorption with a pulsed general valve and REMPI was successfully achieved, 30 years ago. In that work, anthracene, diphenylamine and perylene were studied and the vibrational and rotational temperatures of <15K and 5-10K were approximated, respectively (*63*). Although laser desorption has found its place in research, there exist diverse hypotheses in terms of the mechanisms behind it. They are categorized into two groups, namely thermal desorption and quantum mechanical processes. In the following section, different proposed laser desorption mechanisms will be reviewed.

  ▪ *Laser-induced thermal desorption (LITD)*

If the laser radiation hits the molecules deposited on the substrate, the substrate can absorb the laser radiation and is subsequently heated up. This increment in the temperature is in accordance with the pulse width of the laser pulse. This process results in the desorbing of the molecule from the substrate surface. In this case, temperature changes in the substrate surface play a role, clearly. The temporal and spatial temperature distributions in the substrate can be shown as:

$$C(T)\frac{\partial T(r,t)}{\partial t} = -div\, J(r,t) + I(r,t) \tag{38}$$

Where,

$$J(r,t) = K(T)\nabla T(r,t) \tag{39}$$

$I(r,t)$, $J(r,t)$, C(T) and K(T) stand for laser heating, heat flow, the specific heat and heat conductivity, respectively. One can replace the laser heating with the laser irradiance, as below:

$$I(r,t) = \alpha(1 - R)\, I_0(r,t)exp[-\alpha z) \tag{40}$$

$I_0(r, t)$ denotes laser irradiance while R is a surface reflection. The substrate has a light absorption coefficient of α (wavelength dependent) and the incident laser propagates in z-direction (normal to the surface). Based on a couple of experimental and theoretical investigations done by Lax, Zenobi, and others, it was verified that the heating rate can be very high ($> 10^8$ K/s) (*64*). The effective length of desorption caused by absorption of a photon can be estimated by

$$d_{micro} \cong \tau_{vib} v_s \tag{41}$$

Where τ_{vib} is a typical phonon vibration in the material and v_s stands for the speed of sound. This verifies that desorption must be a localized process. Thus, desorption must occur before the energy of the incident photon vanishes into the adjacent area. This length spans from 0.1 to 10 nm (*65*). In an example of a metal or semiconductor system and a laser beam which excites the valence band electrons, due to the fact that the optical absorption coefficients are large, the optical penetration depth is smaller than the thermal diffusion depth. Accordingly, the electrons which are excited now, have about 100 femtoseconds as mean-free time between the collisions with the lattice phonons. Subsequently, these collisions convert the received energy to the thermal one. The conversion time is dependent on the collision time and is approximately some picoseconds. Thus, by having laser pulses in the nanosecond scale width, all the energy is converted as soon as absorbed (*66*). The interesting point where laser-induced thermal desorption differs from the conventional thermal desorption is that thanks to the higher heating rate, the reaction channels which are preferred under conventional methods are bypassed here, e.g. decomposition (*67, 68*). For the thermal desorption, two assumptions can be made, 1) there is a linear heating regime, where, the temperature increases continuously, within the desorption process, 2) there is an isothermal regime at which the desorption occurs close to the maximum achievable temperature. In real cases, the temperature cannot elevate linearly. Generally, in accordance with the study on the conventional thermal desorption done by Readhead (*69*), the comparison of the data for linear and hyperbolic heating, revealed that desorption is influenced by the heating rate at the maximum desorption rate rather than a heating schedule.

The desorption kinetics are normally treated, according to:

$$-\frac{d\sigma}{dt} = v_n \sigma^n \exp\left(\frac{-E}{KT}\right) \tag{42}$$

Where, σ denotes surface concentration, n stands for the desorption order, v_n is pre-exponential and E is the desorption activation energy (*70*).

- *Quantum mechanical effect in laser desorption*

The thermal desorption induced by photon absorption was discussed in the previous section. Thermal desorption always happens, but it can be negligible if the laser fluence will be chosen small enough. The other possible laser desorption mechanism is described via the electronic excitation of the adsorbed molecules and/or substrate, which is called quantum mechanical (QM) mechanism. In contrast to the thermal desorption mechanism, in QM mechanism at given photon energy, the number of desorbed molecules is proportional to the number of absorbed photons. The electronic photoexcitation of the molecules on the surface and/or substrate is the cause of desorption by the QM mechanism. Therefore, the effectiveness of the process depends strongly on the lifetime of the excited electronic state.

Fabel et al. studied the case of QM mechanism behind laser desorption (*71*). Their report demonstrates the role of the substrate in the QM mechanism. The performed experiments on three different substrates including metals, semiconductors and stainless steel, showed that the true metal surfaces showed no or very small desorption; whereas semiconductor surfaces seemed to be a suitable choice. Therefore, 304 stainless steel with a coated semiconductor layer showed significant desorption. The threshold for the QM mechanism is determined by the bandgap of the semiconductor, hence, the adsorbed molecules and their binding energy play no role. For the measurements done at various wavelengths on the 304 stainless steel, laser fluence was kept below 290 $\mu W/cm^2$, corresponding to the maximum 1°C increment of the surface temperatures. Considering that a minimum 50°C change is essential for thermal desorption (*71*), it is deduced that the observed desorption happened through laser desorption cannot be caused by the thermal desorption process.

Menzel, Gomer and Redhead have also worked on the possible mechanisms describing the desorption process. They surveyed desorption via electron impact or photodissociation which leads to desorption induced by electron transition (DIET). They suggested MGR (Menzel,

Gomer, Redhead) mechanism, where the adsorbate-substrate system is excited to the ionic state. Subsequently, either there will be the desorbed ions, or the system goes through an Auger transition. Therefore, it will be excited to a neutral state and then desorbed (*72*). The prerequisite of such a mechanism is a large amount of energy which needs to be imposed on the system in order to bring the system to the electronic state, which is repulsive regarding a specific bonding mode. Such a transition from the ground state to a repulsive potential curve (neutral antibonding state), converting this transition energy into the nuclear motion. The probability of having desorption depends strongly on the cross-sections of the bonding mode, excitation energy, the mass of the adsorbed molecules and the coverage. Also, it depends on the overcoming of other competitive processes which take away the energy from the original location (delocalization of the energy) (*73*). A very similar mechanism was also suggested for laser desorption (photo-desorption) by Adams and Donaldson, one year later (*74*).

Antoniewicz also suggested a QM mechanism for the desorption process. The first assumption he made was that the particles are following the classical trajectories. The adsorbate-substrate complex is excited by a laser beam, and subsequently, an ion is created from the adsorbed molecule whose radius is smaller than the neutral one. Thus, the actual position of the ion is located closer to the surface compared to its position before excitation. Consequently, the ion moves towards the substrate. The ion is neutralized via electron tunneling from the substrate, while its kinetic energy remains unchanged. However, it gains some potential energy, due to the repulsive motion, caused by a shorter distance than the equilibrium distance to the surface. Now if the total energy of the neutral molecules is greater than the binding energy, the neutral molecule is desorbed from the surface (*75*).

Hypothetically, thermal and quantum effects can happen in different time scales; thermal effects are local and need to be diffused, while quantum effects happen in a short time (*76*). The mentioned mechanisms are expected to extend to all adsorbate-substrate systems including chiral molecules on the substrates. In the case of chiral molecules, there is another parameter which can control the mechanism of desorption, which is the response of enantiomers to the different handedness of circularly polarized light. If the light, which is used for desorption, is altered from linearly to circularly polarized, one can expect to have an enantiospecific desorption. The enantiospecific desorption was reported for the case of chiral adsorbate-chiral substrate for temperature programed desorption (TPD) (*77*), however, it has not been investigated for laser desorption of chiral adsorbate-achiral substrate, which is the main objective of this thesis. The

changes in the optical activity at the surface exposed to circularly polarized light is measured by second harmonic generation-circular dichroism (SHG-CD). Thus, SHG-CD is explained in the following section.

2.4.   Second harmonic generation- circular dichroism (SHG-CD)

Chiral separation (chiral resolution) is a procedure employed in the pharmaceutical industry and clinical analysis in order to separate the two enantiomers of chiral mixtures. A variety of methods can be applied for chiral resolution (*18*), including 1) crystallization or filtration in case of solubility of one enantiomer and insolubility of the other, 2) achiral liquid chromatography (*78*), 3) enzymatic or kinetic resolution by performing a biochemical process to destroy one of the enantiomers, 4) high-performance liquid chromatography (HPLC), where chiral HPLC is one of the best separation methods (*79-81*), 5) gas chromatography (GC), 6) affinity electrokinetic chromatography and so on. In this thesis, as already mentioned in the introduction, a new enantiomeric enrichment method is suggested which is called enantiospecific desorption. In this method, circularly polarized light is used to enantioselectively desorb one of the enantiomers in the mixtures. Such a method has a big advantage over the well-established methods that it is applicable without the assist of reagent chemicals. That reduces the cost of the enantiomerically enrichment procedure as well as avoids contaminations. This new method will be presented and discussed, as a part of this thesis. Enantiospecific desorption is performed on the film of the racemic mixture of a chiral molecule, therefore, SHG-CD as a combination of the high surface sensitive method and the nonlinear chiroptical detection method can reveal even the small expected effects from the surface. Thus, SHG-CD will be explained in this section.

  ▪ *Second harmonic generation (SHG)*

Surface science, with its key role in a variety of scientific fields such as physics, chemistry and biology, has attracted many researchers, over the last decades. Accordingly, demands for surface characterization methods have increased. There exist many techniques to characterize the surface, however, they are not without limitations. Among all the techniques, second harmonic generation (SHG) has the privilege of being simple and nondestructive, and applicable to all phases of materials in all situations, e.g. in-situ and ex-situ (*82*). SHG was developed in 1962 by Bloembergen and Pershan. Afterward, there were more studies on the physical origins of nonlinearities, resulting in an SH response from the surface. Even though the monolayer

sensitivity of the SHG technique was demonstrated, it did not receive notable attention. In 1974, surface-enhanced Raman scattering was discovered. Where a nonlinear two-photon process, was employed to explain it. Since such a surface enhancement resulted from a nonlinear optical process, it was concluded that the other nonlinear optical processes have the advantage of surface enhancement, too. Thus, SHG was established as a surface probe, and later on, it was revealed that SHG is able to detect monolayers even without surface enhancement. From that time on, SHG became one of the important techniques to investigate surfaces and interfaces. Contrary to linear optical techniques, where interfacial molecules in the bulk contribute to the signal and make the separation between the signal from the surface and from the bulk difficult, nonlinear optical techniques can be restricted to the surface. If in SHG, sub-picosecond laser pulses are applied, the technique will be advanced to the sub-picosecond time resolution giving a potential to be used in real-time probing of fast surface dynamics and reactions. Also, it is possible to observe the surface arrangement and composition of molecules in-situ, thanks to the high capability of the spectral and spatial resolution of the laser excitation.

SHG is a second-order nonlinear optical effect, and therefore forbidden in a medium with inversion symmetry (if applying electric-dipole approximation). To generate SHG, this symmetry needs to be broken, which is the case at interfaces. Due to the fact that SHG signal is coherent and monochromatic, the separation of output and input, the background luminescence and scattering is easy with the help of spatial and spectral filters (*83, 84*).

In the following, a brief theoretical background of SHG will be described. Optical processes can be categorized based on their behavior towards external electric fields. The optical polarization, which depends on the property of the material, defines the interaction of the material with the electric field. The strength of the electric field of the bonds in atoms can be estimated as $E_a \sim 1$ V/A° = 10 V/m. In order to reproduce such a filed, the intensity as big as 10^{17} W/m^2 is necessary which is achievable with lasers. The electromagnetic field induces polarization in the material which leads to the emission of electromagnetic light in return. The polarization can be defined with the help of power series in *E*, where *n* is the order of the polarization element in the field.

$$P = P^{(0)} + P^{(1)} + P_{NL} \tag{43}$$

$$P = P^{(0)} + P^{(1)} + P^{(2)} + P^{(3)} + \cdots \tag{44}$$

$$P = P^{(0)} + \varepsilon_0 \chi^{(1)} \cdot E + \varepsilon_0 \chi^{(2)} \cdot EE + \varepsilon_0 \chi^{(3)} \cdot EEE + \cdots \tag{45}$$

P^0 denotes static polarization and $P^{(1)}$ stands for the linear polarization which is responsible for the linear optical process, such as absorption, light propagation, reflection and refraction. χ is the susceptibility tensor, E is the incoming field and ε_0 is the dielectric constant.

In a linear process, the field strength is moderate, thus, higher orders can be neglected. Consequently, the polarization will be linearly proportional to the incoming field. Accordingly, generated light has the same wavelength and frequency. Though, this is not the case for nonlinear processes. P_{NL} defines the nonlinear optical responses ($P^{(2)} + P^{(3)}+\ldots$). The simple example for such a process is a mixture of n laser fields with vectors $K_1, K_2, \ldots, K_n$ and frequencies of $\omega_1, \omega_2, \ldots, \omega_n$, respectively (*85*). Therefore, a generated coherent signal has

$$Ks = K_1 \pm K_2 \pm \ldots \pm K_n \tag{46}$$

$$\omega_s = \omega_1 \pm \omega_2 \pm \ldots \pm \omega_n \tag{47}$$

For the second order polarization, we have:

$$P^2 = \varepsilon_0\chi^{(2)}:E_1E_1 + \varepsilon_0\chi^{(2)}:E_2E_2 + 2\,\varepsilon_0\chi^{(2)}:E_1E_2$$

$$= \varepsilon_0\chi^{(2)}:E_1^2(r)(1-\cos(2\omega_1 t)) + \varepsilon_0\chi^{(2)}:E_2^2(r)(1-\cos(1-2\omega_2 t)) \tag{48}$$

$$+2\varepsilon_0\chi^{(2)}:E_1(r)E_2(r)(\cos(\omega_1+\omega_2)t + \cos(\omega_1-\omega_2)t)$$

Here in addition to the nonlinear response, the linear process will occur, too. Moreover, the intensity of the emitted light is proportional to the square of polarization:

$$I_{\omega_1+\omega_2} \propto \left(P^{(2)}\right)^2 = \left|\chi^{(2)}\right|^2 I_{\omega_1}I_{\omega_2} \tag{49}$$

$I_{\omega i}$ is the incoming light intensity with the frequency of ω_i. In the case of second harmonic generation $\omega_1 = \omega_2$ which results in $K_s = 2K_1$ and $\omega_s = 2\omega_1$. Mostly, nonlinear optical spectroscopy performs in a resonant mode, where the incoming light or the combination of the electromagnetic fields possess the identical frequency of the transition in the medium. This mode is sensitive to the vibronic transitions as well as fast processes like relaxation via spontaneous emission (*86*).

Bloembergen and Pershan formulated SHG for a layer of nonlinear material with a thickness of d. They assumed that this layer is in contact with linear media from top and bottom. Having Z

as the surface normal axis, the height covered with the nonlinear medium will be 0 < d < -z as shown in Fig.6 (*87, 88*). There exist two possibilities for SHG signal to be collected, either as a reflected response of the surface or as a transmitted one. Here, in this work, the focus lies in the transmitted SHG signal.
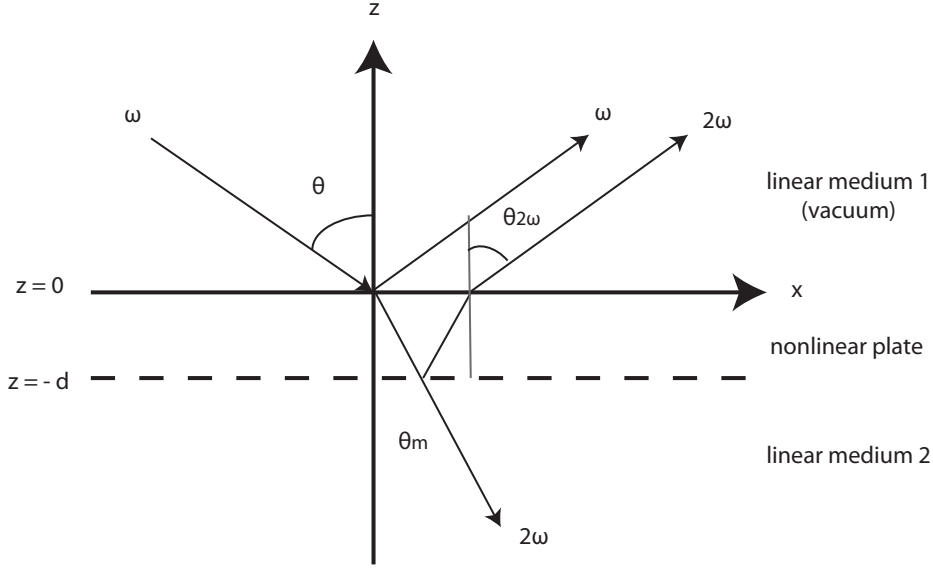

Figure 6- Second harmonic generation process for both transmission and reflection modes, when a nonlinear layer is in contact with linear media.

The resulted electric field for the transmitted SHG is estimated for s polarization (polarized perpendicular to the plane of incidence) as,

$$E_{2\omega}^T = i4\pi P_{\perp}^{NLS} (\frac{2\omega d}{C}) \frac{1}{n_{2\omega} \cos\theta_m + \cos\theta} \tag{50}$$

and for p polarization (polarized parallel to the plane of incidence) as,

$$E_{2\omega}^T = i4\pi P_{\parallel}^{NLS} (\frac{2\omega d}{C}) \frac{(\cos\theta \sin\alpha - \frac{1}{n_{2\omega}} \sin\theta_m \cos\alpha)}{n_{2\omega} \cos\theta + \cos\theta_m} \tag{51}$$

Where $n_{2\omega}$ is the refractive index of the second harmonic wave. α stands for the angle between the nonlinear polarization in medium 2 and -Z axis and P^{NLS} is defined as:

$$\vec{P}^{NLS} = P_{\perp}^{NLS} \hat{s} + P_{\parallel}^{NLS} \hat{p} = P_{\perp}^{NLS} \hat{y} + P_{\parallel}^{NLS} (\hat{x} \sin\alpha - \hat{z} \cos\alpha) \tag{52}$$

28

The propagation of the second harmonic wave is defined by the conservation of the momentum, therefore, for ω, $K_{\omega,x} = K_{\omega,x}^R = K_{\omega,x}^T$ and for 2ω, $2K_{\omega,x}^T = K_{2\omega,x}^R = K_{2\omega,x}^T$. Based on the latter one, one can have (*88*):

$$\sin\theta_m = \frac{K_{2\omega,x}^T}{|K_{2\omega}^T|} = \frac{2K_{\omega,x}^T}{n_{2\omega}|2K_\omega|} = \frac{2}{n_{2\omega}} \sin\theta \tag{53}$$

As mentioned briefly before, SHG is not permitted in all media, e.g. all centrosymmetric media, such as liquid, gas and amorphous do not possess a second-order susceptibility. Thus, no second-order nonlinear process can be obtained from such media with a vanishing $\chi^{(2)}$. However, at the interface thanks to the broken symmetry, the second-order nonlinear optical process (SHG) can be observed. Furthermore, the intensity of the emitted light depends strongly on the surface, which is illustrated in $\chi^{(2)}$. For instance, the emitted light intensity changes linearly with the number of molecules on the surface, if the interaction between the molecules is neglected.

Here, the quantum mechanical description of the non-centrosymmetric molecules at a surface will be explained in more detail. As mentioned briefly before, the induced nonlinear dipole moment $P^{(2)}$ can be written for each molecule in respect of the driving electric field as below:

$$P^{(2)}(2\omega) = \alpha^{(2)}(2\omega = \omega + \omega) : E(\omega)E(\omega) \tag{54}$$

Where $P^{(2)}$ and E are vectors and $\alpha^{(2)}$ is the second-order nonlinear polarizability which is a third-rank tensor. By considering the second-order perturbation theory for the interaction between light and matter (within the electric-dipole approximation), $\alpha_{ijk}^{(2)}$ of the tensor $\alpha^{(2)}$ will be:

$$\alpha_{ijk}^{(2)}(2\omega = \omega + \omega) =$$

$$-\frac{1}{\hbar^2} \sum_{g,n,n'} \left[\frac{(\mu_i)_{gn}(\mu_j)_{nn'}(\mu_k)_{n'g}}{(2\omega - \omega_{ng} + i\Gamma_{ng})(\omega - \omega_{n'g} + i\Gamma_{n'g})} + \cdots \right] \rho_g^{(0)}. \tag{55}$$

g, n, n′ denote energy eigenstates $|g\rangle$, $|n'\rangle$ and $|n\rangle$ of the system, respectively. $\rho_g^{(0)}$ represents the thermal population of differing available ground states g. These transitions happen through the electric-dipole operator μ and are expressed by the matrix element $(\mu_i)_{gn}$. The matrix

elements $(\mu_i)_{gn}(\mu_j)_{nn'}(\mu_k)_{n'g}$ describe the structure and symmetry of the material. The energy differences and widths for the transitions between $|g\rangle$ and $|n\rangle$ are illustrated as $\hbar\omega_{ng} = E_n - E_g$ and $\hbar\Gamma_{ng}$, respectively. That is generally valid for all other combinations of states. There are three possible cases of SHG, which are shown in Fig.7. Two photons with the energy equals of $\hbar\omega$ are absorbed by the matter and the corresponding second harmonic photon with the energy of $2\hbar\omega$ is reemitted. A non-resonant SHG happens (Fig.7a), when the emitted photons and the reemitted one, do not match the transitions in the molecule, while, a resonant enhancement happens in case b and c in Fig.7, where ω or its responds 2ω match transitions from the ground state $|g\rangle$ to one of the intermediate states $|n\rangle$ or $|n'\rangle$.
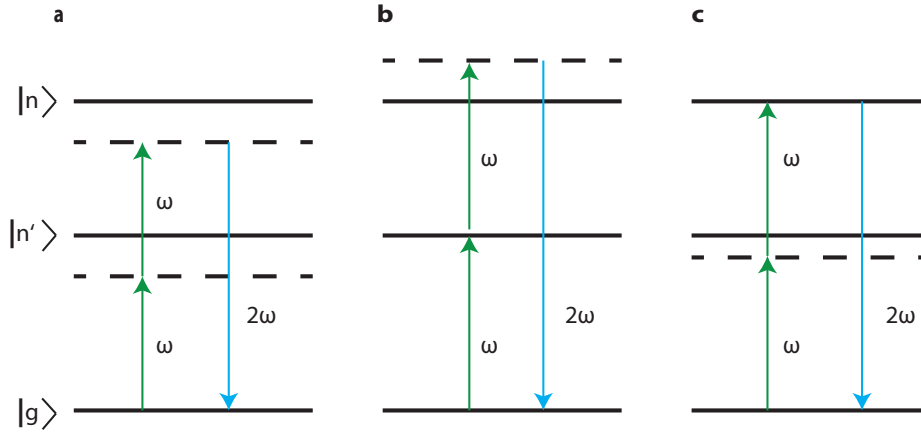

Figure 7- SHG processes. a) non-resonant transition and SHG response, b) resonant transition and non-response, c) non-resonant transition and resonant response.

By assuming a monolayer of oriented molecules and excluding the local-fields, one can estimate the nonlinear response by summation over all molecules. Thus, the outcome $\chi_{s,ijk}^{(2)}$ will combine the induced nonlinear sheet polarization with the driving electric field, as:

$$\chi_{s,ijk}^{(2)} = \frac{N_s}{\varepsilon_0} \langle T_{i\lambda} T_{j\mu} T_{KV} \rangle \alpha_{\lambda\mu V}^{(2)} \tag{56}$$

Where N_s is the adsorbate surface density, $\alpha_{\lambda\mu V}^{(2)}$ stands for nonlinear polarizability of the molecule in its own coordinate system, $T_{i\lambda}$ describes the molecule transformation tensor from its own to the laboratory frame, $\langle ... \rangle$ is an ensemble average over the different orientation of the coordinate system of the molecules, and ε_0 denotes the permittivity of free space. Thus, the

tensor element $\chi^{(2)}_{s,ijk}$ reveals valuable information about the adsorbed molecules such as their coverage, orientation and spectroscopic characteristics. The tensor properties illustrate the symmetry of the interface independent of the model describing the surface nonlinear susceptibility (*89*).

Apart from the strong nonlinear response from the interface, the non-local nonlinear response from the bulk media shall also be taken into account. The electric quadrupole and magnetic dipoles are responsible for the non-local response which is allowed even in the medium with inversion symmetry, while the electric dipole causes SHG from the surface. Thus, an effective susceptibility, $\chi^{(2)}_{eff}$ can be defined, which is the combination of susceptibilities from surface and bulk. To distinguish their contributions to the obtained SHG, they need to be estimated, quantitively. The electric dipole part of $\chi^{(2)}_{eff}$ is $\lambda/2\pi a$ times bigger in comparison to the electric quadrupole and magnetic dipole parts. Here, *a* is the unit cell size. The thickness of $\lambda/2\pi$ near the surface is the main area, contributing to the bulk response. Now, if we assume a thickness of *d* for the layer contributing to the SHG, the quantitative ratio between the response from the surface and the bulk is *(d/a)²* (*88*). Generally, the signal from the surface is inevitably influenced by the bulk, however, that can be excluded by modifying the interface and controlling the coverage of the molecules. It was also proved that the change in $\chi^{(2)}_s$ has a linear behavior as a function of adsorbate density(*89, 90*).

To correspond intensity of the SH signals to the experimental parameters and optimization the signal, the equation below can be considered:

$$S = \frac{\omega sec^2\theta \, E_P^2 \, R \left|\chi^{(2)}_{eff}\right|^2}{4 \, \hbar\varepsilon_0 C^3 \tau A} \tag{57}$$

$$\left|\chi^{(2)}_{eff}\right|^2 \equiv \frac{\left|e'(2\omega) \cdot \chi^{(2)}_s : e'(\omega)e'(\omega)\right|^2}{\left[\varepsilon_1^{\frac{1}{2}}(2\omega)\varepsilon_1(\omega)\right]} \tag{58}$$

Where *S* is in units of photons/s. E_P and τ denote pulse energy and pulse width, respectively. θ is the incident angle of the incoming beam, while $e'(\omega)$ represents the polarization vector $\hat{e}_1(\omega)$, after being aligned for the linear propagation of the beam towards the surface. *R* stands for

repetition rate and A is the illuminated area on the sample. C is the speed of light and ε_1 stands for the frequency-dependent dielectric function.

Eq.57 yields the direct influence of the pulse energy and pulse length on the SH signals. As an example, with a femtosecond laser mode-locked Ti: sapphire oscillator, the range of $10^2 - 10^6$ photons/s will be expected for S. This intensity is not strong, though strong enough to be detected by a photomultiplier tube (PMT) and required electronics (*89*).

- *Second harmonic generation- circular dichroism (SHG-CD)*

Second Harmonic Generation – Circular Dichroism (SHG-CD) is defined according to the SHG responses of the surface to the different handedness of circularly polarized light, by which Eq.37 is developed to:

$$g = \frac{2\left(I_{SHG}^{left} - I_{SHG}^{right}\right)}{\left(I_{SHG}^{left} + I_{SHG}^{right}\right)} \tag{59}$$

SHG-CD has been applied on surfaces and interfaces to investigate their nonlinear optical activities. The first pioneer in this field is Petralli-Mallow et al. (*27*). In their report, they successfully combined SHG with CD spectroscopy. It was reported that, on the investigated system of 2,2'-dihydroxy-l,l'-binaphthyl molecules adsorbed at the air/water interface, CD value obtained from SHG signals has a larger magnitude compared to that value of conventional CD spectroscopy. Later on, they proved their achievements with the help of the theory (*29*). There, it was demonstrated that SHG-CD shows large effects because it is electric dipole allowed rather than dependent on the weak magnetic dipole transition moment and consequently weak rotational strength. Furthermore, they showed that this observation resulted from the increment of the imaginary components of $\chi^{(2)}$ near the resonance, therefore, the SHG-CD signals were significant and measurable. At the same time, Kauranen et al. (*91*), demonstrated that magnetic dipole transition moments also plays a role in the optical activity. Later on, they claimed that, magnetic dipole moments are mainly responsible for the CD effects through SHG measurements and electric dipole moments cause optical activity just near the resonance (*92*). By that, they explained the achiral behavior of a racemic mixtures. A chiral molecule may have a right- or left-handed helical structure; on that account, it is not superimposable on its mirror image. Consequently, there exists no mirror plane for a chiral molecule. Now if we have a layer of one enantiomer of a chiral molecule through which they are distributed isotopically, the system will

be still chiral with no mirror plane. On the other hand, in case that both enantiomers exist in the layer with an equal contribution (50:50), e.g. racemic mixtures, the system will turn into an achiral and centrosymmetric system that possesses mirror planes. Such a system yields no optical activity due to the fact that, magnetic dipole transition moments of both enantiomers are equal but have opposite signs. Thus, they will cancel out each other (*92*). Afterwards, there have been several works on SHG-CD for different chiral systems such as, investigating the oxidation state of a redox membrane protein, cytochrome c (*93, 94*), observing the optical activity of different biological chiral molecules on the surface (*95*), achieving SHG-CD signal from a uniaxial layer of achiral molecules where they are arranged in a chiral manner (*96*) and very recent article presenting SHG-CD performance on metamaterial nano-helices made out of Au (*97*).

SHG-CD was employed in this thesis, as a precise tool in order to follow the chiroptical changes of the surface, applied during the enantiospecific desorption process.

3. Experimental

All the methods, which have been used throughout this thesis, can be split into three main techniques, namely gas phase laser spectroscopy, laser desorption of non-volatile chiral molecules, and enantiospecific desorption by circularly polarized light. In the following, more detailed explanations of the mentioned techniques, the utilization of them within this thesis and the corresponding set-ups are presented.

3.1.   Gas phase laser spectroscopy

CD-REMPI in combination with the twin-peak technique and the time-of-flight mass spectrometer (TOF-MS) was employed to analyze volatile chiral molecules. This combination provides a three-dimensional selective gas phase laser spectroscopy technique including enantioselective CD, wavelength selective REMPI and mass selective MS.

3.1.1. Apparatus and vacuum systems

The analysis of volatile chiral molecules in the gas phase is usually conducted in high vacuum systems in order to prevent any interferences with other molecules in the environment and also to provide a desired pressure and environment for the evaporation of volatile molecules.

In the presented set-up in Fig.8, two main compartments can be defined. The first part is the inlet part, where volatile molecules are introduced via the effusive beam and/or the supersonic beam. This part consists of gas lines and a feed-through of the pulsed general valve, effusive beam inlets and the ion source. To evacuate the chamber, a twin turbomolecular pump (TPH 330, Pfeiffer vacuum) and two turbomolecular pumps (TMU 261 and TMH 261, Pfeiffer vacuum) are employed. The optimized reachable pressure is around $4 \cdot 10^{-7}$ mbar. This compartment is separated with a gate valve (VAT vacuum valve) from the second part of the set-up. The second compartment consists of the time-of-flight (TOF) tube which provides 120 cm field-free drift region, and an MCP detector (designed based on Wiley and McLaren TOF-MS (*98*)). This compartment is pumped down with a twin turbomolecular pump (TPU 330, Pfeiffer vacuum) to the pressure of $4 \cdot 10^{-8}$ mbar. In the following, the components of each compartment are described in more detail.
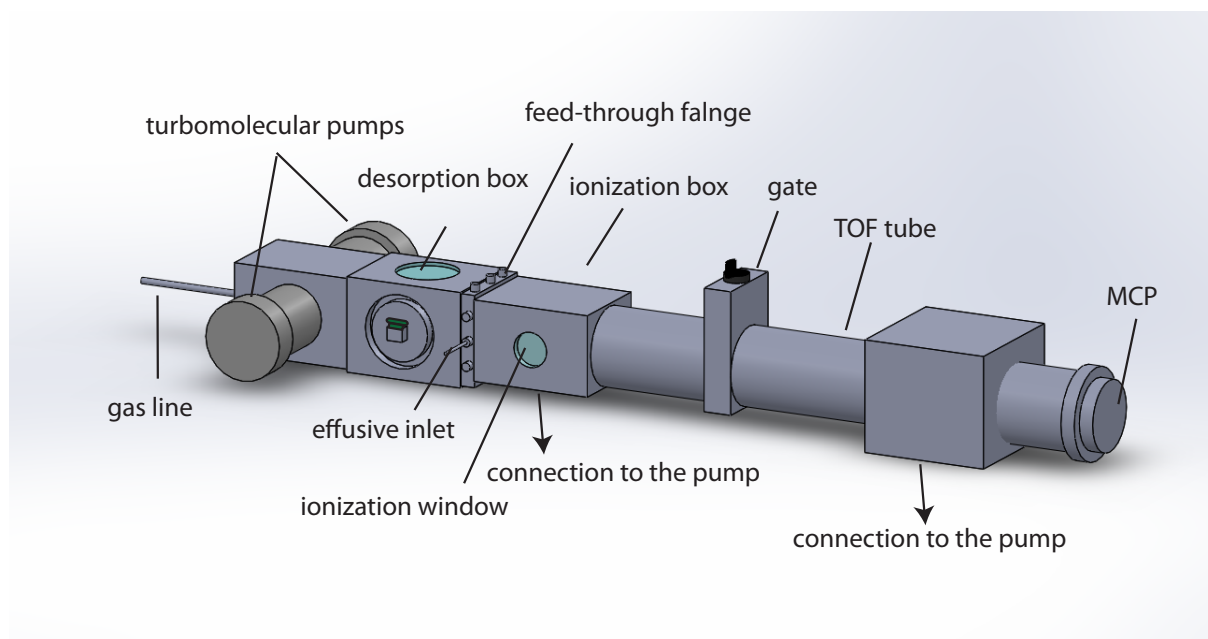
Figure 8- Schematic view of the set-up used for gas phase laser spectroscopy.

3.1.2. Pulsed general valve

Generally, there are two categories of valves used to introduce gases into the gas phase. They are either continuous such as leak valves or pulsed like pulsed general valves. The former one is for continuous usage, while the latter one is used to pulse the gases into the chamber at specified times (*99*). The idea to take advantage of the pulsed molecular beam was initiated by Hagena and co-workers (*100*). The most known advantages of such valves are the strong expansions and high rapid intensities which are reachable with the moderate pumping and low sample consumption. In our set-up, the advantage of the pulsed general valve is to have a possibility of collisions between the carrier gas and the molecules and subsequent supersonic expansion. The used pulsed general valve here was bought from General Valve Corporation (series 9). The gas line designed for the pulsed general valve goes through the large self-made stage which embodies the feed-through. The stage allows aligning the valve collinearly to the ion source. The backpressure of the carrier gas (Ar 4.6, 99.996 vol% Ar) is regulated from 0.5-5 bar. The volatile substances are placed in a small dismountable part of the gas line, on the way of the carrier gas and outside of the vacuum chamber. Having the reservoir of the molecules outside of the chamber gives the possibility to change or refill it without venting the system.

3.1.3. Effusive beam inlets

The inlets of the effusive beam are implemented via Swagelok system. Two narrow pipes go through the feed-throughs installed on the flange (see Fig.8), which contains the ion source. There, they are connected by small tubes to the part, installed on the repeller plate. The repeller plate consists of an inner cone and two outer cones. The former guides the supersonic beam through the repeller plate, while the latter ones, which are connected to the effusive beam inlets, generate an effusive beam which wraps the supersonic beam, as depicted in Fig.9. The detailed explanations for the effusive inlets can be found elsewhere (*13*). One of the advantages of such a system is to wrap the supersonic beam, coming from the general valve, homogeneously and without disturbing the cooled molecular beam. This also provides the possibility to detect both the effusive plume and the cooled molecular beam at the same time and axis. The other advantage of these effusive inlets is that the inlets work separately and independently from each other, therefore, two different volatile substances can be analyzed, simultaneously. The substance is located in a small container, which is fastened to the Swagelok system. A small Swagelok valve separates the atmospheric pressure and the high vacuum pressure inside the chamber ($4 \cdot 10^{-7}$ mbar). By opening the valve, molecules are vaporized into the gas phase inside the apparatus.
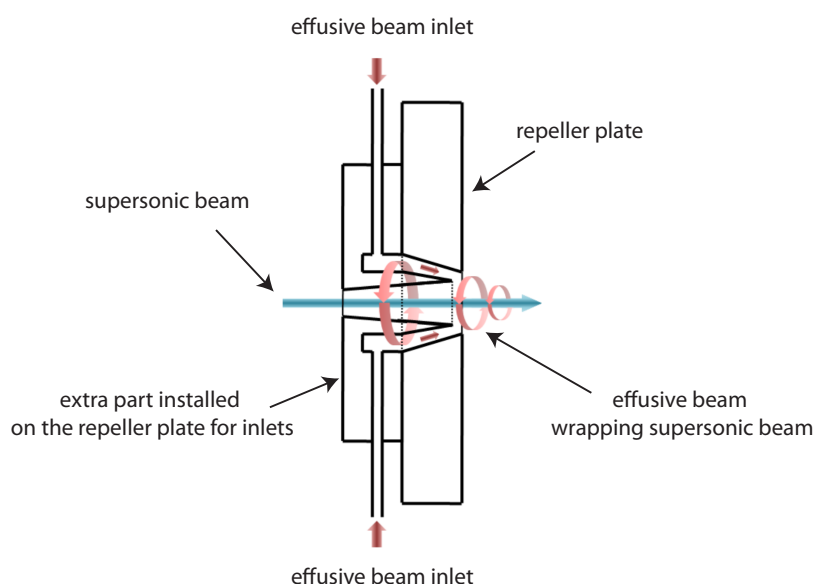

Figure 9- A schematic view of the repeller plate with implemented effusive beam inlets. Reproduced from Ref. (*13*) with permission from the PCCP Owner Societies.

3.1.4. Ion source and time-of-flight mass spectrometer (TOF-MS)

The investigation of ion rays and ion beams motivated the idea of having a source, which is suitable for ionizing atoms in the gas phase. This idea was pushed further by introducing and combining the ion source with a mass spectrometer (*47*). The simplest TOF mass spectrometer has an ion source and a detector at the opposite end. Generally, neutral molecules are ionized in the ionization point, in front of the repeller plate. The ionized molecules are accelerated through one or more electrical fields and flying towards the detector. The fields are either continuous (the current set-up) or pulsed (the prototype set-up of laser desorption, section 3.2.1). In both cases, an electrical field applies to all the ions, thus, the ions possess the same energy. Since there is no additional field to accelerate the ions after the ion source, the momentum of the ion is preserved. The velocity that the ions obtain, is a function of the ratio between their mass (*m*) and charge (*z*). Consequently, they are split into groups based on that ratio. The lightest group arrives faster than the heavier one. The two main advantages of this mass spectrometer are the speed of data acquisitions, which is in the range of microseconds, and having a general view on all detected species in one mass spectrum. These two properties make the TOF-MS a unique apparatus in analyzing the molecules in the gas phase (*98, 101*).

- ▪ *Ion source description:*

The linear TOF contains a repeller plate, an accelerator plate, a ground plate, deflector plates, einzel lens plates and a linear drift region. The time that an ion flies through the TOF is divided into two main parts, including the time that the ion spends in the acceleration fields (t_A) and in the field-free (drift region) region (t_D). In order to calculate the flight time for all the ions, some Newtonian physics equations are required as listed below:

$$\begin{cases} F = E_A q \\ F = ma \end{cases} \rightarrow a = \frac{E_A q}{m} \tag{60}$$

$$a = \frac{dv}{dt} \rightarrow v = \int \frac{E_A q}{m}\, dt \rightarrow v = v_0 + \left(\frac{E_A q}{m}\right) t \tag{61}$$

a is the constant acceleration in a homogeneous electric field E_A which gives the acceleration potential of V_A for the ion at the positions s_A. *m* is the ion mass, *q* stands for the charge and *v* denotes the velocity. Therefore, t_A is :

$$t_A = \frac{v - v_0}{E_A}\left(\frac{m}{q}\right) \tag{62}$$

By considering the following equation,

$$s = \int v \, dt \tag{63}$$

Where s is the position of the ion with the velocity of v at dt. We have:

$$s = s_0 + v_0 t + \frac{1}{2}\left(\frac{E_A q}{m}\right) t^2 \tag{64}$$

$$\tag{65}$$

$$t_A = s_A \sqrt{\frac{2m}{V_A q}}$$

or

$$t_A = \sqrt{\frac{2 s_A m}{E_A q}}$$

$$\tag{66}$$

It should be noted that t_A is calculated as the functions of the acceleration potential, V_A, in Eq.65 and the acceleration space, s_A, in Eq.66.

For the drift region, one can deduce:

$$qV_A = qE_A s_A \tag{67}$$

$$qE_A s_A = \frac{1}{2} m v_D^2 \tag{68}$$

$$v_D = \sqrt{\frac{2qE_A s_A}{m}} \tag{69}$$

$$t_D = \frac{D}{v} \rightarrow t_D = \frac{D}{\sqrt{\frac{2qE_A s_A}{m}}} \tag{70}$$

$$t_D = \frac{D}{\sqrt{\frac{2qV_A}{m}}} \tag{71}$$

Where V is the acceleration potential in volts. s_A and D stand for the acceleration space and the drift distance, respectively. Consequently, the overall flight time of the ion is $t_0 + t_A + t_D + t_d$ (μs). t_0 and t_d denote the times that it take for an ion arrives at the ionization point and to be detected at the detector, respectively (*17, 35, 102*).
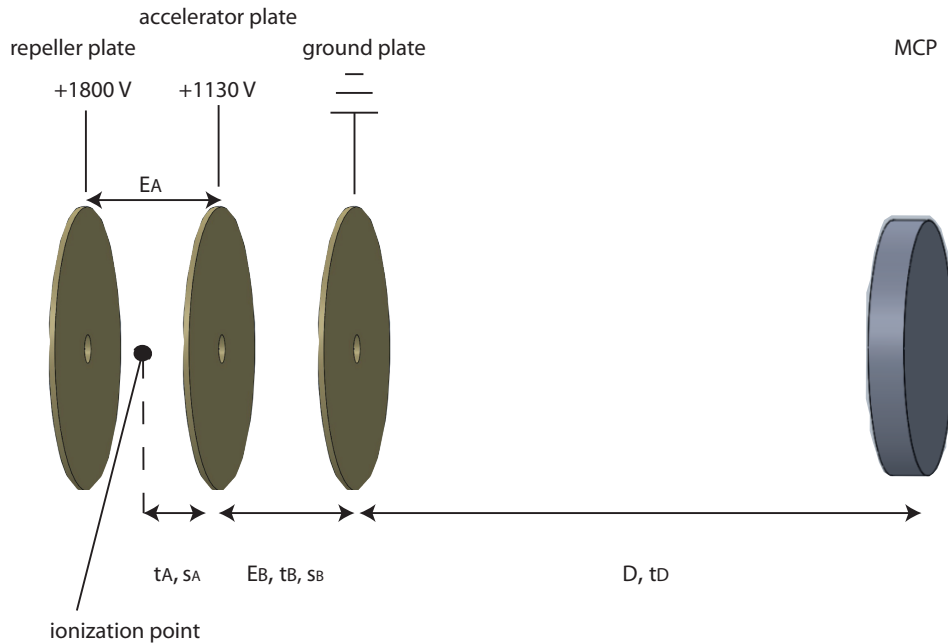

Figure 10- A two-stage ion source configuration.

It is also possible to enlarge the flying distance (D) by converting the ion source into two-stage (Fig.10). Such an ion source has two acceleration spaces. The employed ion source in our set-up is also based on the two-stage configuration. As a result, the total flight time includes also the time that the ion spends in the second electric field. The kinetic energy of the ion that enters the second acceleration region is $qV\text{-}qV_B = qV_A$, where, $V = V_A + V_B$ (V_A and V_B are acceleration potentials for electric fields E_A and E_B, respectively) (*102*). By considering s_B as the second acceleration space, Eq.72 and 73 can be derived as:

$$t_B = (\sqrt{V} - \sqrt{V_A})\frac{s_B}{V_B\sqrt{q/2m}} \quad \text{or} \tag{72}$$

$$t_B = (\sqrt{s_A E_A + V_B} - \sqrt{s_A E_A})\frac{1}{E_B\sqrt{q/2m}} \tag{73}$$

- *Resolution of TOF-MS:*

Generally speaking, the resolution of a TOF spectrometer depends on the formation of ions. If all ions are formed at the same time and same position, they face similar electrostatic fields. Therefore, the ions have no initial velocity, resulting in specific arrival time at the detector for all the ion with a similar ratio of *m/z*. In this case, the resolution of TOF-MS is defined by the detector. However, in reality, the resolution depends on the initial velocity of the ions (energy resolution) and the spectrometer capability of reducing the temporal distance caused by the spatial distance (space resolution). The common way to define the resolution of a TOF-MS is to consider the largest mass which can be completely distinguished from the adjacent masses. This ability is identified by the mass resolving power:

$$R_{FWHM} = (m/z)_{empirical} / \Delta (m/z)_{FWHM} \tag{74}$$

Where *m/z* denotes the peak center of the specific mass while $\Delta (m/z)_{FWHM}$ is the full width at the half maximum of the peak (*103*). The equation can be extended for the time domain with considering $m = A\, t^2$, where *A* is a constant. The Eq.74 will be evolved to:

$$R_{FWHM} = (m/z)_{empirical} / \Delta(m/z)_{FWHM} = t/2\Delta t \tag{75}$$

The early linear TOF-MS was poor in the resolution. However, thanks to numerous calculations, modifications of the spectrometers and improvement of the resolution of TOF-MS were plausible. The reasons for such a poor resolution can be sorted into three main phenomena. First, the finite time for the formation and extraction of ions, which ends in the temporal effect. Second, the restricted volume for the formation of ions, which results in the spatial distribution effect. Thus, ions will have different potential energies and consequently different kinetic energies. On that account, ions with identical mass have different flight times. This time is also affected by the initial different positions in the acceleration field. Third, the initial velocity of ions which is caused by the initial velocity of the neutral ions or gained kinetic energy within the fragmentation process. The last reason can be divided into two effects itself, namely a pseudo-temporal and a pseudo-spatial. The spatial one can be compensated by the space focus, whereas, the temporal effect can be corrected by, for instance, the high voltage used for pulsing the acceleration field.

There is a point located in the drift region of TOF, where the ions which possess higher energy are passing the ions with lower energy which have been in the electric field for shorter times.

This point is a narrow space and is called space focus. The first-order space focus is a point in the drift region where the linear part of the potential energy will vanish. By locating the detector at this point, one can compensate for the effect caused by a pseudo-spatial as well as initial space distribution. The two-electrode ion source will not give a very well corrected mass resolution because it cannot cover the whole distance of the drift region. Whereas, the two-stage ion source built of three electrodes (two fields) gives a possibility to adjust the space focus for longer distances (*17*). Unlike, the first order space focus, which can be controlled by applied voltages on the electrodes, the second-order focus point is fixed and determined by the relation between the space of the electric fields (distance between the electrodes). In the second-order focus point, not only the linear but also the quadratic term of the potential energy disappears (*102*).

3.1.5. Deflectors and einzel lens plates

Deflector plates and einzel lens plates are both implemented after the acceleration fields into the ion source to steer back the ions beam to the original axis. Hence, the ions fly, again, collinearly to the ion source and the detector. The deflector plates consist of a ground plate and a charged one. Two sets of deflectors are used to correct the ion path, namely vertically and horizontally, as shown in Fig.11a. The einzel lens contains five electrodes, including a centered charged and the four grounded (Fig.11b). The fields applied within the deflector and the einzel lens plates are symmetric, therefore, ions are not accelerated, but the deprivation in their routes is compensated, which leads to better ion yields.
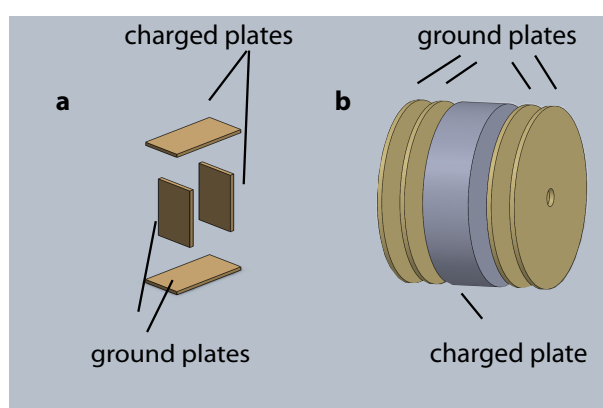

Figure 11- The schematic view of the deflector plates and einzel lens. a) each set of deflector plates consist of a ground plate and a charged one. b) einzel lens is made of five electrodes, including a charged one located in the middle and ground plates surrounding the charged one.

3.1.6. Micro-channel plates (MCP)

The ions, after flying through the drift region, are detected at the end of the TOF tube by a micro-channel plate (MCP). An MCP is an array of about 100 micro electron multipliers with the diameter size of 10-100 μm, which are arranged parallelly (*104*). Therefore, the surface of the detector should be a planner and parallel to the ion beam. An MCP has the capability to detect a poor ion current and multiply it via a secondary emission process. To have a precise performance of the MCP, it is necessary that all ions arrive at the anode of the detector at the same time. In addition, the amplifier circuitry needs to be fast enough to respond to the short charge-pulses (*35*).

3.1.7. Mass calibration

The signals, coming from the detector, are collected by the oscilloscope (WaveRunner 610 Zi, Teledyne LeCroy, 1GHz and 20 GS/s). The spectra, recorded on the oscilloscope, are time-based. To calibrate the spectra based on the mass, one can use the following equation (*105*):

$$m = k\,(t_m - t_0)^2 \qquad\qquad (76)$$

This equation is derived from the kinetic energy of the ions (*106*) that indicates the quadratic relation between mass and time. *k* here is the constant which is dependent on the ionization point, ion source geometry and applied voltages. t_0 here, stands for the digital delay time of the cable and electronics, while, t_m is the time at which the corresponding signal is appeared on the oscilloscope.

3.1.8. Laser systems

Lasers became popular among scientists because they overcame most of the limitations of the conventional light sources, such as power, monochromaticity, coherence and polarization (*107*).

Throughout this thesis, different laser systems were employed. There are categorized into two groups including solid-state lasers and dye laser systems.

- *Solid state lasers:*

The Nd: YAG (neodymium-doped yttrium aluminum garnet; $Nd:Y_3Al_5O_{12}$) crystal is normally used as a lasing medium for solid-state lasers. In this study, an Nd: YAG laser (Split Light Hybrid systems, Innolas, 30 Hz) were used to pump the dye laser system. This Nd: YAG laser is a hybrid model with a diode-flash lamp combination. The resonator contains a diode and an Nd: YAG crystal rod. A single transverse oscillation mode (TEM_{00}) is adopted for the resonator which gives a Gaussian beam profile. The pre-amplifier and amplifier laser crystal rods are both pumped with the same flash lamp. A Pockels cell was integrated into the system for Q-switching. The Nd: YAG rods produce infrared laser light (1064 nm). This wavelength can be converted into 532 nm (SHG), 335 nm (THG), 266 nm (4HG) and 213 nm (5HG). The harmonic generation crystals are made of KTP or KD*P. Based on the laser dye solution and the desired wavelength range, 532 nm or 355 nm can be guided into the dye laser system.

- *Dye lasers:*

The dye laser found its place rapidly among the scientists, due to the flexibility and the narrow bandwidth of the output. It can be tuned over a wide range and can be pumped continuously or pulsed. The compatibility of the output which can be collimated with other nonlinear optics system broadened the range of its application. The principle of the dye laser operation is based on organic dyes as the gain medium. The dye molecules are excited to the excited level (S_1). Then, vibrational energy will be released via internal conversion. Finally, the lasing radiation happens from S_1 to S_0. Because of the short lifetime of such emissions, a large number of molecules should be excited at almost the same time. In addition, the gain provided by the dye solution system should be large enough to compensate for all the loses occurring due to the optical cavity and absorption of the molecules (*107*).

Here, by combing an Nd: YAG laser as a pumping laser with FineAdjustment dye laser system, different wavelength ranges and diverse power output were achieved. For all the measurements, done with this system as an excitation-ionization laser, Coumarin 153 (C153) solution was used. The concentrations of 1.6 g/l and 0.32 g/l in ethanol for the resonator and amplifier were prepared, respectively. If the solution is pumped with 355 nm, 15% efficiency will be expected. The peak emission for this dye, under such a condition, is 535 nm and it covers a range from 517 to 574 nm. In order to have a UV range as the output, a frequency conversion unit was implemented into the system. Such a conversion via doubled frequency is an SHG process, which

is achievable with a nonlinear optical crystal (e.g. BBO). The residual of the original wavelength is separated by a set of prisms, called Pellin-Broca. The spectral linewidth for this dye laser system is 0.04 cm^{-1} with an output of 11 ns. The energy of the laser pulses can be varied by the intensity of the flash lamp.

3.1.9. Twin-peak technique

One of the challenges in a REMPI experiment is the laser pulse to pulse fluctuations. Due to the fact that REMPI is a nonlinear process, the mentioned fluctuations give an asymmetric statistical distribution of the ion signals (*58*). To avoid that, one can take advantage of performing REMPI with one single shot. As shown in Fig.12a, the single shot ionizes the first plume of molecules at position *A* in the ionization/acceleration region of the ion source and being reflected into the ionization region by a mirror (0° reflection), installed at the other side of the set-up. The reflected laser shot ionizes the next plume of the molecules, somewhere at position *B* which is close to *A*. If the distance between *A* and *B* is big enough compared to the FWHM of the signals created at positions *A* and *B*, the mass spectra of both ionized plumes can be merged in one mass spectrum with a slight shift for the same masses, as indicated in Fig.12b. Therefore, one can claim that ionization of two molecular clouds with one laser shot is plausible. Moreover, this method can be combined with CD-REMPI, which alters the systematic errors of measured g-values caused by laser fluctuations. The only required change is to make the laser beam circularly polarized. Each handedness is switched to the other one by reflection at the 0° mirror (*55, 108*). Thanks to this reflection, one single shot goes through both handednesses of the circularly polarized light. Thus, the equation of the g-value is evolved either to Eq.77 or 78, depending on the initial handedness of the circularly polarized light:

$$g_{LR} = 2 \, \frac{I_{L,signal\ at\ A} - I_{R,,signal\ at\ B}}{I_{L,signal\ at\ A} + I_{R,signal\ at\ B}} \tag{77}$$

$$g_{RL} = 2 \, \frac{I_{L,signal\ at\ B} - I_{R,signal\ at\ A}}{I_{L,signal\ at\ B} + I_{R,signal\ at\ A}} \tag{78}$$

Where, g_{LR} shows the evaluated g-value when the incoming beam is left circularly polarized, while g_{RL} shows the g-value evaluated contrariwise. I_L and I_R stand for the ion yields created by left and right circularly polarized light, respectively. As a result, an individual g-value can be extracted from each mass spectrum.
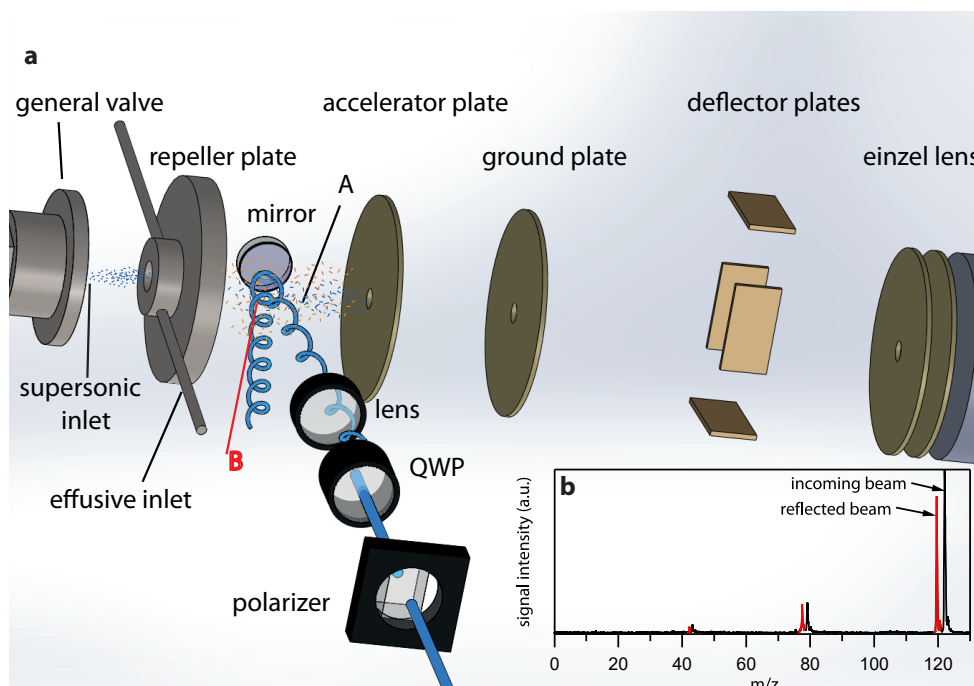
Figure 12- a) a schematic view of the twin-peak experiment. Linearly polarized light is altered by a QWP into circularly polarized light. The incoming beam ionizes first molecular cloud at A (both supersonic molecular and effusive beam). The reflected beam with the other handedness of the circularly polarized light ionizes the second cloud at B. b) a mass spectrum of a twin-peak experiment. The black peaks are the ion yields at the position A and red peaks are the ions resulted from the position B.

3.1.10. Experimental procedure and setting

The volatile chiral molecules are injected into the gas phase through the pulsed general valve and via the effusive beam inlets. The pulsed general valve has a nozzle diameter of 0.2 mm and operates at 30 Hz repetition rate with 250 V and 40-120 μs pulses. The Ar backpressure used for the supersonic expansion is 2.8 bar. As already mentioned before, a part of the gas line connected to the valve, stores the sample. Since the investigated molecule here, was liquid at room temperature, a few drops of the sample were put onto the glass wool, which was subsequently placed in the sample compartment. In case of the effusive beam, either a small flask or a small Swagelok plug is used as the sample vessel. The working pressure of the chamber differs, based on the kind and number of simultaneous active inlets. In case both pulsed general valve and effusive beam inlet are in use, the working pressure is regulated at $5 \cdot 10^{-5}$ and $4 \cdot 10^{-6}$ mbar, for inlets/ionization part and TOF tube, respectively.
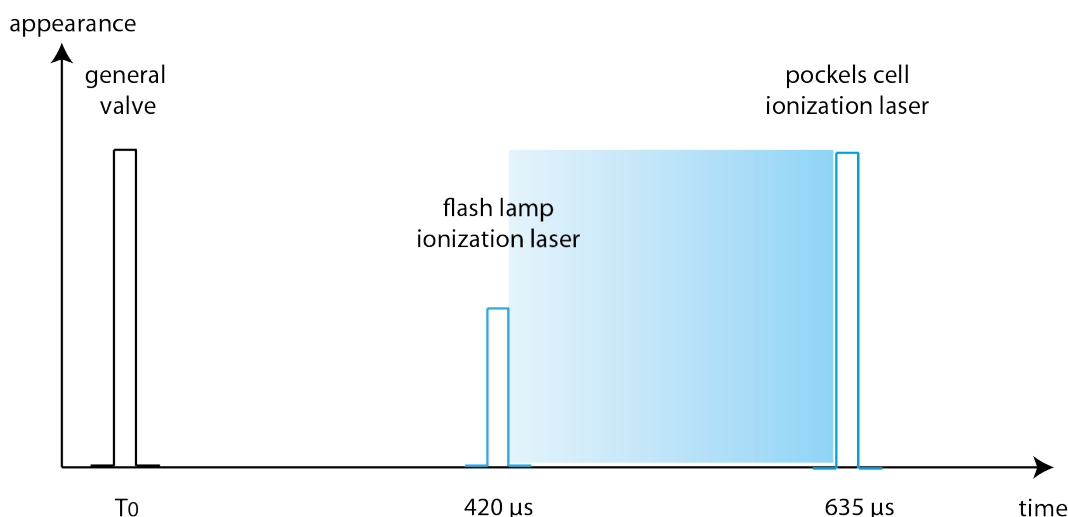
Figure 13- The schematic plot of the time synchronization, used for the gas phase laser spectroscopy measurements.

(R)-(+)-1-phenylethanol was investigated in the supersonic beam due to the fact that the cooled molecular beam was required to achieve high vibrationally resolved spectra. The achiral volatile molecule, which was used as a reference substance, was phenol. Phenol was introduced into the chamber via the effusive beam inlet. Thanks to the high volatility of phenol, it was vaporized into the gas phase, very fast. The cooled molecular beam of (R)-(+)-1-phenylethanol and the warm phenol plume, were ionized by the laser, subsequently, accelerated in the electric field (continuous fields). Afterward, the ions flew within the deflector plates, einzel lens plates and the TOF tube towards the MCP. The MCP converted the current of ions into the readable signals for the oscilloscope.

Table 1- Applied voltages on the electrodes in the ion source and TOF.

Repeller plate	+1800 V
Accelerator plate	+1130 V
MCP	-2100 V
Vertical deflector	+550 V
Horizontal deflector	0
Einzel lens	+100 V

Both, the general valve and the laser are triggered externally with 30 Hz. To ionize the molecules at the right moment, the pulsed general valve and the dye laser system need to be synchronized. This synchronization is necessary in order to have the laser beam in front of the nozzle of the

pulsed general valve, a few microseconds after it released the cooled molecular beam. This is not the case for the effusive beam inlet, because that molecular plume exists in the chamber as long as the inlet is open. The applied delay times via a pulse delay generator (Stanford research instrument, DG535) are indicated in Fig.13. In addition, all the applied voltages of the ion source, during the measurements are summarized in the Tab.1
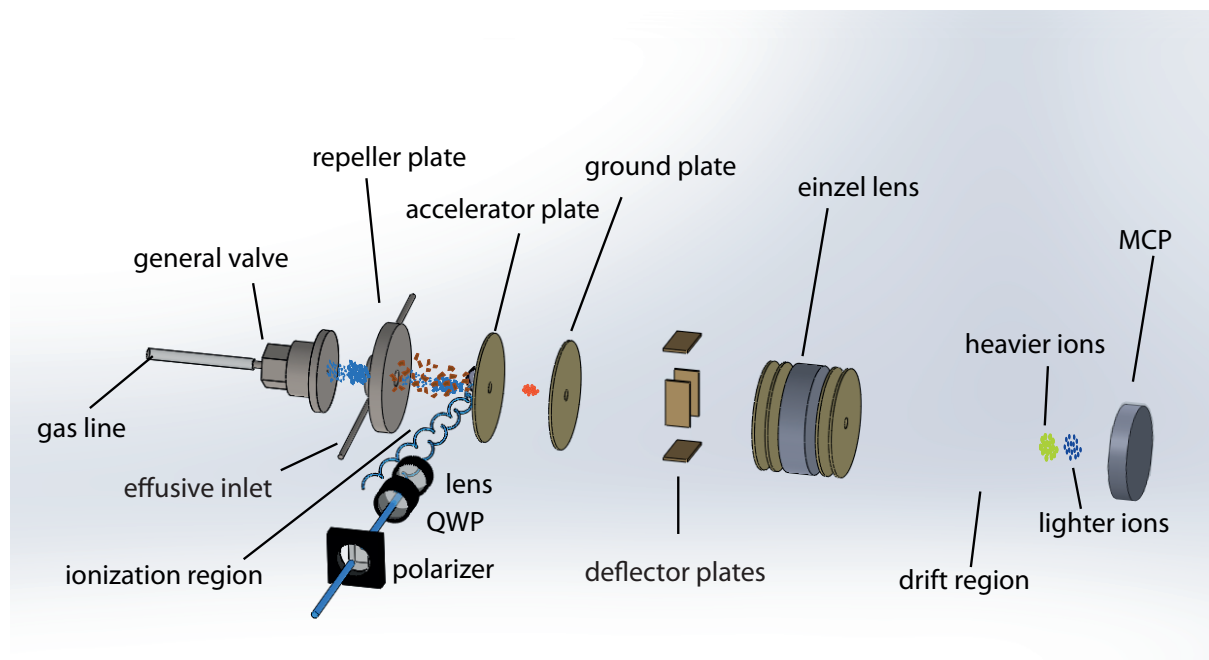

Figure 14- The employed ion source for the gas phase laser spectroscopy experiments. A seeded carrier gas goes through supersonic expansion via a pulsed general valve. Then, the cooled molecular beam (blue) is wrapped by a warm molecular beam (brown), coming from effusive beam inlets. Here, the ionization laser beam ionizes molecules via the twin-peak technique. The ions (red) are accelerated within the two-stage ion source (two electric fields). Furthermore, the accelerated ions pass the deflector plates and the einzel lens to be aligned, collinearly to the MCP. After flying through the drift region (field-free region), the ions arrive at the MCP, temporally separated, based on their masses.

The ion source configuration in addition to the laser path for the set-up is shown in Fig.14. The output of the dye laser system is guided towards the set-up (ionization region). A photo-diode records the intensity of the beam for further data processing (see section 3.1.11). Before it entered the chamber, the linearly polarized light is converted into circularly polarized light by means of a QWP or a PEM. Finally, it is focused by a lens (f = 250 mm) inside the chamber, somewhere in front of the repeller plate (ca. 5 mm). The distance between the nozzle of the pulsed general valve and the ionization point is estimated to 10 cm. The circularly polarized light ionizes the molecules and goes out from the other side of the chamber. There, in order to apply the twin-

peak technique, it is reflected back by a mirror (0° reflection) and focused (f = 200 mm) into the chamber, again. The back-reflected beam has the other handedness of the circularly polarized light, thanks to the 0° reflection. The focal point for this beam is located closer to the nozzle of the general valve, compared to the incoming beam.

The absorption spectrum of (R)-(+)-1-phenylethanol over the range of 259-266 nm (500-600 $\mu J/mm^2$) was obtained by one colour (1+1) REMPI-MS, corresponding to the $\pi \rightarrow \pi^*$ transition of (R)-(+)-1-phenylethanol. For that purpose, the dye laser system with the dye solution of C153 was employed to scan over the range. The FineAdjustment LabView program of the FineAdjustment dye laser system has been complemented with an additional program which performs the wavelength scan over the desired range. This program communicates with a smaller oscilloscope (TDS 3032B, Tektronix, 300 MHz, 2 GS/s) that needs to be used for the scan measurements. After the recognition of vibronic transitions in the absorption spectrum, one colour (1+1) CD-REMPI was conducted on the peaks appeared at 262.13 nm and 262.11 nm, in order to compare the g-values of these transitions. The data acquisition was done for approximately 100,000 shots for each handedness of circularly polarized light. A home-written LabView program was calculating the g-values for the twin-peak measurements.

- *Operating quarter wave plate (QWP) and photo-elastic modulator (PEM):*

In order to convert linearly polarized light into circularly polarized light, a QWP (B Halle) or PEM (PEM 100, Hinds instruments, 50 KHz) can be used. To do so, the initially linearly polarized light (P or S) is essential, therefore, a polarizer has to be implemented in front of the QWP or a PEM. For instance, in the case of the QWP, in order to find the proper configuration (rotation angle), one can use another polarizer after the QWP. Linear light with one polarization (P or S) can be blocked totally with the second polarizer, which has a 90° rotation corresponding to the first polarizer. That means, the two polarizers are perpendicular to each other and blocking both linear polarizations of light. Hence, a photo-diode used to detect the beam intensity after the second polarizer shows negligible intensity. This condition is fulfilled if the QWP is at the linear configuration. Now, the QWP is rotated by a motor and the intensity of the light after the second polarizer is tracked. At the motor steps and the corresponding angles, where the intensity is maximal, the linearly polarized light is converted into the circularly polarized light. Therefore, the fast axis plane of the QWP is at 45° with the light plane. Each maximum stands for one of

the handedness, as showed in Fig.15a. In the case of the PEM, the very similar procedure can be applied, however, here the PEM is installed at a 45° in accordance with the polarization plane of the incoming laser light. The delay between the oscillation of the PEM (eigenfrequency of ~50KHz) and the laser pulse (repetition rate of 30 Hz) defines the outcoming polarization. Therefore, the trigger of the laser with the defined delay time is crucial and controlled by a home-made trigger box. The intensity of the outcoming light as a function of the delay time is presented in Fig.15b. The interpretation of the curve and finding a proper setting (delay time) for the circularly polarized light is analogous to the case of the QWP.
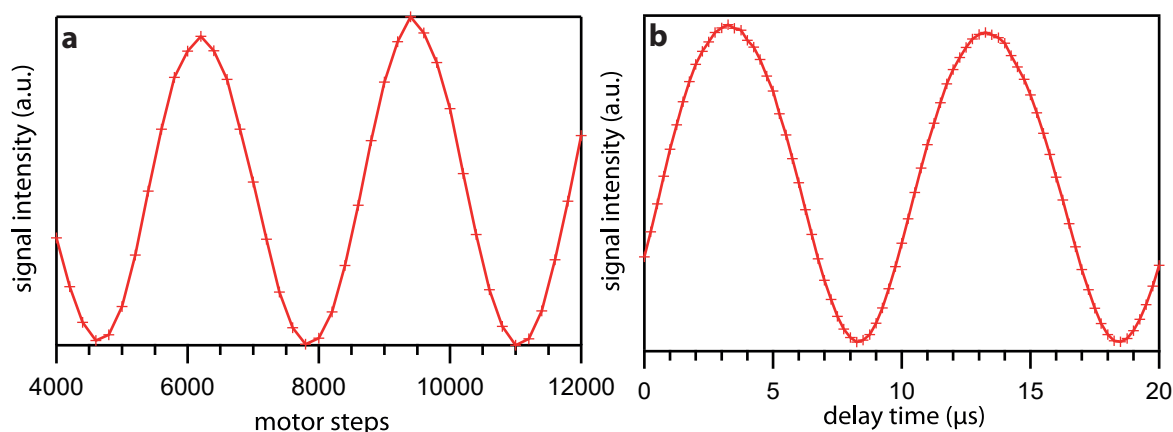

Figure 15- Calibration of a) QWP and b) PEM for creating circularly polarized light. The QWP is installed on a rotary motor. Circularly polarizations (the peaks in the spectrum) are achieved at specific steps of the motor (angles of the QWP). The PEM is working in cooperation with a trigger box, therefore, at the specific delay times, the desired handedness is gained.

3.1.11. Processing data

As briefly explained in the previous section, twin-peak measurements provide all the information that one requires to calculate the g-value. One single shot, individually, indicates the g-value. However, there exist some limitations, including the discrepancies between the energy of the incoming and reflected laser beams and the density of the molecular clouds at position A and B (Fig.12a). The former one is caused by the loss of energy at each optical component and windows of the chamber. All these limitations result in so-called systematic errors, which essentially needs to be suppressed. To compensate such kind of errors, two correction methods can be applied. The first one is performing the analogous experiments, simultaneously on the achiral reference molecule, which has a zero g-value and similar absorption properties to the investigated chiral

molecule. By subtracting the evaluated g-value of a chiral molecule from the reference molecule, the fake g-value is excluded (*57*).

$$g\_value_{corrected} = g\_value_{chiral\ molecule} - g\_value_{achiral\ molecule} \qquad (79)$$

The second method is that the initial circular polarization of the incoming laser beam is swapped after a few shots, e.g. 200 shots. Then, after a few sets of data acquisitions, the g-values which are calculated through initial left circularly polarized light (g_{LR}) are sorted in a descending trend (decreasing systematic error contribution), while the g-values which are resulted from initial right circularly polarized light (g_{RL}), are sorted in an ascending trend (decreasing systematic error contribution). For the correspondent laser intensity and molecular beam density, it is assumed that the calculated g-values should have had equal values with the opposite signs, because of the different handedness of the incoming laser beams (g_{LR} or g_{RL}). Hence, the sorted g_{LR} and g_{RL} are paired and averaged, subsequently, to eliminate the systematic errors. The averaged values are once again averaged to give the final averaged value, which is reported in this thesis as a g-value. It should be noted that additional filters are also applied on the data points; e.g. small ion signals compared to the noise level caused by low laser intensity are excluded from the evaluations. Therefore, the corresponding g-values for such signals are not considered (*13*).

3.2. **Laser desorption of non-volatile chiral molecules**

As already explained in the introduction section, by facilitating TOF-MS to the desorption part, one can take advantage of analyzing all kind of molecules even non-volatile ones in the gas phase. The laser desorption happens in front of the nozzle of the pulsed general valve, where desorbed molecules can be subsequently carried along with the carrier gas. Within this process, thanks to the supersonic expansion and collisions happening between desorbed molecules and carrier gas, the internal energy of the molecules are cooled off, leading to a cooled molecular beam of desorbed molecules in the gas phase (*109*). In the following, preliminary work on the laser desorption with a prototype set-up as well as the integration of the desorption part into the main set-up, which was explained in section 3.1, are described in detail.

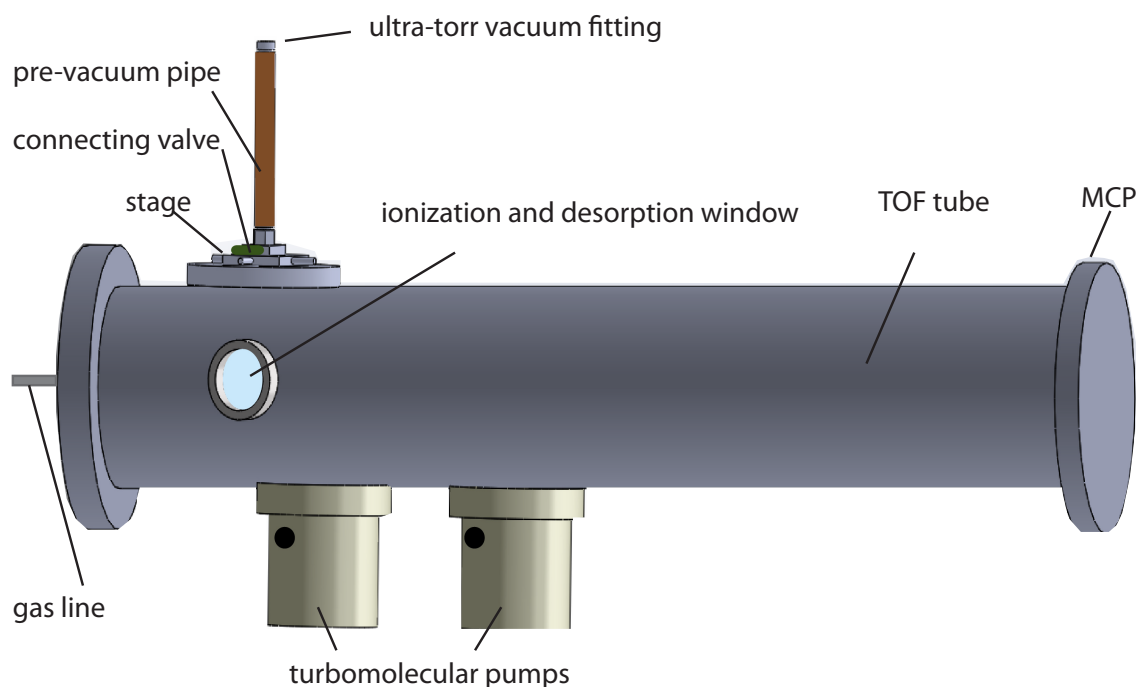### 3.2.1. **A prototype apparatus of the laser desorption**

Figure 16- A schematic view of the prototype set-up of the laser desorption.

The prototype apparatus including TOF-MS was used for the preliminary work on the laser desorption. As it is shown in Fig.16, the set-up consists of the main chamber connected to the 85 cm TOF tube. The whole set-up is pumped down with two turbomolecular pumps (TMU 260,

Pfeiffer vacuum) to $5 \cdot 10^{-7}$ mbar. The main chamber contains the Teflon block, which is attached to the pulsed general valve (Parker valve) from one side, and from the other side to the ion source. The ion source is installed on the Teflon block, collinearly to the pulsed general valve, as depicted in Fig.17. The ion source consists of a repeller plate, an accelerator plate and a ground plate, sequentially. This is by definition a two-step ion source. The MCP is installed collinearly to the ion source at the end of the TOF-MS tube to detect the produced ions. Unlike, the ion source explained in section 3.1.4, the electric fields are pulsed here, in order to have the acceleration for the desired ions coming from the desorption. The main task of the Teflon block is to intersect the desorption rod via its vertical groove and the desorption laser through the horizontal one. The pulsed general valve carries He (5.0, 99.999 vol% He) as a carrier gas for the desorbed molecules at the intersection in the Teflon block. The sample rod is inserted to the system via a pre-vacuum pipe (see Fig.16). The pipe is connected to the manipulator via a ¼" (6.35 mm) Swagelok valve. The manipulator, itself is implemented on the main chamber and helps to adjust the position of the pipe for a better insertion of the sample rod.
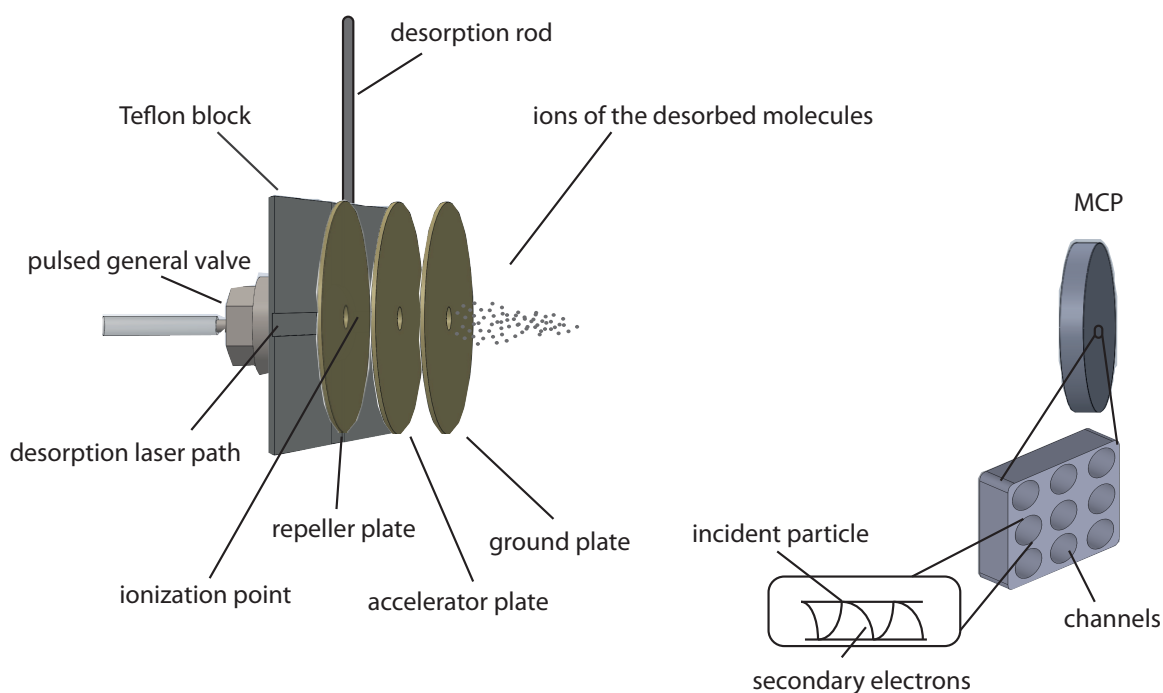

Figure 17- A two-stage ion source, used for the prototype laser desorption set-up, including a repeller plate, an accelerator plate, a ground plate and an MCP. The MCP consists of several micro-channels which amplifies the signal via a secondary electron emission process.

A rotary pump is used in order to evacuate the pre-vacuum pipe to a pressure of the low 10^{-2} mbar, before opening the valve and inserting the sample rod into the main chamber. The Swagelok fitting (ultra-torr vacuum fitting) is used to seal the pipe inlet. The sample rod as, shown in Fig.18, is used to transfer molecules into the high vacuum chamber in a vertical position.
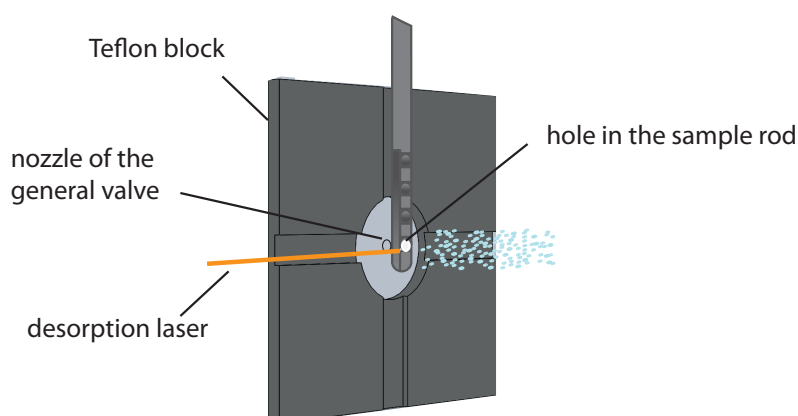

Figure 18- A schematic view of the desorption point in the prototype set-up. desorption laser, the nozzle of the pulsed general valve and the sample rod meet each other at the point which is collinear to the ion source.

- ▪ Sample rods and sample preparation*:*

There exist two different designs for the sample rod tips, which are made out of stainless steel and screwed on the sample rods. The first design, as illustrated in Fig.19b, contains a set of grooves, which enables the loading of different molecules, matrixes and mixtures for desorption. In the new design, the same grooves are used but they embody holes with a diameter of about 3 mm and a depth of 4 mm, as shown in Fig.19c. The idea behind this design is to have a volume to confine the molecular powder and compress it, without using any matrix molecules.

1,1′-Bi-2-naphthol known as BINOL (Aldrich, 99%) was chosen as a test molecule to be desorbed. Two different preparation methods, corresponding to the employed tip, were applied. The preparation in case of the first tip, with flat grooves, was as follows. A copper band was used to attach the HOPG (Highly Oriented Pyrolytic Graphite) to the surface, in the groove. A solution of BINOL in MeOH was prepared and the HOPG surface was covered with BINOL

molecules by drop coating. The preparation for the newly designed tip with holes was to press BINOL powder inside the holes.
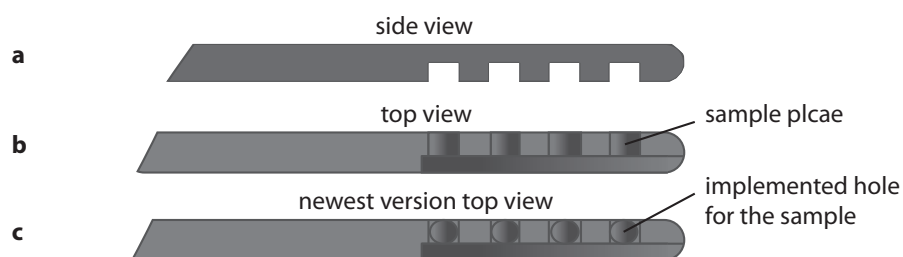

Figure 19- The sample rod tips, used in the prototype set-up for performing laser desorption. a) a general side view of the tips. b) the first version of the rod consists of 4 grooves. c) the second version (newest version) of the designed tip with holes for holding samples.

- *Laser systems:*

For the desorption, a nanosecond Scan Mate 2C (Lambda Physik, 20 Hz, the bandwidth of 0.172 cm^{-1}) dye laser system with a pumping Nd: YAG laser (Quentel) operated at 532 nm, was used. The dye laser system covered the range of 598 to 636 nm. The dye solution was a mixture of 0.17 g/l Rhodamine B with 0.04 g/l Rhodamine101 in ethanol with the maximum emission at 615 nm and 26% efficiency. The dye laser system energy was varied by changing the delay time between the flash lamp and Q-switch. The ionization laser was a Soliton Nd: YAG laser (THALES LASER, type = DIVA II, 10 Hz, 266 nm). The pulse energy was changed by the delay time between the flash lamp and Q-switch or the current of the diode. This laser has a 10 ns pulse width.

- *Experimental procedure:*

To desorb the molecules, the prepared sample is implemented, vertically inside the chamber, and subsequently in the Teflon block. The step of the tip is adjusted in front of the hole of the Teflon block, and therefore in front of the nozzle of the pulsed general valve. Whereas, the molecular surface is aligned towards the horizontal groove and to the desorption laser beam (see Fig.18). The desorption and ionization laser beams are focused through the same window to the desorption point and ionization point, respectively. The desorbed molecules are taken up by the carrier gas coming from the pulsed general valve operates with 200 V pulses (100-230 μs) and

subsequently, go to the ionization point which is ~5 mm after the repeller plate (desorption-ionization distance ~ 1 cm). The ions of the desorbed molecules are accelerated through the ion source. The latter one has pulsed fields, therefore, all the plates on the ion source are in temporal synchronization with each other as well as the lasers and the pulsed general valve. This overlap is shown schematically in Fig.20. All the applied voltages are summarized in Tab.2. Afterward, the accelerated molecules are flying through the drift region and detected at the end by the MCP (*110*). The oscilloscope (LeCroy, Wave Jet 332, 300 MHz, 2GS/s) is used to record the signals and mass spectra.

Table 2- Applied voltages for the prototype set-up.

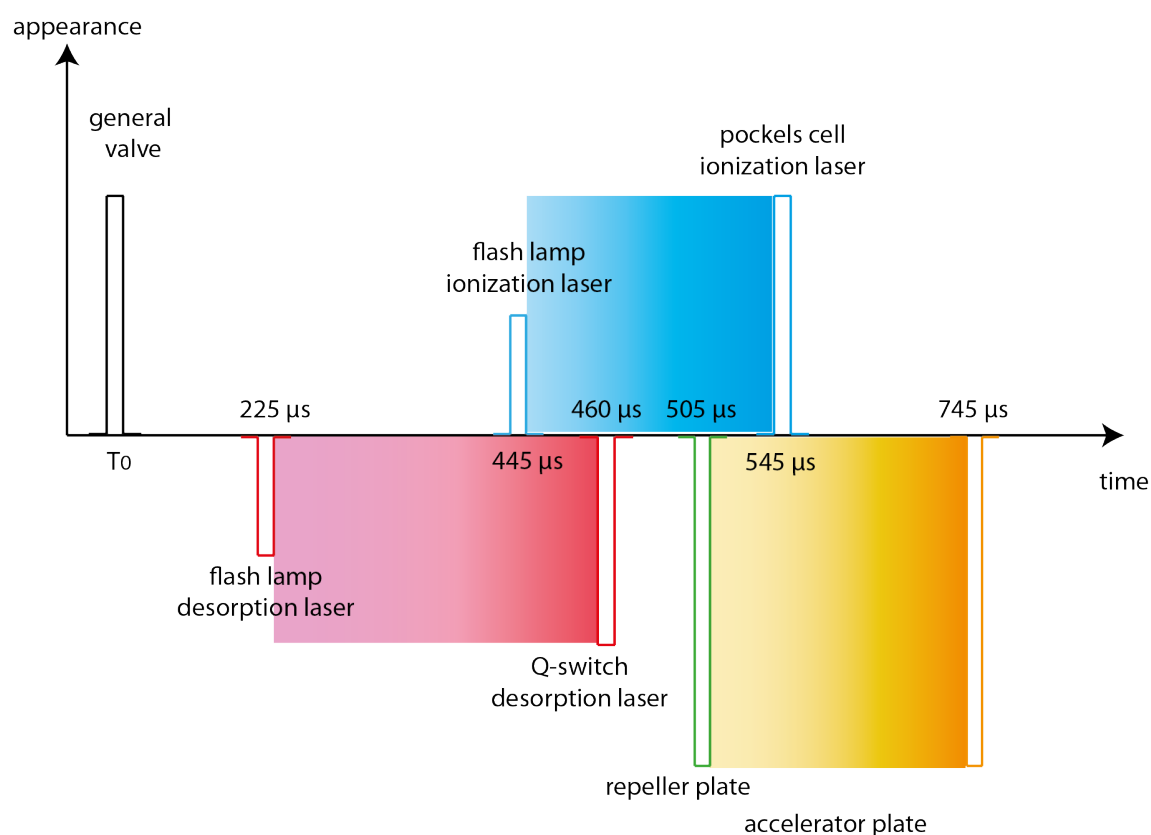| Repeller plate	+4260 V
Accelerator plate	+2620 V
MCP	-1950 V

Figure 20- A schematic plot of the time synchronization for the prototype set-up.

3.2.2. Integration of the desorption source into the main set-up

As already discussed in the previous section, imbedding a desorption source into the main set-up (section 3.1.1), facilitates the set-up of analyzing both volatile and non-volatile chiral molecules in the gas phase. Further on, it opens up access to the investigation of the intra-molecular interaction in the gas phase, e.g. induced circular dichroism (ICD), which will be discussed in more detail in section 5.

There exist numerous models of the desorption source, nevertheless they all share common components, including a carrier gas (Ar, He, CO_2, …) generally provided by a pulsed general valve, a sample holder and in some cases a channel or nozzle to guide out the molecular beam into the ionization spot. The initial laser desorption sources were introduced with the main focus on preparation methods and signal stability (*109, 111-113*). However, the cooling efficiency reported for the molecular beams was not significant and there existed some problems with the formation of clusters. To prevent this problem, new approaches were taken in designing new sources. The original idea behind all the designs was to entrain the desorbed molecules into the jet in order to have more collisions between the carrier gas and the plume of desorbed molecules before the ionization (*114*). Later on, Smalley and his co-workers introduced a waiting room to that concept (*115*), where multiple collisions happen before the jet goes through the real expansion. Saigusa et al. also implemented this concept into their set-up. They reported two different types of the desorption source, namely, 1) channel-type desorption source (Fig.21a) and 2) bare-type desorption source (Fig.21b). In the former one, the desorbed molecules and Ar gas pulses are going through the channel together and expanded via supersonic expansion, whereas, in the latter one, the desorbed molecules are going through several collision inside priorly supersonic expanded Ar gas pulses. The presented models are both suitable for laser desorption, yet the properties of the resulted molecular beams might change (*112*). In the other study done by Taherkhani et al. they combined the idea of a mixing chamber from Smalley and the sample preparations from Piuzzi to have a long-lasting desorption source with high cooling efficiency (*116*).
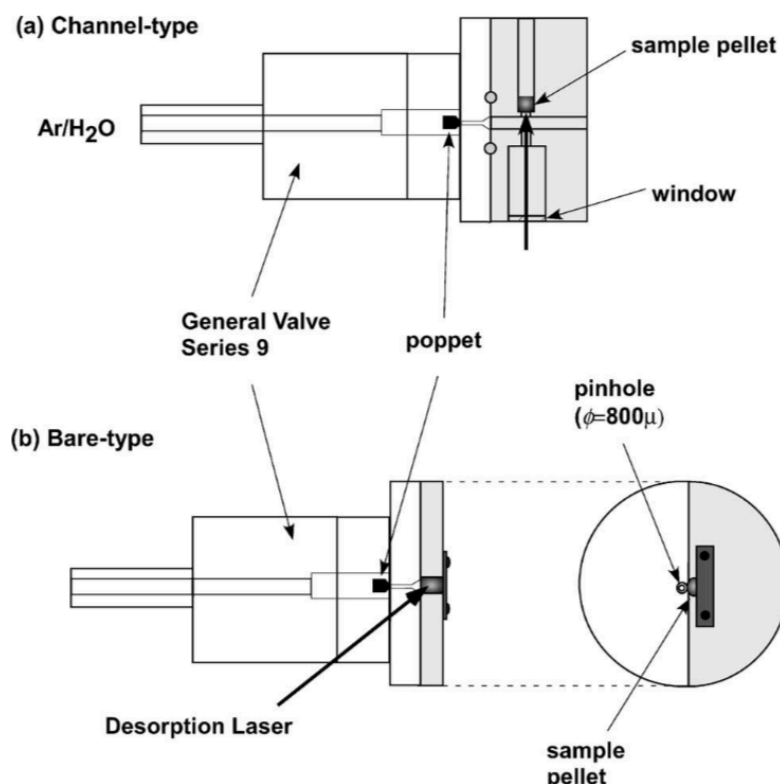
Figure 21- Two designs for the desorption source, suggested by Saigusa et al., a) channel-type and b) bare-type. The figure is reproduced from the Ref. (*112*).

In this thesis, the new desorption sources were designed to be compatible with the main set-up. The inspirations were provided by the works done by Smalley, Hitherto, Taherkhani, as well as the gained experience within the work on the prototype set-up.

3.2.3. Designing a desorption source

The first version of the desorption source includes three components as illustrated in Fig.22. The component1 has an indented part in the shape of a circle, which is compatible with the front panel of the pulsed general valve, in order to host the valve. The nozzle of the valve is adjusted collinear to the channel which goes through the whole body of the component1. This channel guides the carrier gas further. At the other side of the component1, there is another indent. This indent fits the main body of the source, component2. The side which comes into contact with the component1 has a channel which is aligned collinearly to the channel of the component1, therefore, to the nozzle of the valve. The component2 contains the waiting room as well as the path for a sample rod. The latter one goes through the whole length of the box, while the former one has a volume of $12 \, mm^2 \times 4 \, mm$. The path for the sample rod is horizontal and perpendicular
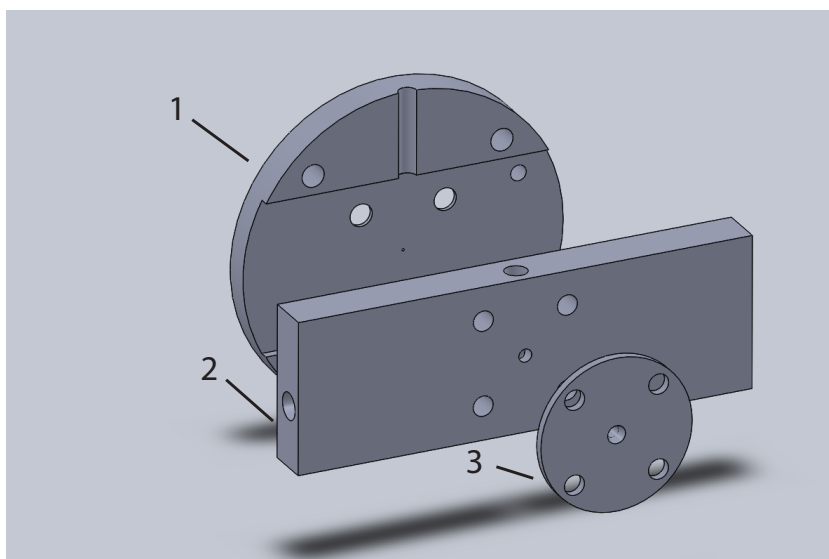
Figure 22- Different components of the first design of the desorption source. 1) the connection body to the general valve. 2) main body which includes waiting room. 3) an outlet panel.

to the other route implemented for the laser beam. The latter one also goes through the whole box in order to provide the possibility to align the laser beam coming from the top onto the surface of the sample rod, accurately. A quartz glass window (4.9 mm diameter) is placed in the path of the beam to prevent the escape of the desorbed materials and also to help sealing the waiting room for a better collision and the subsequent expansion. The diameter of the laser path is larger at the top part (5 mm) and becomes smaller (4 mm) after 3 cm. The step created by that discrepancy holds the window.
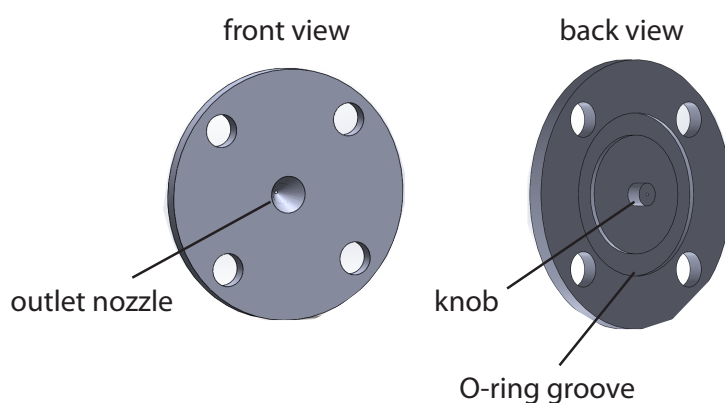

Figure 23- An outlet panel, designed for the desorption source. It provides a cony path for the expansion. The knob fits into the main body. O-ring seals outlet connection to the main body.

The created junction of the sample rod and the laser beam is called waiting room, where the collisions between the carrier gas, coming from the valve and the desorbed molecules happen. It is precisely located in front of the channel connected to the nozzle of the general valve. The component3 is removable and provides the expansion for the collided mixture in the waiting room. The hole implemented on the front side of the main body is suitable for the knobs of the component3. The nozzle which goes through the component3 is collinear to the channel in the main body and has a cone shape, as depicted in Fig.23.

In the next version of the desorption source, the first two components are merged; that helped to remove the extra channels for the carrier gas, meaning that the gas is seeded directly into the waiting room in the new design. Moreover, additional modifications were also applied, including 1) enlargement of the channel connecting the waiting room to the nozzle of the general valve (change from 0.5 mm to 2 mm). 2) reduction in the distance between the molecular beam and the molecular surface of the sample rod, by lifting the horizontal path of the sample rod (4 mm to 2 mm). One needs to consider that there is a limitation on reducing this distance, due to the fact that the sample rod can disturb the expansion trajectory. 3) enlargement of the outlet of the main body connected to the component3 (from 2 mm to 5mm). Since the sources were examined without the component3, this enlargement was made to avoid any interruptions in the motions of the molecular beam entrained desorbed molecules. The main body of the new design is shown in Fig.24.
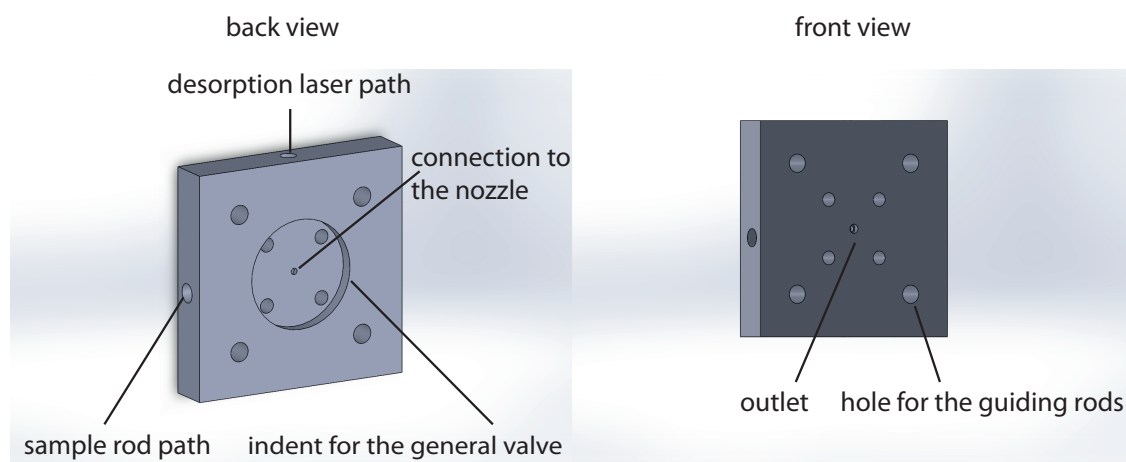

Figure 24- Back view and front views of the new design of the desorption source.

3.2.4. Required modifications to the main set-up

In order to align the desorption sources, collinearly to the ion source and TOF tube, four holes were implemented into the desorption sources. The desorption sources are mounted on four rods, which are going through the holes and make the sources fixed and stable (see Fig.24). It also helps to align the outlet in a straight line with the ion source. The distance between the desorption sources and the ion source and, consequently, the ionization point can be adjusted by moving the pulsed general vale forward or backward via its feed-though. A flange with three windows and one inlet for the sample rod was modified as a new part of the set-up (Fig.25). The distance between desorption and ionization was reduced from 17 cm to 12 cm by implementing the new flange. All three windows cover a wide range of wavelengths with a transmission > 75%. The bottom window is used in order to align the laser beam path through the desorption source. This is done to assure that the beam hit the surface of the molecules properly. The profile of the beam, without the presence of the rod, is examined underneath the bottom window (below the flange). The height of the rod inlet is adjustable (up or down) as well as the lateral position (left or right), as illustrated in Fig.25. By moving the panel, one can find the desired position, at which the rod moves easily through the desorption source without resistance. The pre-vacuum section works similar to the pre-vacuum section of the prototype model. It is (dis)connected by a Swagelok valve (1/4") to the main set-up. A fore-pump (Pfeiffer vacuum, Duo 3M) is employed to evacuate this compartment to the high 10^{-3} mbar. The rod is inserted via a Swagelok ultra-torr vacuum fitting. The O-ring, which is inside the screw, is pressed and expanded while screwing so that the sample rod inside the pre-vacuum pipe is sealed. The other alteration, which was carried out to improve the signal intensity as well as stability, was using a thinner plate as a repeller plate (identical to the other plates of the ion source). That made the distance between the desorption point and the ionization one shorter. At the same time, the distance between the ion source and the desorption point was reduced by shortening the rods of the ion source. Consequently, the distance between ionization and desorption points became nearly 6.5 cm. Accordingly, the chamber compartment was modified for a new set of windows for the ionization. The modified apparatus is illustrated in Fig.26.
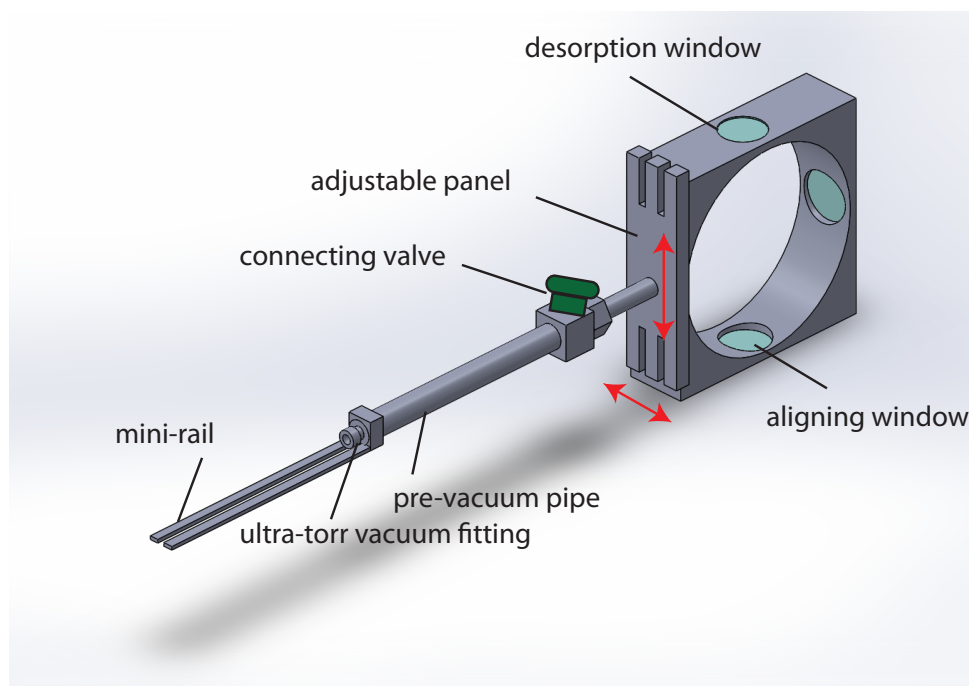
Figure 25- New desorption flange consists of a desorption window for the incoming desorption laser, an aligning window to adjust the desorption point, a moveable panel (freedom in the direction of red arrows) to adjust the rod, a connecting valve, a pre-vacuum pipe, an ultra-torr vacuum fitting and a mini-rail for guiding the rod.
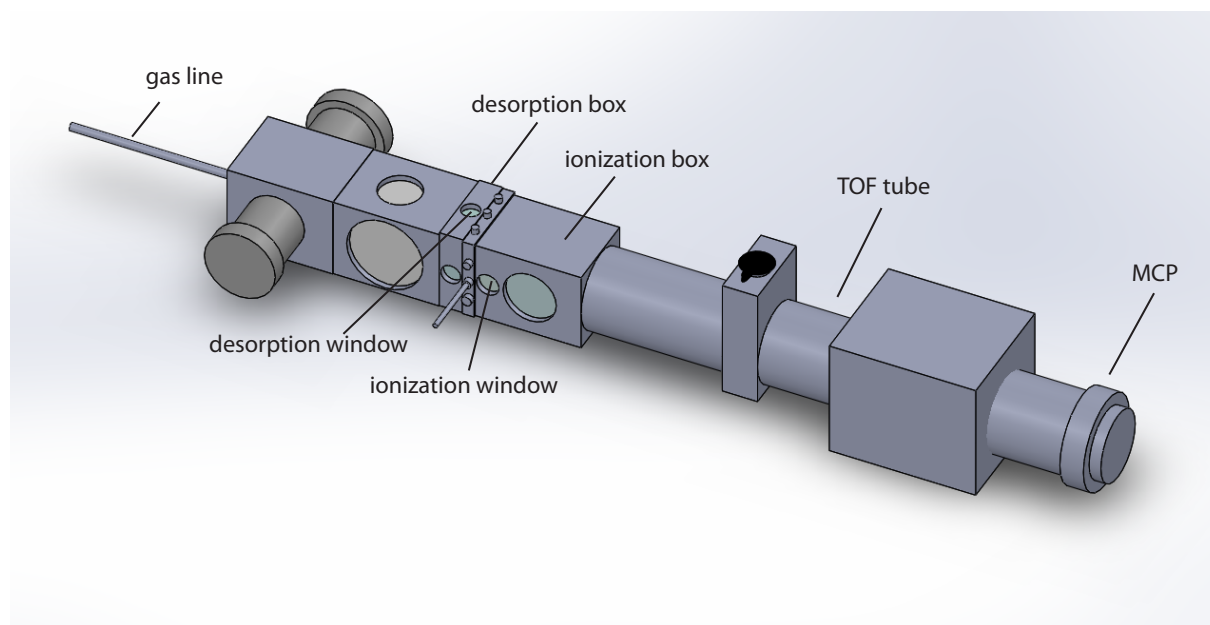

Figure 26- The modified set-up after the integration of the desorption source and the required modifications.

3.2.5. Sample rod and sample preparation

To introduce a sample into the chamber, a round sample rod with a tip, which contains a quadratic indent for the sample molecules, was designed. The length, width and depth of the indent are 50 mm, 4 mm and 2 mm, respectively, and it is made out of stainless steel (Fig.27). The rod consists of a hole at the tip, by which the position of the rod inside the desorption source is calibrated. The hole has the same diameter size as the laser beam path (4 mm). Therefore, when it is overlapped with the laser beam, the laser spot is observed below the flange of the desorption. Thus, all the positions are calibrated in accordance with the hole position. At the end of the rod, a small bar is inserted, perpendicularly. The latter one stabilizes the movement of the rod without being rotated. For that purpose, an extra mini-rail, made of two parallel rods, was added to the pre-vacuum pipe.
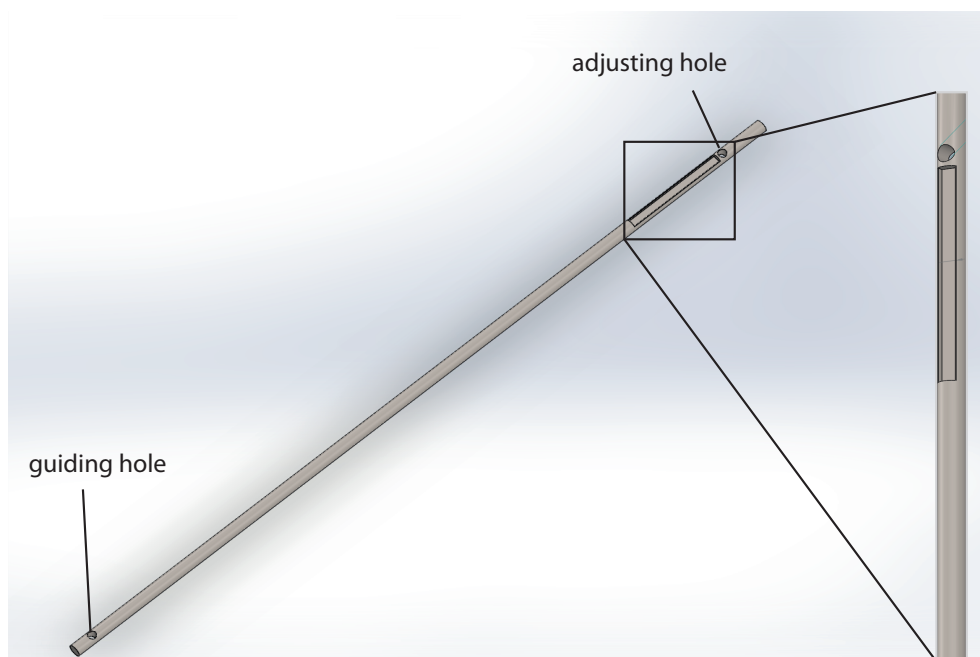

Figure 27- The new sample rod designed for the desorption source. It has two 4 mm holes. An adjusting hole for calibration of the rod at the correct position and a guiding hole for leading the rod in the mini-rail.

The investigated molecule here was 1,1′-Bi-2-naphthol, BINOL, because of the gained knowledge of that molecule via the prototype set-up. In order to prepare the sample, the indent of the sample rod was filled with BINOL powder. In order to have a flat and pressed surface, a home-made press piece was designed and made out of stainless steel. The press has the shape of the quadratic indent of the sample rod, as shown in Fig.28.
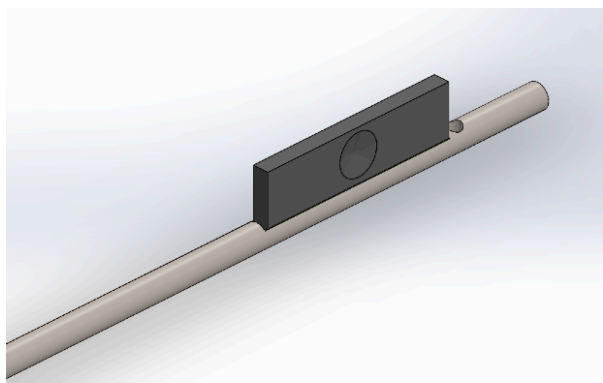
Figure 28- The pressing part used to compress the sample powder inside the indent of the sample rod.

3.2.6. Experimental procedure

All the techniques performed on volatile molecules are in principle applicable on desorbed molecules as well. The setting for the ionization process remains the same with employing a similar dye laser system and dye solution (see section 3.1.8).

The prepared sample rod is inserted into the pre-vacuum pipe and sealed by the Swagelok fitting screw. After the evacuation of the pre-vacuum pipe to 10^{-3} mbar, the connection valve between the pre-vacuum pipe and main chamber (desorption flange) is opened. Subsequently, the rod is pushed slowly into the chamber and fixed on the mini-rail to prevent any unintentional rotation. Further on, the desorption laser is guided through a cage system (Thorlabs, 30mm) and focused on the sample surface from the top and 2-3 mm away from the nozzle of the general valve. The desorption laser employed is a Scan Mate 2c dye laser system (the same dye solution and dye laser system which was used for the prototype set-up and operated at 607 nm in case of BINOL). The desorbed materials are entrained by the carrier gas, coming from the pulsed general valve, and then fly to the ionization point. There, they are ionized and fly towards the MCP, as shown in Fig.29.
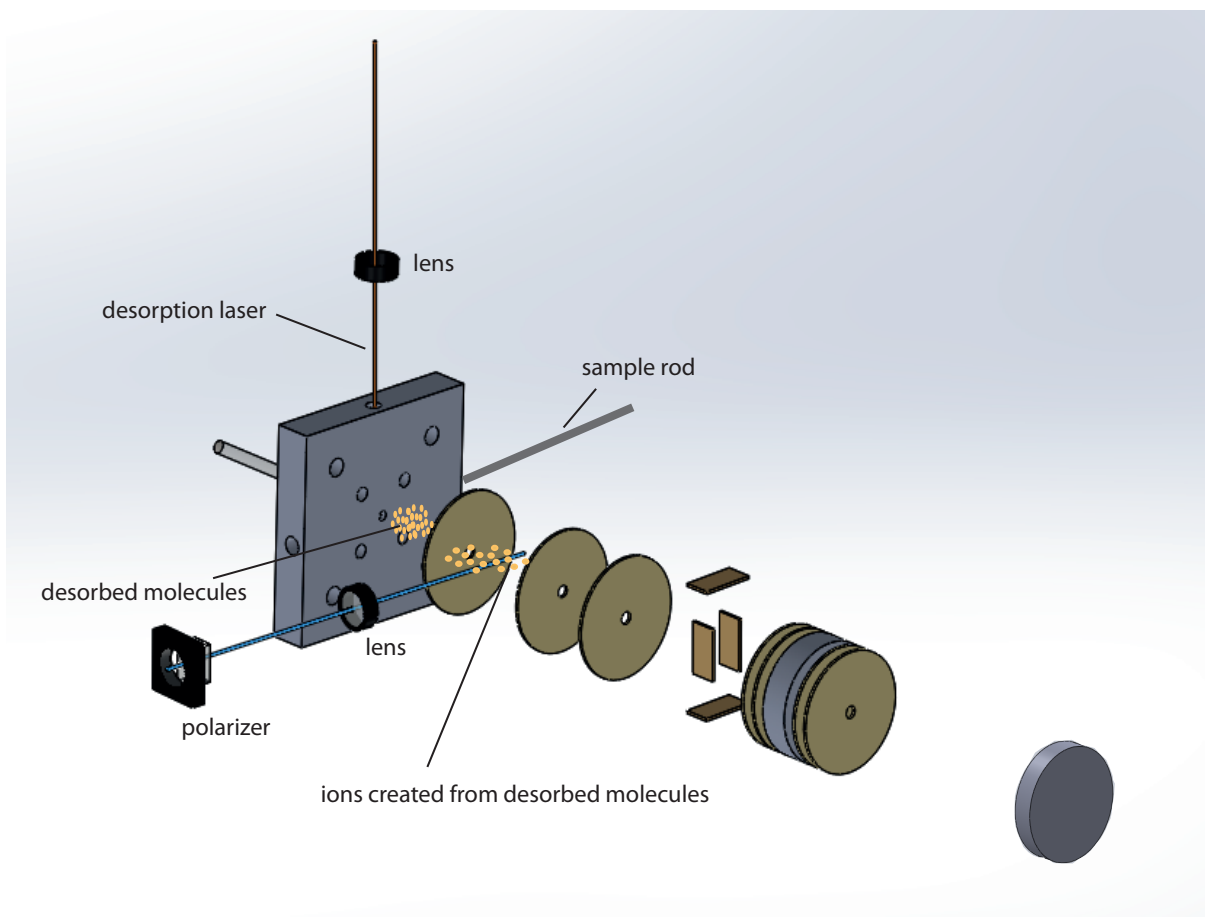
Figure 29- The ion source employed for laser desorption.

The first attempt to obtain a signal from desorbed material was with the first version of the desorption source at the distance of 17 cm form ionization point. However, no signal correlated to the desorption laser was observed. In the second try, the second version of the desorption source was integrated. This time the distance between desorption and ionization points was shortened to 12 cm and 6.5 cm, as explained before. Table 3 summarizes all the applied voltages on the ion source, while Fig.30 shows schematically the delay times applied for the set-up. To achieve such a synchronization, a pulse delay generator is employed and operated with 60 Hz. Then, signals generated from a delay box are guided to the frequency divider, where 20 Hz and 30 Hz signals are generated, corresponding to the zero time of the 60 Hz delay box. Subsequently, 30 Hz and 20 Hz signals are used to trigger the ionization and desorption lasers, respectively. In addition, the general valve is also pulsed with 30 Hz.

Table 3- Applied voltages for the set-up with an integrated part for laser desorption.

Repeller plate	+1850 V
Accelerator Plate	+1613 V
MCP	- 2100 V
Horizontal deflector	+320 V
Vertical deflector	0 V
Einzel lens	+ 450 V
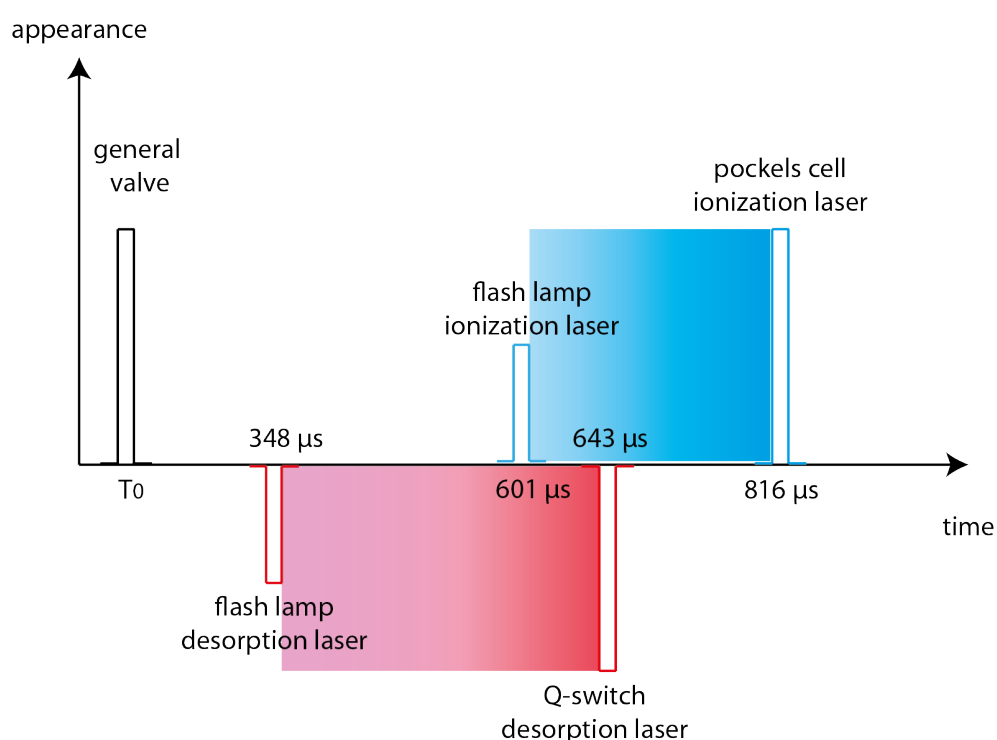
Figure 30- The time synchronization for the laser desorption experiment.

3.2.7. Automation of the sample rod

The stability of the signal from the desorbed molecules needed to be improved. To overcome the unstable signal intensity, a stepper motor was implemented into the set-up. It provides forward and backward movements for the sample rod. Throughout the movement of the rod, the desorption laser is able to scan the whole sample surface, and each shot is exposed to a new surface spot. For that purpose, a trapezoidal stepper motor actuator (DRV014) with an ability to travel 50 cm (Thorlabs) was fixed next to the sample rod inlet (below the mini-rail). The

compatible controller (BSC201 DC), along with its software (APT), is employed to regulate the parameters, such as maximum velocity, acceleration, travel distance and pitch (the distance per mm or degree that the lead screw, connected to the shaft of the motor, travels per revolution). Also, an extra part was designed, which helps the motor with the reverse movement of the sample rod, as depicted in Fig.31. The final configuration of the fixation part, the sample rod and the motor, is shown in Fig.32.
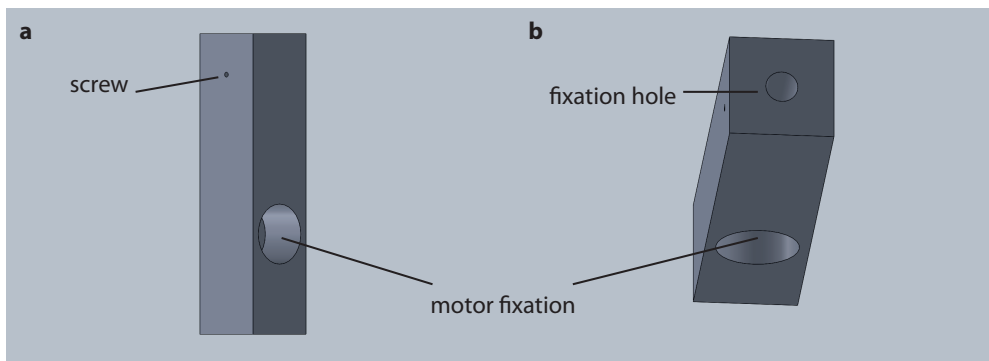
Figure 31- The fixation part connected to the shaft of the stepper motor. a) Side view of the part, the small bar connected to the sample rod was fixed with two screws. b) Top view of the part, the fixation hole is hosting the small bar. The front hole is glued to the shaft of the motor.

Figure 32- The configuration of the sample rod and the designed fixation part in order to be used with the motor. The sample rod is fixed by the extra bar via the mini-rail and at the same time is fixed inside the fixation part to the motor.

The next step was to modify the current LabView program for CD-REMPI-MS measurements in order to run the motor in parallel to the experiments. To do so, first, the APT software was added to the individual VI via the ActiveX option in LabView, with tw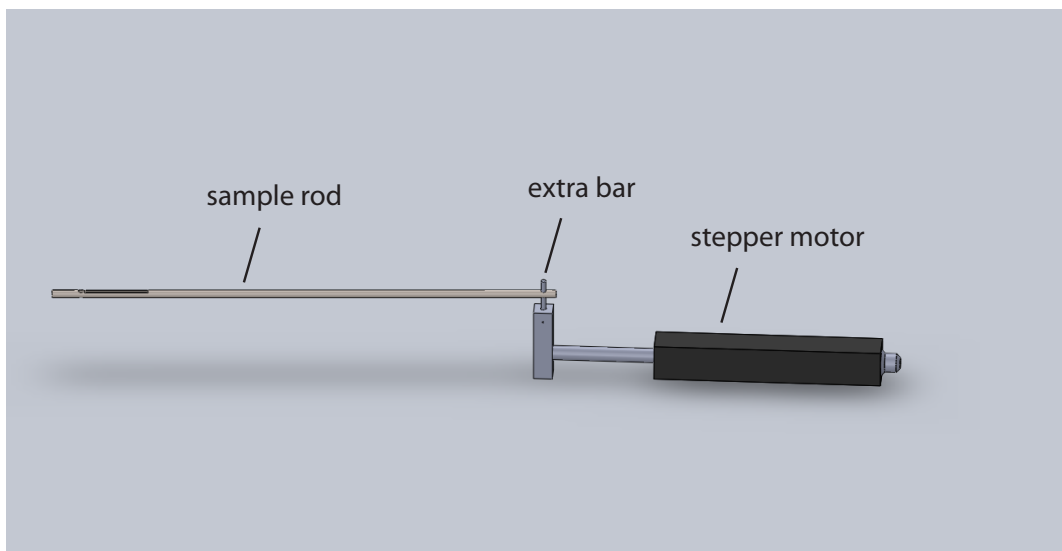o alternative running modes of continues and a single run. The former one runs the mother for an infinite number of loops till the user stops the motor, whereas, the latter one runs the motor for the fixed pre-defined number of loops. Furthermore, the velocity of the motor, acceleration speed and travel distance can be defined accordingly for each measurement. The front panel of the finalized version of the LabView program for the motor is illustrated in Fig.66 in the appendix. More corresponding detail can be found in reference (*117*).

The optimized parameters were used for data acquisitions within an automated laser desorption set-up are reported in Tab.4.

Table 4- Optimized parameters of the motor for stable signal stabilities of the desorbed molecules.

maximum velocity forward motion	acceleration Forward motion	maximum velocity reverse motion	acceleration reverse motion
0.3 mm/s	0.5 mm/s/s	0.3 mm/s	0.5 mm/s/s

3.3. Enantiospecific desorption of non-volatile chiral molecules by circularly polarized light

The objective of this section is to obtain enantioselective desorption of enantiomers of non-volatile chiral molecules by applying one of the handedness of circularly polarized light. The concept of this technique lies in different responses of the enantiomer of chiral molecules to the different handedness of circularly polarized light. Since the enantiomers are excited with different handedness of circularly polarized light, differently, thus, enantiospecific desorption corresponding to the applied handedness of circularly polarized light is possible. On that account, this phenomenon also opens up a new door towards the interpretation of the mechanisms behind laser desorption. Accordingly, this method, which is clean and independent of extra purification agent, can be versatilely used in various research fields especially in the pharmaceutical field as an alternative method for enantiomeric enrichment.

All the experiments which will be presented in this section are divided into two phases. The first phase is the desorption by circularly polarized light and the subsequent investigation of linear CD effects of the samples. The second phase is devoted to the desorption by circularly polarized light but observing the nonlinear optical activities of the samples.

3.3.1. Enantiospecific desorption by circularly polarized light and linear CD spectroscopy

The preliminary work for the enantiospecific desorption was performed in this phase. The as-bought racemic mixture of BINOL (Aldrich, 99%) was chosen for that purpose. The general experimental procedure can be divided into three steps, including the sample preparation, the desorption by one of the handedness of circularly polarized light and the analysis of the remained mixture.

- *Sample preparation*

The solution of 2 g/l of BINOL racemic mixture in methanol (MeOH) was prepared. The ending part of the Eppendorf tube was cut to use it as a substrate (5-8 mm diameter). By drop coating, BINOL molecules were brought onto the substrate. 4 drops with a volume of 10 μl were used. An extra sample for each try was prepared and called 'mother sample'. The mother sample was a reference sample and verified the optical activity of the other samples before the desorption.

▪ *Experimental procedure:*

The coated substrate was mounted on the rotatable stage which made it possible to scan the surface. For the desorption, a dye laser system (20 Hz, Scan Mate 2C, Lambda Physik AG), operated at 670 nm with the fluence of 3.6 mJ/m^2, was used. A dye solution of 0.30 g/l DCM (4-(Dicyanomethylene)-2-methyl-6-(4-dimethylaminostyryl)-4H-pyran) in DMSO (Dimethyl sulfoxide), which has a range of 625 to 685 nm with the maximum emission at 651 nm was employed. In Fig.33, the sketch of the set-up in use is illustrated. Laser light went through a polarizer and a PEM mounted in the way of the beam to convert the linearly polarized light into circularly polarized light. Then it was focused onto the sample surface by a lens. The surface was located at the diverging part of the beam with a diameter of 2 mm. The desorption was performed for approximately 10-15 min per step. Each step of the rotation covered a 2 mm-length of the substrate perimeter, which was approximately correspondent to 20° of the stage.
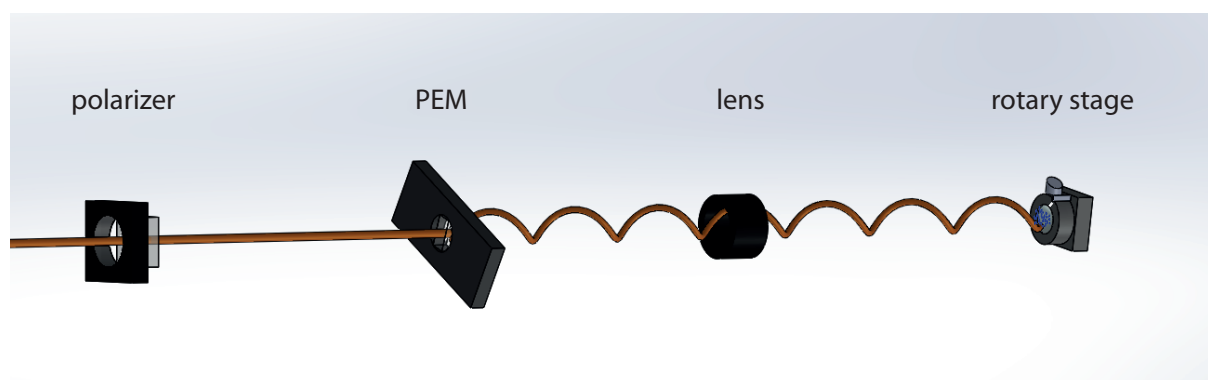
Figure 33- The preliminary set-up of enantiospecific desorption. A linearly polarized light goes through a polarizer and then a 45° rotated PEM, resulting in circularly polarized light which is focused afterward on the sample. The substrate is installed on the rotary stage.

▪ *Observing linear CD effects:*

After performing the desorption with one of the handedness of circularly polarized light, the remained mixture was dissolved into 3.5 ml MeOH (the achieved concentration was below the saturation level of CD spectrometer). The solution was analyzed with the CD spectrometer to observe the optical activity of the sample. The optical activity of the initial solution (mother sample) was also examined with the CD spectrometer to assure that the resulted CD effects were created throughout the desorption process.

3.3.2. Enantiospecific desorption by circularly polarized light and nonlinear CD spectroscopy

The first set of preliminary data was obtained within the first phase, however, due to obstacles caused by the laser system, sample preparation and analysis of the sample, the reproducibility of the results was not successful. In the new attempt, SHG-CD was performed in order to probe the sample before and after desorption with circularly polarized light. SHG-CD is a surface sensitive technique, which gives the possibility to follow changes at the surface, locally. This means that optical activity originated from the desorption by circularly polarized light can be followed at the spot of the desorption with this technique. The set-up which was utilized for this purpose is explained in the following.

3.3.3. Laser system:

The ultrafast light sources with pulse lengths in fs range, with low noise and adequate intensity, have been used for different studies in various fields such as physics, chemistry and biology. These sources are tuneable (UV to mid-IR) and pumped by amplified Ti: Sa lasers in cooperation with an optical parametric amplification (OPA). The $Ti:Al_2O_3$ or Ti: Sapphire solid-state laser is a tunable system which covers a range of 650 to 1000 nm (*118*). The combination of a collinear OPA and a difference frequency mixing extends the spectral range from near-IR to mid-IR, whereas a noncollinear OPA (NOPA) in combination with frequency doubling and sum frequency mixing provides the shortest pulses from UV to the near-IR. For this experiment, a Ti: Sa amplifier system (CPA 2001; Clark MXR) operated at 1 KHz repetition rate was used as a light source. It provided 1 mJ energy per pulse at 775 nm with 150 fs pulse duration. The long pulse width of the laser helps with both, stability and temporal resolution during the measurements. A two-stage NOPA was pumped by a fraction of 180 μJ. The pulse duration of the of NOPA output was compressed to below 50 fs which is close to the Fourier limit. The measurements were conducted with 600 and 650 nm with the energy of 0.6 to 2.5 μJ (*119*), respectively.

3.3.4. Sample preparation

Thin films of BINOL molecules (Aldrich, 99%) were fabricated by thermal evaporation and subsequent adsorption onto the substrates in a high-vacuum set-up (Fig.34). Optical borosilicate glass, commercially known as BK7, was employed as substrates. All the substrates were cleaned

by isopropanol and lint-free tissues to wipe off dust and other contaminations from the surface. The evaporation was performed in the home-designed vacuum chamber under pressure of 10^{-7} mbar and room temperature (*120*). The evaporator has three independent crucibles which are controlled, separately. Each of these crucibles can hold nearly 40 mg of BINOL. This amount corresponds to the thickness of approx. 1.5 µm which takes 20 min of evaporation. In order to estimate the film thickness, a pre-calibrated quartz microbalance (QMB) (INFICON SL-A1E40) was used.

The QMB function is based on the Sauerbrey equation where the deposited mass on the quartz crystal is considered as an extra mass added to the crystal. As a result, the frequency of the crystal will be changed. Therefore,

$$\frac{\Delta f}{f_0} = - \frac{\Delta m_f}{m_q} \tag{80}$$

Here f_0 stands for the initial frequency of the crystal, Δm_f denotes the extra mass added to the crystal and m_q is the initial mass of the crystal. On that account, the amount of deposited material can be estimated. By assuming a crystal volume of 357.8 A^3 per molecule, the thickness of 1.5 µm for the films was calculated.

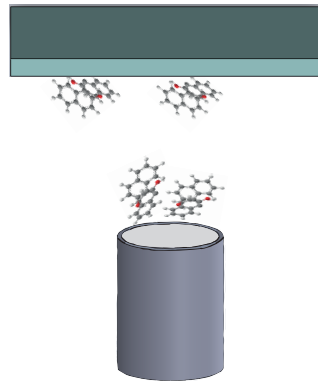Figure 34- The evaporation process. In order to prepare a film of BINOL, an evaporator was used.

3.3.5. Experimental set-up

As depicted in Fig.35, the linearly polarized output of the NOPA is guided through a polarizer and a QWP (B Halle) in order to create circularly polarized light. The QWP is automated by a motor (Berger Lahr) to swap between the two handednesses of circularly polarized light. Then,

the circularly polarized light is focused onto the sample by a fused silica lens (L_1) whose focal length is 100 mm, where SHG is generated. The angle between the incident beam and the surface normal is 70°. Afterward, both the SHG signal and fundamental laser light are collimated by another fused silica lens (L_2) with a focal length of 40 mm. The fundamental beam is separated from SHG, in the next step, by passing through a pair of Brewster prisms (P) and bandpass filter (Schott 2UG11, 1UG5). Finally, the SHG signal is focused onto the detector (Horiba MicroHR, LN.CCD Princeton Instruments) by a third fused silica lens (f = 100 mm). The used optical components are described in the following.
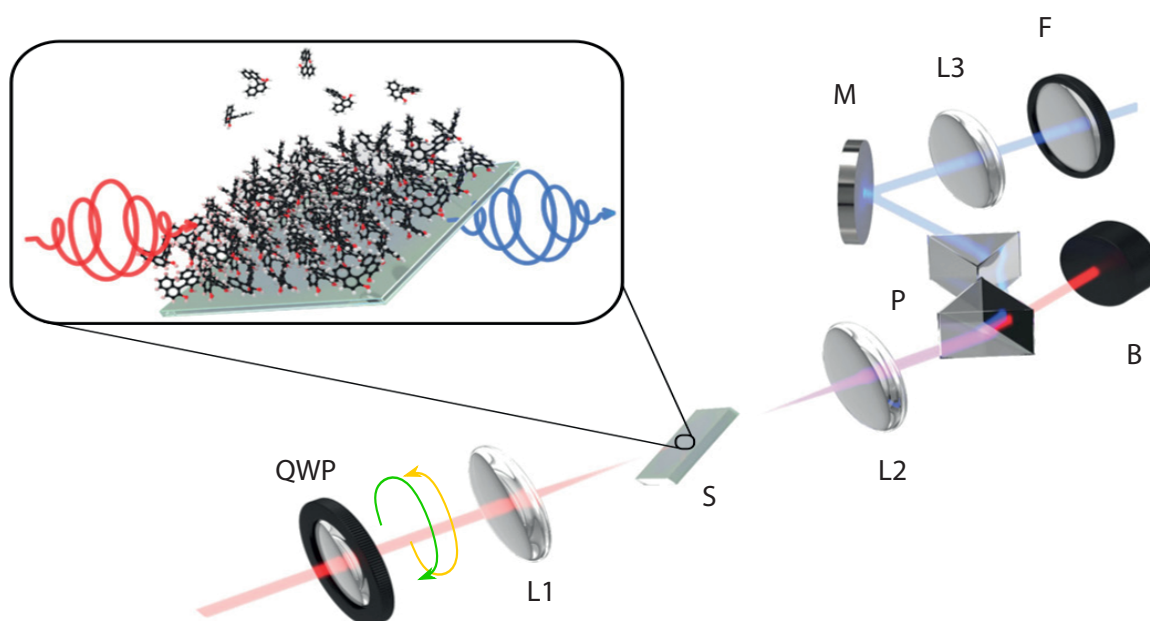
Figure 35- The enantiospecific desorption measurement set-up. Linearly polarized light from NOPA is altered by a QWP into the circularly polarized light. The laser beam is focused by a lens (L1) onto the sample and SHG response is collected.

- *Brewster prism and bandpass filter:*

A Brewster prism is an optical element used for transmitting p polarized light, perfectly. One of the applications of these prisms is to filter the output of OPA systems. These prisms can be used individually or in a combination to provide the desired reflection angle and therefore lateral shifts. The latter one can be controlled by altering the relative positions of the prisms (*121*). The bandpass filters are able to transmit a range of wavelengths and block any other wavelength which is not in the desired range.

▪ *Detector:*

A monochromator from Horiba (MicroHR) and liquid nitrogen cooled CCD (LN/CCD) from Princeton Instruments were used for this experiment as detectors. Horiba MicroHR is a spectrometer (scanning monochromator) with high-quality gratings covering a wide range of wavelengths from deep UV to mid-IR. Charge-coupled device (CCD) detectors are required for the experiments with poor signal intensity level (e.g. SHG signal) where multiple integrations have to be done.

3.3.6. Experimental procedure

The experiment is conducted in the three steps. First, measure SHG-CD at the spot '*x*' of the surface. To do so, the sample surface is exposed to left circularly polarized light, and the SHG signal is recorded. Then again, the sample surface is illuminated by right circularly polarized light, and the SHG signal is collected. Each SHG signal intensity is the averaged over 15-20 spectra. By applying Eq.59, the g-value of the surface at spot '*x*' is calculated. This value is the initial g-value of the spot; thus, it is called g_0. Second, the spot '*x*' at the surface is exposed to one of the handedness of circularly polarized light for different time durations. Third, SHG-CD is measured again at the spot '*x*' at the surface and analogous to the first step, the g-value is evaluated. The g-value corresponds to the specific desorption time is called g_i. The difference between g_0 and g_i is defined as Δg, which is the change in optical activity due to the desorption by circularly polarized light.

4. Results and discussion

4.1. Gas phase laser spectroscopy

The aim of this part of the thesis is to observe the vibrionic transitions of R-(+)-1-phenylethanol, which is a volatile molecule in the gas phase. In addition, the role of the vibrational modes on the g-value of enantiomers is investigated. The example of R-(+)-1-phenylethanol illustrates the potential of the presented approach in the study of volatile chiral products of the asymmetric catalysis.

The experiments were conducted in the set-up, which was explained in detail before in section 3.1. R-(+)-1-phenylethanol was injected into the vacuum via supersonic expansion, while the reference molecule phenol, which is an achiral but volatile molecule, was brought into the chamber via effusive beam. The reference molecule is used for a precise mass calibration as well as a g-value correction. The nozzle of the pulsed general valve, used for this experiment, had a diameter of 0.2 mm. Backpressure of 2.8 bar (argon) was used for the supersonic expansion. The measurements were performed under a working pressure of approx. $4 \cdot 10^{-6}$ mbar. In order to carry out (1+1) CD-REMPI-MS, the dye laser system (Coumarin 153, 1.6 g/l in Ethanol) in combination with a doubling frequency system was used to provide the range of 259-266 nm. This range makes possible to investigate the $\pi \longrightarrow \pi^*$ transition ($S_0 \longrightarrow S_1$) of the phenyl ring of R-(+)-1-phenylethanol.

1-phenylethanol was found to be an endogenous volatile compound in tea flowers (*122*), as well as cranberries, grapes, cocoa and so on (*123*). However, there are a number of approaches to synthesize this chiral molecule enantiomerically pure as reported by Yun et al. (*124*). Moreover, there exist a few reports about the intramolecular interaction, configuration and conformation of this chiral molecule (*125, 126*). The chemical structure of both enantiomers and their g-values are presented in Fig.36. The fragmentation pattern of this molecule was described in detail by Nibbereing et al. (*127*) and will be discussed later.
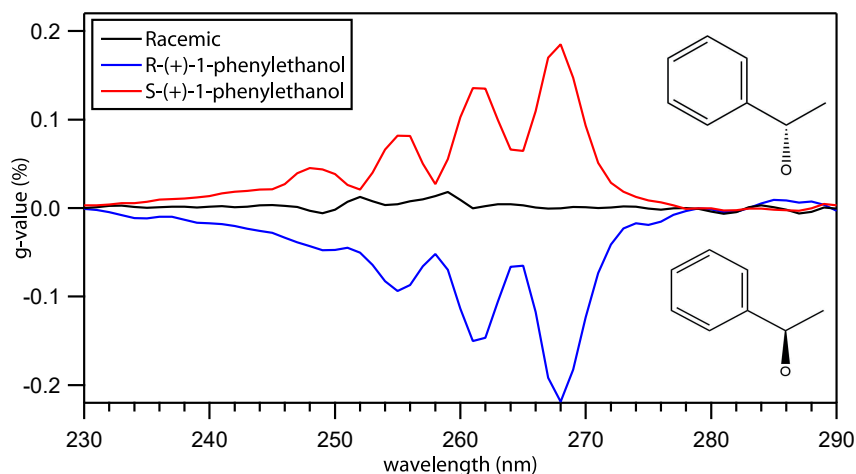
Figure 36- G-value of R-(+)-1-phenylethanol (blue), S-(+)-1-phenylethanol (red) and its racemic mixture (black) in ethanol, recorded by a CD spectrometer (JASCO J-815). The chemical structure of each enantiomer is depicted next to the corresponding spectrum.

In this section, the role of vibrational modes of (R)-(+)-1-phenylethanol (Sigma-Aldrich, enantiomeric excess > 494.0%) on the g-value is investigated, following the recent study of our group (publication B) (*13*). The results of R-(+)-1-phenylethanol are split into two main parts. The first part is the interpretation of the mass spectrum and the fragmentation pattern of this molecule. In the second part, the (1+1) CD-REMPI-MS measurements will be discussed.
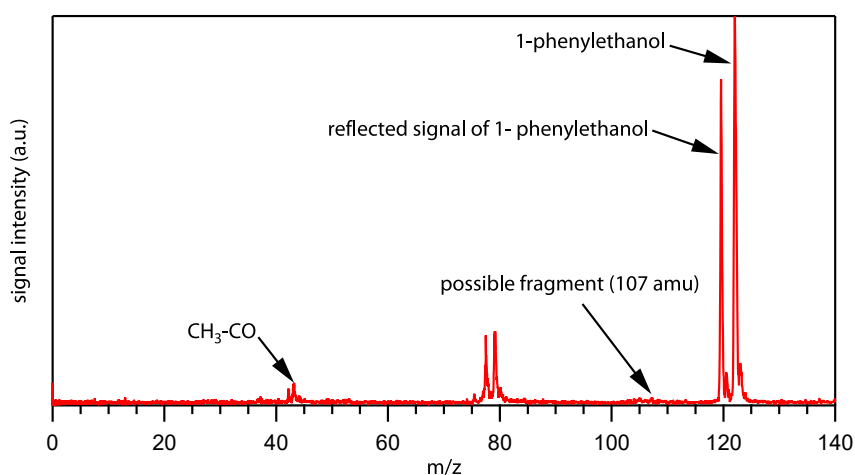

Figure 37- The mass spectrum of 1-phenylethanol. The twin peak method was used to record the mass spectrum. The fragment at 107 amu (g/mol) is not pronounced here.

R-(+)-1-phenylethanol with a molar mass of 122.167 g/mol shows the mass spectrum in Fig.37, where it is fragmented into 107 g/mol and 79 g/mol, mainly. These two masses are explained by the fragmentation mechanisms suggested in Fig.38a and Fig.38b, respectively. As reported by Nibbering et al. (*127*), these two fragmentations can be caused by losses of CH_3 and subsequently CO. The only discrepancy between literature and our mass spectrum is the intensity of the 107 g/mol fragment. This can be interpreted by the separation of both CH_3 and CO at the same time rather than in two steps. That results in a smaller abundance of the 107 g/mol fragment.
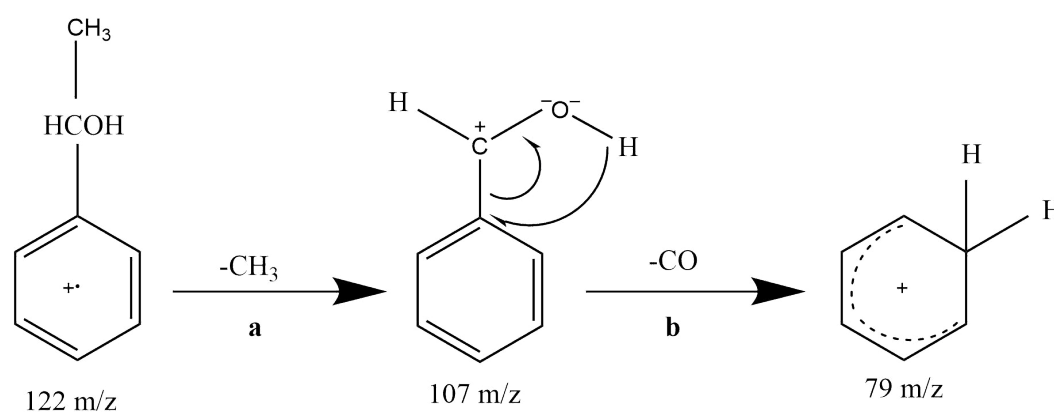

Figure 38- Possible fragmentation mechanisms for 1-phenylethanol.

After the observation of the mass spectrum of R-(+)-1-phenylethanol, the g-values for different vibrational modes between 37594 to 38610 cm^{-1}, corresponding to the range 259-266 nm, were investigated.

As the first step, a scan over the range of 259-266 nm was conducted and the ion signals in both, effusive and supersonic cooled molecular beams of R-(+)-1-phenylethanol, were recorded. Both scans are illustrated in Fig.39. The plots show the ion signals as a function of relative wavenumber (cm^{-1}). The latter one is scaled based on the 0_0^0-transition, meaning that the reported wavenumbers are relative to 0_0^0-transition. The cooled molecular beam yields the high resolved vibronic transitions of R-(+)-1-phenylethanol. On the contrary, the effusive beam spectrum exhibits a broad absorption band. The observation of well-resolved vibronic transitions in case of the supersonic jet illustrates one of its significant advantages (*48, 128, 129*). The difference between the cooled molecular and the effusive beams lies in the temperature of the molecules. In case of the cooled molecular beam, thanks to the supersonic expansion, the translational and

rotational (to some degrees) transitions of molecules are cooled. Therefore, molecules possess just vibrational transitions. With the help of literature (*125*), ten different vibrational modes around the 0_0^0-transition (within 1000 cm^{-1}) were assigned in the high resolved spectrum (these assignments will be discussed, later).

Moreover, one colour (1+1) CD-REMPI-MS was performed in combination with the twin peak technique, to calculate the g-values of these different vibronic transitions. This combination helped to improve the accuracy of the obtained data. It should be noted that g-values were calculated for those bands with non-negligible intensities. As reported previously by our group (*13*) and shown in Fig.40, the anisotropy factors varied up to forty times for different vibronic transitions (publication B).
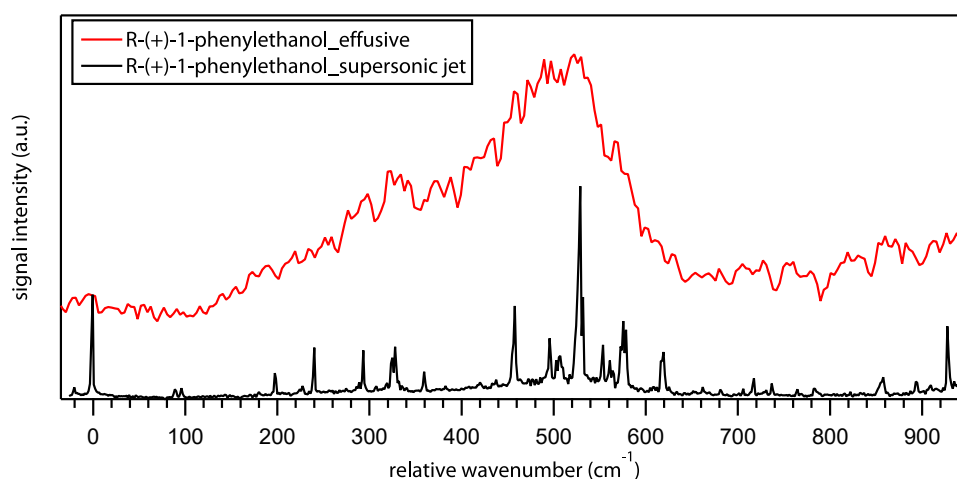
Figure 39- Scans (259-266 nm) in effusive and supersonic jet molecular beams on R-(+)-1-phenylethanol.

In addition, there are significant discrepancies between the calculated g-values in the effusive and cooled molecular beams for the same wavelength. This points out the role of rotational transitions and hot bands which exist at room temperature in case of the effusive beam. The rotational broadening and excitation of hot bands lead to the overlap of several vibrational modes. As a result, the calculated g-values for the effusive beam are the averaged values of the adjacent transitions. Thus, the absolute values are different compared to the g-value of the single vibronic transitions at the same wavelengths. Furthermore, each vibrational mode affects different molecules in a non-identical way. It depends on the molecular structure and alignment of electric and magnetic dipole transition moments. Considering Eq.36, if the angle between these two dipole moments spans from smaller to larger than 90°, the sign of g-values will be

flipped. One can assume that the influence of different vibrational modes results in a variation of this angle. Therefore, the g-values of different vibrational modes possess opposite sign in some cases. This assumption was proved by TD-DFT calculations. However, that cannot simply be extended to other chiral molecules due to the fact that all the calculations are structure dependent and are not analogous for all chiral molecules. In conclusion, the combination of theory and experiment demonstrated the role of vibrational modes on the g-values. Such information is valuable in basic molecular research, for example, molecular spectroscopy, molecular geometry and so on.
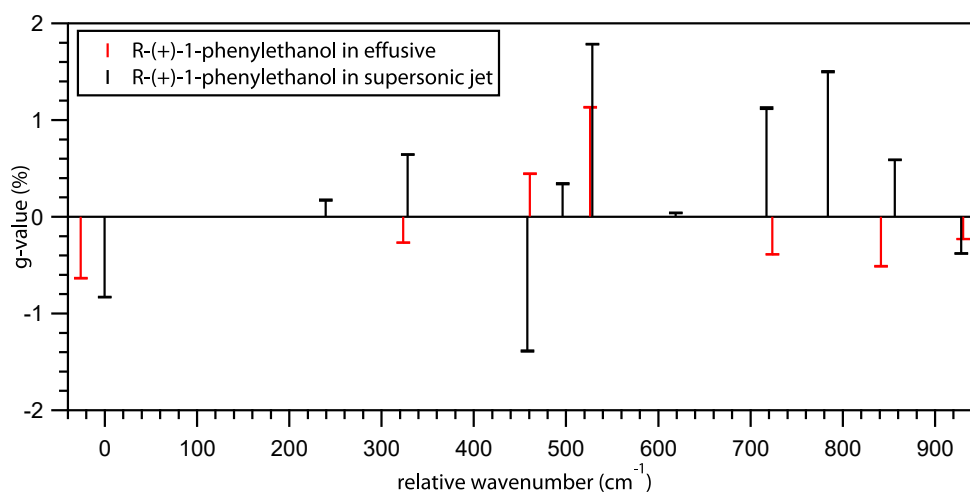
Figure 40- Calculated g-values for R-(+)-1-phenylethanol in effusive and supersonic jet molecular beams.

Although measurements done in the supersonic jet contain many details, the corresponding computational simulations were proved to be challenging as well. To assign vibrational modes to vibronic transitions obtained in a supersonic jet, one usually takes into account both position and intensity of the predicted bands and tries to find the pattern similarities to have the best match (*130, 131*). Nevertheless, the matching procedure may be not very accurate, due to the fact that both positions and intensities are slightly off compared to the experimental data. That is caused by the assumptions made for the calculations and also the inherent property of the models (*132*). In packed spectra, even the order of the energies of neighboring bands can be affected (*133-135*). The objective of the follow-up study (publication C) (*136*) was to assign vibrational modes to vibronic transitions with more confidence. Given the advantage of g-value and its additional information in case of chiral molecules, the assignments could be done more reliably. For that purpose, we collaborated with Prof. Fabrizio Santoro, who is a senior researcher

at the Institute of the chemistry of organometallic compounds (ICCOM) of the Italian national research council in Pisa, in order to perform the theoretical calculations.

For this study, the experimental data was acquired as it was explained above for the previous study. R-(+)-1-phenylethanol in the supersonic jet, was chosen again as an investigation system. The TD-DFT was performed for R-(+)-1-phenylethanol in the region within 1000 cm^{-1} around the 0_0^0-transition.
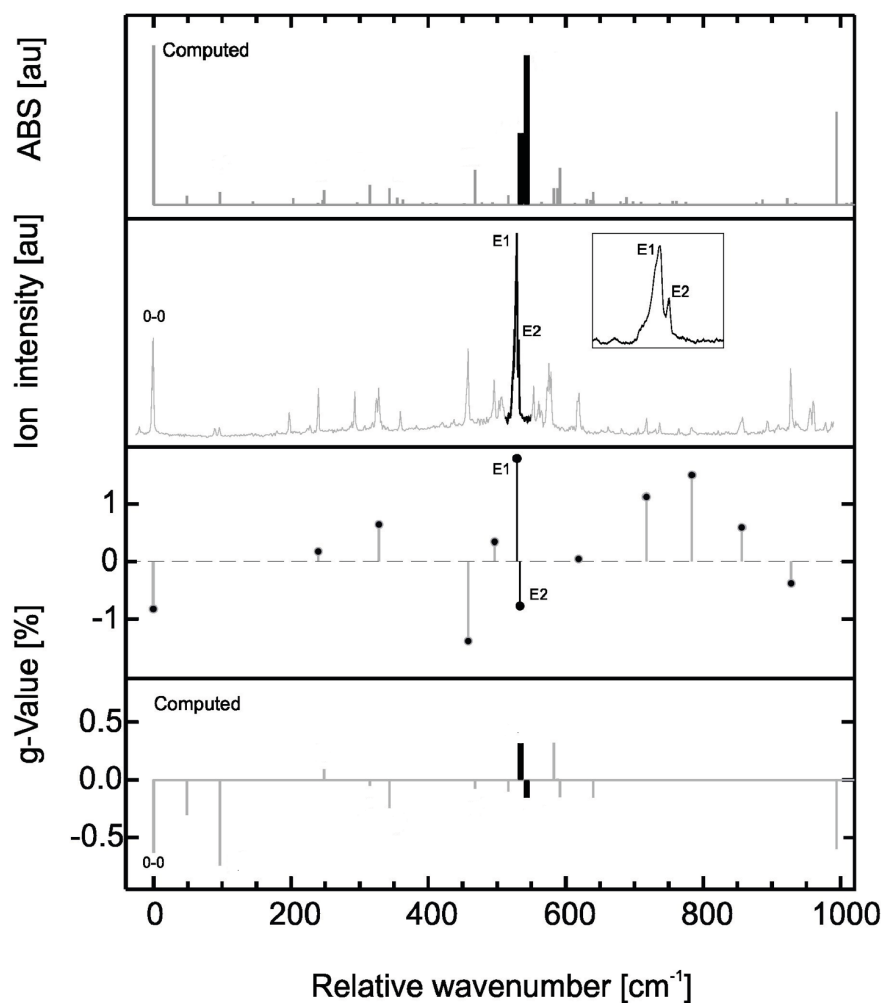
Figure 41- Experimental (central panels) and theoretical (top and bottom panels) spectra of the absorbance and g-value performed and calculated on R-(+)-1-phenylethanol in a supersonic jet. The figure is copied from reference (141).

The intensity, as well as the g-value, were calculated. The prerequisite for the calculation of g-values, namely the amplitude and direction of the electric and magnetic dipole transition moments, were already available and obtained from the calculations done for the position and

intensity of the vibronic bands. However, g-values of the transitions with intensities smaller than 5% of the most intense transition stick were not calculated. The reason behind it lies in the inherent inaccuracy of the predicted intensity and ECD, which leads to a large error for g-values. In Fig.41, all the calculated and experimental data are presented. Both, intensity and g-value plots are functions of relative wavenumber (cm^{-1}). The latter one is scaled based on the 0_0^0-transition, meaning that the reported wavenumbers are relative to the 0_0^0-transition. As it is illustrated in Fig.41, calculations show a nearly similar pattern as the experimental one. This includes a strong 0_0^0-transition, a set of weak bands around 250-350 cm^{-1}, a bunch of bands with the intense peak at 450-550 cm^{-1} (E_1 and E_2) and a band at 900-1000 cm^{-1}. The latter one shows the largest position discrepancy compared to experimental data, whereas, all the other predicted bands show a slight blue shift. Although the intensity and g-value of the bands are generally in good agreement with the experiment, there exist some discrepancies. Based on this calculation, the assignment done in the previous publication (publication B and reference (*13*)) can be revisited. The band at 994 cm^{-1} (927 cm^{-1} in the experimental data), was correctly assigned to a ring breathing mode, based on the new computations. The band at 248 cm^{-1} (242 cm^{-1} in the experimental data), was also correctly assigned to the torsion of the rotation of the CH_3 group. The band at 468 cm^{-1} (462 cm^{-1} in the experimental data) was previously assigned to a CH_3 bending mode. Although, in the new calculations, the intensity of the band as well as the sign of the g-value were predicted almost correctly, the magnitude of the g-value was drastically underestimated. Thus, it was suggested that a CH_3 bending mode, in this case, was coupled strongly with the C-C-O bending mode so that the g-value in the computed data yielded a smaller magnitude.

In addition to the comparison mentioned so far, there are more notable dissimilarities between experimental and predicted data. For instance, in case of the band at 330 cm^{-1}, both position and intensity of the band were reproduced by calculations, but the sign of the g-value for the predicted band is not matching with the experimental one. In the previous publication (publication B and reference (*13*)), this band was assigned to a ring deformation, while here the coupling with the H-C-OH torsion was also considered to have a contribution. This example exposes the limitations of assignments which are solely based on the intensity and the position of the bands. Also, it illustrates the importance of considering the g-value for the assignments. As a result of such dissimilarities, a high confident assignment was not possible. However, the difference in the sign of g-values could be explained from the theoretical perspective; the calculations may

predict a too strong coupling between the ring deformation and the H-C-OH torsion modes which ended in the wrong g-value sign in the computed one.

A more pronounced example for the importance of the consideration of the g-value for the assignment procedure is found for the computed transitions at 534.22 cm^{-1} (E_1) and 543.15 cm^{-1} (E_2). They are assigned to the fundamentals of an out-of-plane and an in-plane deformation of the ring modes, respectively. In this case, based on the absorption intensity and the position of the computed bands, they could be assigned to the experimental band at 528.92 cm^{-1} and its shoulder peak at 531.83 cm^{-1}, respectively. Nonetheless, that assignment cannot be very confident, due to the apparent discrepancy of their relative intensities between theory and experiment. The computed bands seem to be swapped because of inaccuracy on the computed frequencies. Possible reasons are the approximations in the level of electronic theory or the lack of proper anharmonic corrections. Despite that, a new set of experiments were performed to calculate the g-value for these bands. Interestingly, the results turned out to be in great agreement with the theory. Both, sign and relative amplitude of the experimental g-values were matching with the predicted computed values. On that account, it was determined that the order of predicted bands was correct; therefore, the transitions at 534.22 and 543.15 cm^{-1} were correctly assigned to the out-of-plane and the in-plane deformation of the ring, respectively. Regarding these new results, the reason behind the discrepancies between relative intensities of the bands cannot be justified by the errors on the frequencies, but rather inaccuracies on the wavefunctions which are responsible for the intensities. This study shows that g-values calculated from experimental results in addition to theoretical ones, make the assignment of vibrational modes to vibronic transitions more reliable.

■ *Conclusion:*

In this study mass spectra of 1-phenylethanol, cooled in a supersonic jet were shown, where the fragmentation pattern is well-matched with the available literature. In addition, a high vibrationally resolved spectrum was acquired via one colour (1+1) CD-REMPI-MS. The theoretical calculations helped to understand the configuration and structure of chiral molecules, more profoundly. It was demonstrated that the simultaneous comparison of computed and experimental data for both absorption intensity and g-value of various vibronic bands leads to the firm and robust assignment of these bands to vibrational modes. That reveals the high potential of the information obtained via CD-REMPI-MS and how it paves the way towards a

deeper understanding of molecular electronic levels in combination with the theoretical predictions.

The example of 1-phenylethanol also shows the capability of CD-REMPI-MS as an analytical tool for volatile products of the heterogeneous asymmetric catalysis. This information not only includes the chiroptical activity and enantiomeric excess of the products but in combination with theoretical models determines the absolute configuration of them.

4.2. Laser desorption of non-volatile chiral molecules

The goal of this section is to analyze non-volatile chiral molecules in the gas phase as isolated molecules. The investigation of these molecules had been restricted to analysis methods in solutions and under the influence of solvent molecules. After the invention of the laser, the idea of combining it with a mass spectrometer, in order to desorb and/or ionize non-volatile molecules in the gas phase, became the centre of attention of many researchers in the late 70s and early 80s (*14, 137-139*). Later on, this method was modified with the introduction of supersonic expansion and REMPI (*15, 41, 140, 141*). Performing CD-REMPI-MS in the gas phase on such molecules can open up new doors towards the study of their configuration. In addition, this approach can be applied to investigate non-volatile products of asymmetric catalysis.

In this thesis, the main goal is to facilitate the set-up explained previously together with the newly designed laser desorption source (see section 3.2.3). By achieving this goal, the current set-up is capable to perform CD-REMPI-MS on many chiral molecules regardless of their vapor pressures. First, a prototype set-up (section 3.2.1) was used for the preliminary investigations of laser desorption ionization, and the second step was the design of a new desorption source for the main set-up and integration of that into the main set-up.

For this purpose, 1,1′-Bi-2-naphthol or BINOL was chosen as a molecule of interest. BINOL has a mass of 286.32 g/mol. Its volatility is not sufficient enough to sublimate under room temperature conditions, therefore, it is a perfect choice for the first demonstration of the laser desorption technique. BINOL is one of the most well-known chiral molecules which has an axially chiral C_2 symmetry. The increased resistance to rotation around the 1,1′- bond raises the optical activity in BINOL enantiomers. Both enantiomers of BINOL are thermally stable. BINOL was found in 1873, however, it became representative of a chiral molecule in the early 1970s. Since then, there has been a great number of researches on BINOL and its derivatives in different research fields such as molecular recognition, metal mediated asymmetric catalysis, chiral material building, hydrogen bonding donor organocatalysts, asymmetric transformation (*142*), therefore, BINOL is a good choice to start with. It was reported that BINOL possesses two conformers, cisoid and transoid, with the dihedral angles (between two naphthalene rings) of less and greater than 90°, respectively. However, cisoid is the preferred conformation. In addition, CD spectra of these two conformations yield mirror images revealing that there is an inversion of the sign of the CD between them. Both conformation of BINOL, as well as their

dihedral angle configurations, are shown in Fig.42a. Two enantiomers of BINOL are depicted in Fig.42b. The common method to synthesize BINOL (racemic) is an oxidation reaction of 2-naphthol under room condition (in air) catalyzed by copper. In order to obtain enantiomerically pure BINOL, using (8S, 9R)-(-)-N-benzylcinchonidinium chloride as a chiral resolving agent is considered to be a simple and efficient method (*143*).
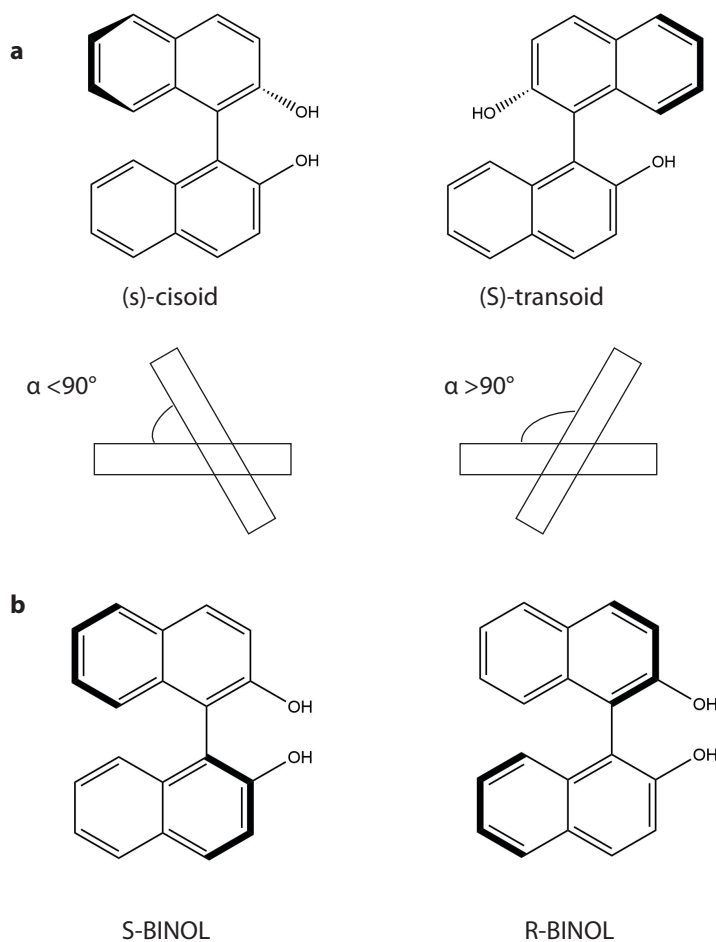
Figure 42- The chemical structure of BINOL. a) two conformers of BINOL and corresponding dihedral angles. b) two enantiomers of BINOL.

In Fig.43, the absorption spectra of BINOL in ethanol (0.0034 g/l) is shown as well as the g-value spectra. The resonance near 330 and 280 nm are resulted from the polarized transitions of 2-naphthol rings in the short-axis and off-axis (^1L_a and ^1L_b), respectively, while the significant absorption around 225 nm originates from the long-axis polarized transitions (^1B_b) of 2-naphthol rings (*144*). There also exist some theoretical works which tried to interpret the optical activity

of BINOL enantiomers and make suggestions for the contribution of different interactions and transitions in CD effects observed for BINOL (*30, 145, 146*). In this section, BINOL was used as a chiral molecule, to optimize laser desorption source.

Figure 43- The absorbance spectrum of BINOL in ethanol (upper panel) and g-value spectra of the racemic mixture (green), R-BINOL 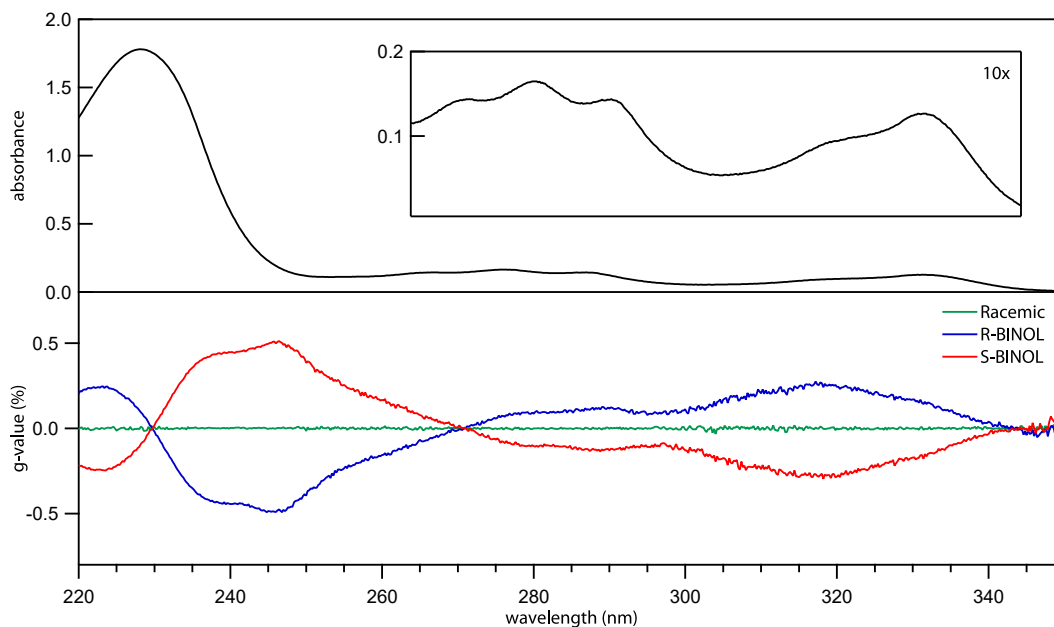(blue) and S-BINOL (red) recorded for the individual but the similar concentration of racemic, R-BINOL and S-BINOL in ethanol (bottom panel).

- ▪ *A prototype set-up of laser desorption*

The first set of trial experiments in the prototype set-up were performed on BINOL deposited on HOPG (Highly oriented pyrolytic graphite). The working pressure was low 10^{-6} mbar and the desorption and ionization lasers were operating at 607 nm (4.5 mJ) and 266 nm (0.42 mJ), respectively. Desorption was observed and the parent peak of BINOL was detected as can be seen in the mass spectrum in Fig.44. However, the signal intensity was poor and further optimizations of the set-up were needed.

The other long-term goal of laser desorption was to desorb molecules by circularly polarized light. By considering the fact that for the laser desorption by circularly polarized light, it is essential to suppress the influence of the foreign molecules in the desorption process, new sample preparation was developed. Accordingly, a new tip was designed for the sample rod, which held the pure sample powder (see section 3.2.1). The rest of the experimental conditions were kept

analogous to the previous studies. Interestingly, the signal intensity was improved by 10 orders of magnitude. Consequently, the results presented in Fig.45 indicates that the desorption can be performed not only without the assistance of extra molecules (like the case of HOPG) but also can result in a larger signal.
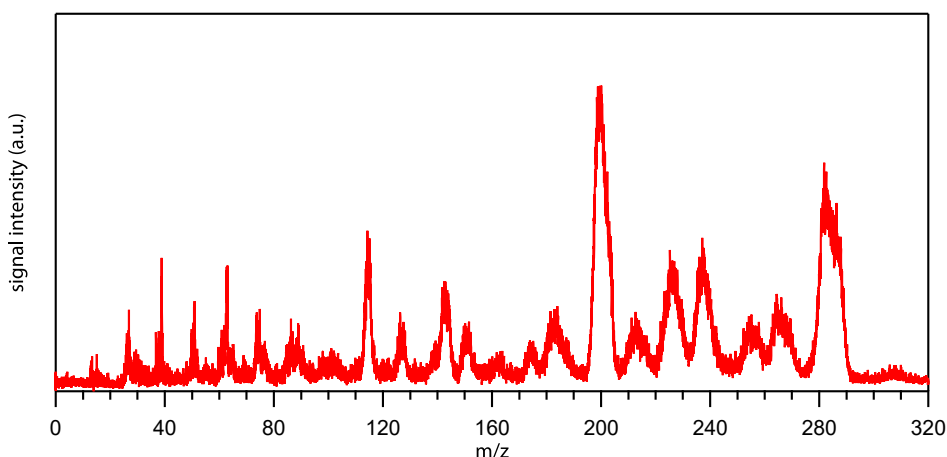
Figure 44- Mass spectrum of BINOL deposited on the HOPG. Recorded in the prototype set-up.
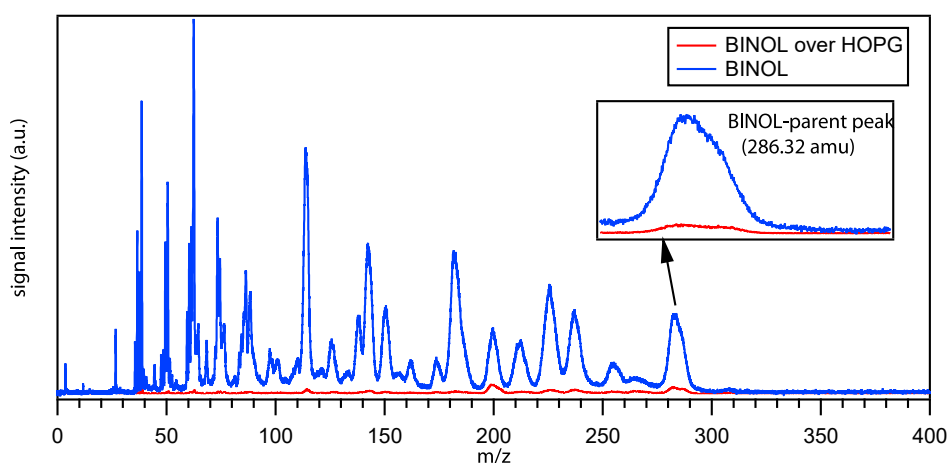
Figure 45- Compared mass spectra of two different sample preparations for BINOL. BINOL over HOPG (red) and pure BINOL (blue). The increment in the ion yield is more than 10 orders of magnitude.

To assure that such an intense signal is originated from the desorption process, itself, rather than the residual gas (background), the latter one was solely analyzed by the ionization laser. As shown in Fig.46, no residual BINOL was observed in the gas phase after overnight pumping of

the chamber (before carrying out desorption). Therefore, it can be concluded that the intense signal observed for BINOL after the desorption is a result of laser desorption.
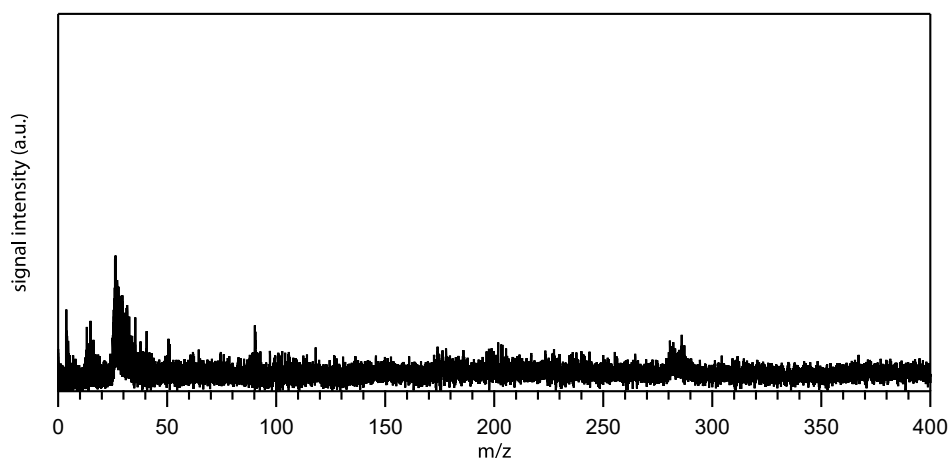
Figure 46- Mass spectrum of the residual gas (vacuum) after overnight pumping and without running laser desorption.

Furthermore, the stability of the signal was checked over a period of 190 minutes as plotted in Fig.47. The signal reached a plateau at the end, which is approx. half of the initial amplitude. Simultaneously, the energy of both lasers was also tracked within this measurement. It could be shown that the energy of the desorption laser increased by nearly 20% of the initial energy, whilst the energy of ionization laser dropped to 57% of its initial value. On that account, the fluctuations of the ionization laser seem to have substantial effects on the signal stability.
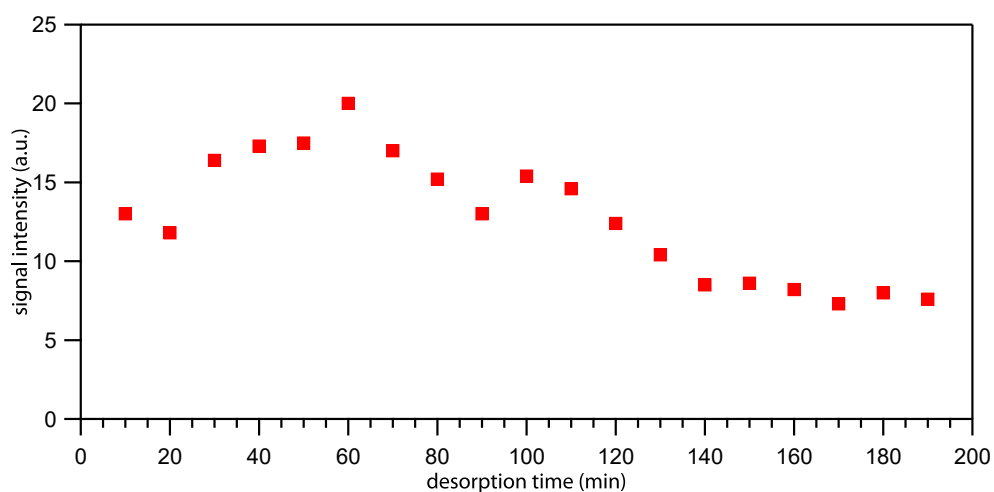
Figure 47- Signal stability as a function of desorption time.

In order to have efficient desorption of intact and neutral molecules, the wavelength of the desorption laser is one of the factors which plays a non-negligible role. Schlag et al. (*147*) claimed that according to their results, for resonant laser desorption, the dominant mechanism is the quantum mechanical one. Whereas, for non-resonant laser desorption, substrate absorption with a subsequent fast thermal laser heating seems to play a key role. Moreover, they concluded that the resonant laser desorption leads to intact neutral desorbing molecules. In another study reported by Saigusa et al. (*112*), they showed the dependency of the desorption efficiency on the wavelengths, where nearly no desorption was observed for the wavelengths at which the studied molecule was transparent (no TPA).

To answer the question what mechanism is dominant here and to desorb neutral molecules, the range of 600-620 nm was chosen for the wavelength scan for the desorption laser. This range was in accordance with the absorbance spectrum of BINOL. The scan was performed on BINOL in 1 nm steps. The data acquisition was random, meaning that, the wavelengths in the range were picked randomly and not in the sequence. As illustrated in Fig.48, the parent signal apparently follows the changes in the desorption laser energy. Although, the maximum laser energy and the most intense ion signal are not overlapping. The laser maximum performance appears at 609 nm, whereas, the most intense signal shows up at 607 nm.
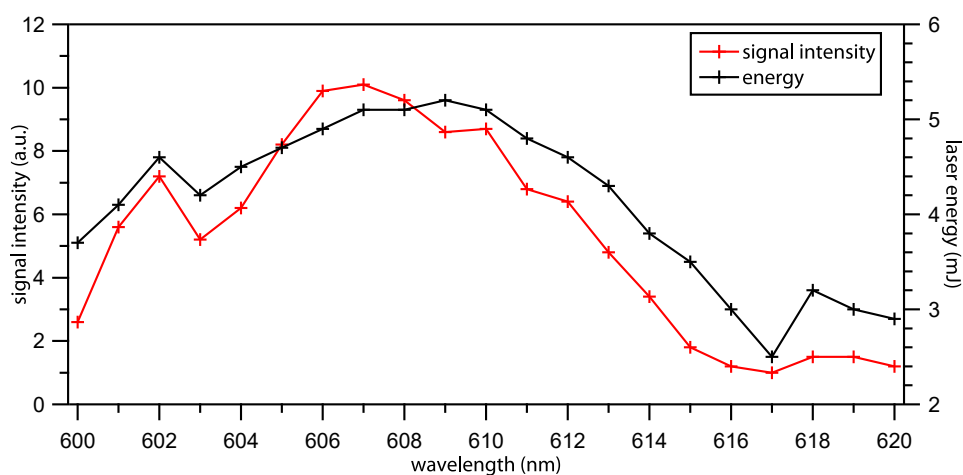

Figure 48- Desorption laser wavelength scan over 600-620 nm.

In another wavelength scan over a smaller range (604-611.5 nm), where the energy was almost constant, the signal shows different behaviour and do not follow the same trend as the desorption laser energy, as shown in Fig.49. That indicates that the signal intensity cannot solely depend on

the energy of the desorption laser and is also dependent on the wavelength. These set of data was also recorded in a random manner and was reproduced three times for each wavelength (the wavelengths in the range were picked randomly and not in the sequence). Therefore, the observed maxima cannot be explained by a decreasing trend in the signals, as seen in the signal stability study (Fig.47) or noise, but indeed depends on the wavelength. The data suggest that the desorption cannot be only dependent on the thermal mechanism, but the quantum mechanical processes do also play a role. To realize the contribution of both mechanisms, more studies and experiments need to be carried out.
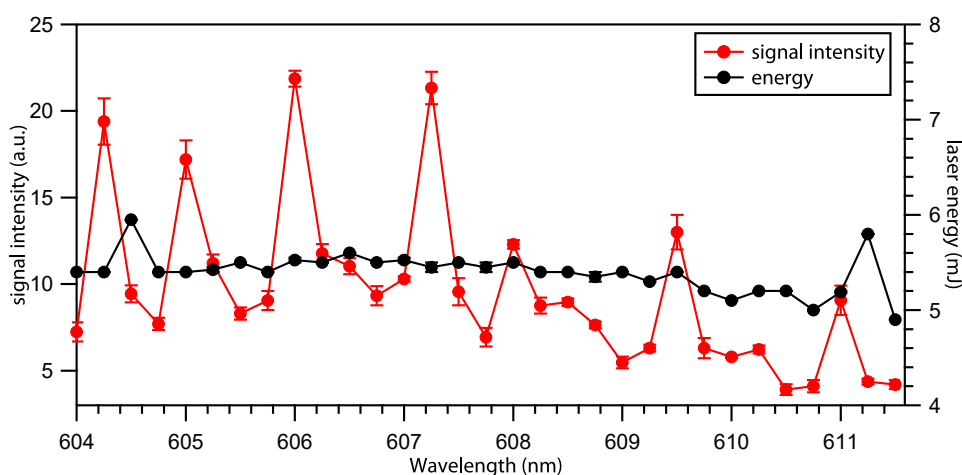
Figure 49- Ion signal intensity as a function of the desorption laser wavelength. Data acquisition for each wavelength was repeated three times

- *A new desorption source for the main set-up*

In the next step, a new desorption source was designed for the main set-up. Therefore, the experience with the prototype set-up gained in the previous studies could be used. However, many challenges remain, such as integrating a new part into the main set-up and the optimization of the setting, e.g. synchronizing two different dye laser systems with 20 and 30 Hz repetition rates. The same desorption and ionization wavelengths as in the previous studies with the prototype set-up were used here.

The first set of data obtained by the first version of the source was not promising as illustrated in Fig.50, because of the poor intensity of the BINOL signal. Many modifications were done in order to improve the signal, including the sample preparation, reducing the distance between the

molecular axis and the sample surface, enlarging outlet diameter of the source, reducing the spatial distance between desorption and ionization points, changing the wavelength of the desorption laser, and so on. A more detailed description of the modifications is given in section 3.2.4. By that, the signal intensity altered significantly.
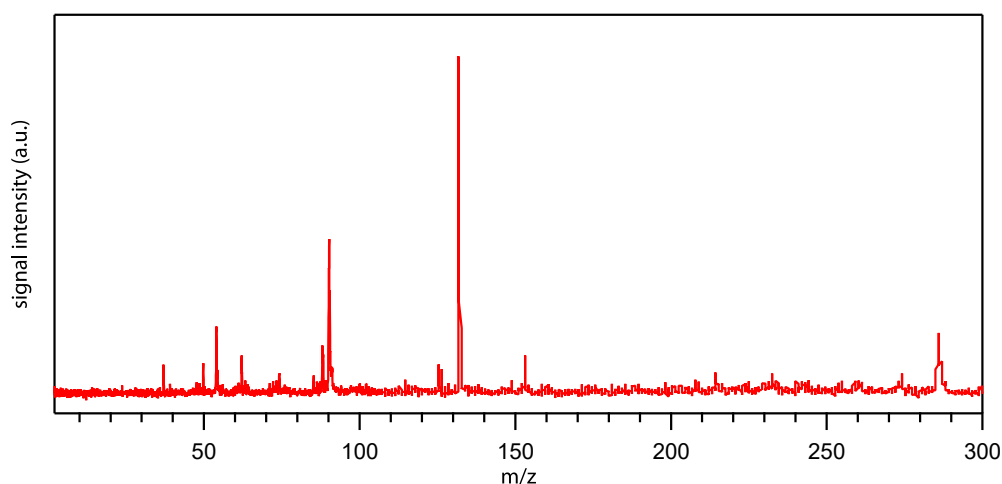
Figure 50- Mass spectrum of BINOL in the first version of the desorption source,
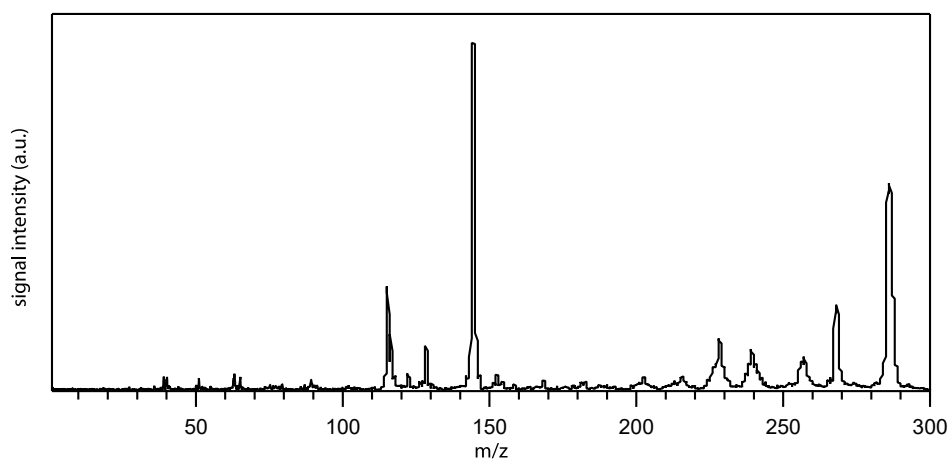
Figure 51- Mass spectrum of BINOL in the new design of the desorption source and after some modifications.

Finally, the mass spectrum of BINOL was successfully recorded (Fig.51) after implementing the new version of the desorption source and optimizing the main set-up. The generated fragmentation pattern for BINOL has not been studied to the best of our knowledge. To interpret the fragmentation pattern observed here, some explanation and suggestions are given in the following.
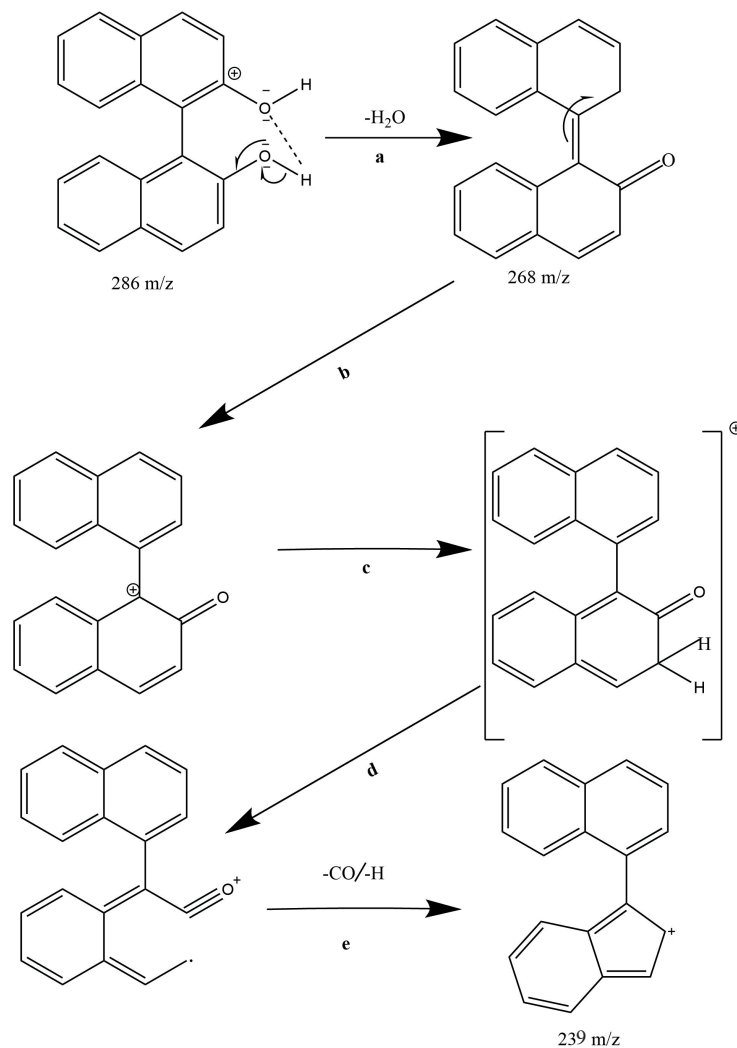
Figure 52- The proposed fragmentation mechanism for BINOL.

The parent signal of BINOL appeared at 286.32 g/mol. The reference molecule that enables a precise mass calibration, was 1-phenylethanol. It has a mass of 122.16 g/mol and was seeded via the gas inlet of the supersonic jet. Next to the mother peak of BINOL, which has the largest mass, a set of peaks close to each other are visible. The signal at 268 g/mol seems to correspond to a loss of 18 g/mol. That can be explained by the loss of $-H_2O$, as depicted in the sketch a in Fig.52. The next signal possesses a mass of 257 g/mol, suggesting that BINOL lost 29 g/mol. This fragment might be a result of losing -CO and subsequently -H, as indicated in the sketch of Fig.53. The signal with a mass of 239 g/mol, appears to have lost $-OH_2$, -CO and -H. Consequently, the fragmentation mechanism depicted in the sketches a-e in Fig.52 can be proposed.
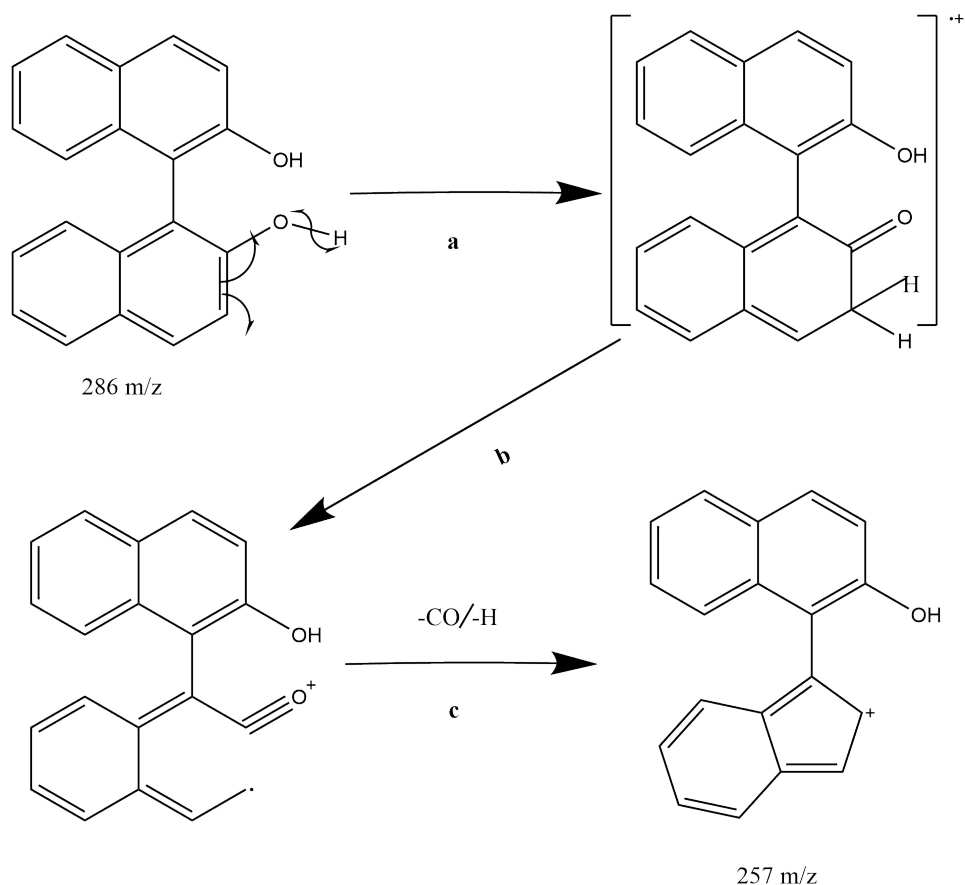
Figure 53- The proposed fragmentation mechanism for BINOL.

The most intense fragment is located at the mass of 144 g/mol whose mass is equal to the mass of 2-naphthol. According to the measurements, this peak was created within the desorption process which will be discussed later. The two other fragments that are close to 2-naphthol presumably were derived from 2-naphthol by loss of -OH and -CO/-H, with masses of 127 g/mol and 115 g/mol, respectively. Thus, the same procedure as the other fragments can be applied for them. It should be noted here that all the suggested interpretations for the fragments were only based on the mass spectra; therefore, for further and complete insight into the mechanism, more studies are required which is out of the scope of this thesis.

As shortly discussed before, the fragment with the mass of 2-naphthol was dependent on the desorption laser energy so that by passing a threshold energy, its intensity increased drastically. The relative increment of this signal was not scaling with the relative value of the parent signal. Additionally, the behaviour of the former one was independent of the supersonic jet so that without the pulsed general valve in use, the ion signal could be observed. That was not the case for desorbed BINOL and 1-phenylethanol in the supersonic jet. The subtracted spectrum from

spectra with and without enabled general valve is shown in Fig.54. The signal of mass 144 has a negative value. The negative value indicates that this fragment was in the residual gas of the chamber and independent of the general valve.
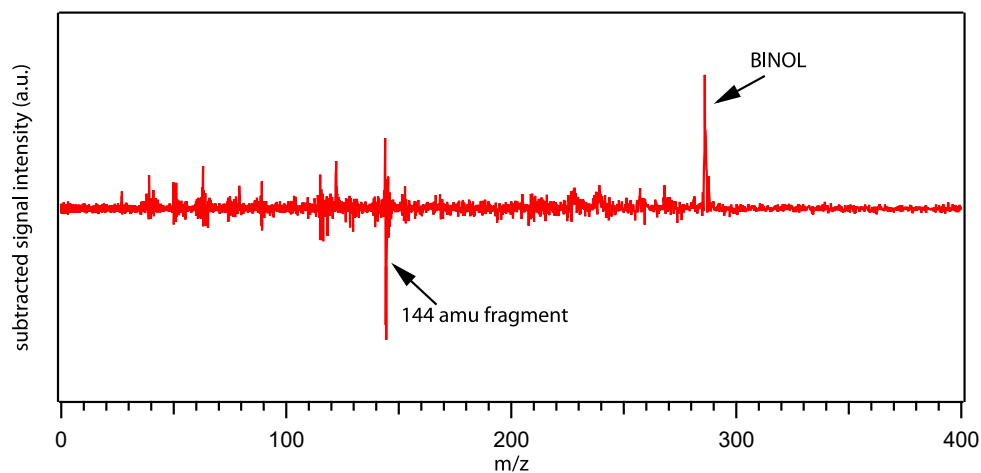
Figure 54- The subtracted mass spectrum of BINOL with the pulsed general valve activated and without it.

The brownish spots on the sample, caused by the desorption laser are shown in Fig.55. This indicates that some of the molecules were decomposed throughout the desorption process. Hence, breaking the molecules into two 2-naphthols is not improbable.

Figure 55- Desorbed spots on the sample surface.

Although the laser desorption was accomplished, the signal intensity was not stable. To improve the signal stability a stepper motor, which moves the sample underneath the beam of the desorption laser, was employed. The systematic motion with the least fluctuation of the signal

was the objective of the implementation of the motor. An ATP software programmed by the factory (Thorlabs) was used in order to control the motor. The program allows controlling the velocity (mm/s) as well as travel distance which is required to scan throughout the surface of the sample.
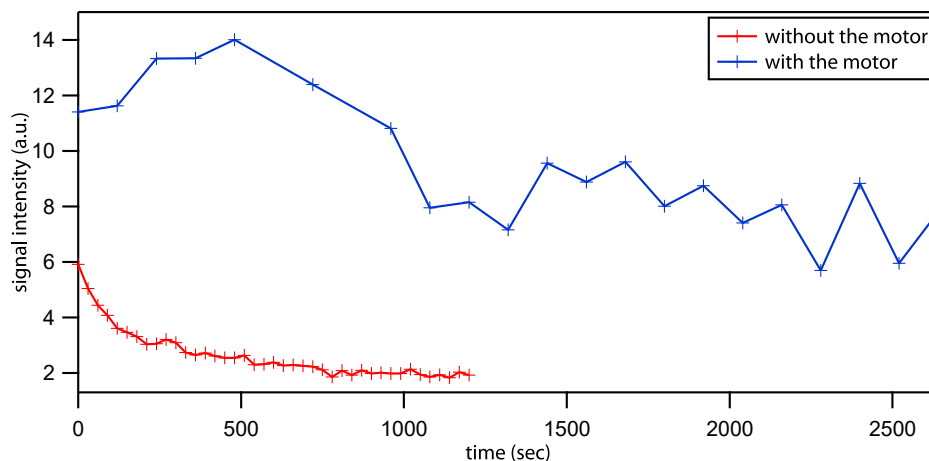
Figure 56- Comparison of the signal intensity between the automated and the fixed sample rod.
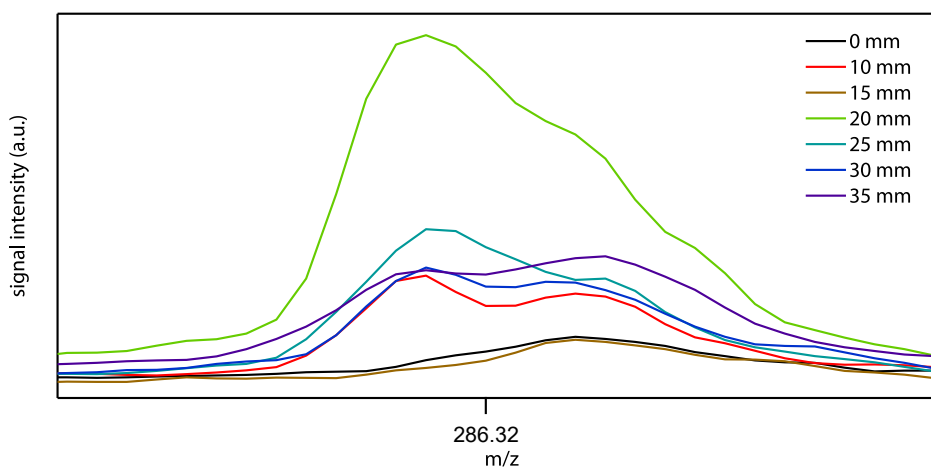
Figure 57- A scan of the sample surface with the moving rod, connected to the motor. The distance of 35 mm on the surface was investigated.

The signal intensity was increased as well as the stability, as can be seen from the plots in Fig.56. However, fluctuation in the signal was still observed. The origin of the signal fluctuations could be the fluctuations in the intensity of the desorption and/or ionization lasers, inhomogeneous sample preparation and the movement of the motor. The latter one, itself, makes a slight

fluctuation in the vacuum and working pressure, resulting in the signal fluctuation. The surface preparation quality can be probed by acquiring data at different positions on the surface, as indicated in Fig.57. The signal intensity was distinctly differed at different positions on the surface, suggesting that surface preparation is partly responsible for the unstable signals.

▪ *Conclusion:*

A newly designed laser desorption source was successfully implemented into the existing set-up. It enables the study of the desorption mechanism and the investigation of non-volatile molecules in the gas phase. For the first time, a REMPI-MS of BINOL in the gas phase was recorded. However, more modifications are required to improve signal stability. The studies in the prototype set-up revealed that the observed laser desorption is not a simple thermal desorption process, but quantum mechanical mechanisms may take place as well. The experiments indicated that many parameters affect the ion signal of the desorbed molecules, such as desorption and ionization laser energies, temporal and spatial synchronization between the pulsed general valve and the lasers, the distance between molecular beam axis and sample surface and the distance between the desorption and ionization point. All those factors contribute to the final ion signal of the desorbed molecules. Finally, CD-REMPI-MS studies on the chiral molecules in the gas phase are now possible with the present set-up. This opens the doors to investigate biologically relevant large chiral molecules, which are not volatile enough to be seeded via the effusive beam or the supersonic jet inlets. In addition, investigation of non-volatile products of the asymmetric catalysis is now possible with the modified set-up.

4.3. Enantiospecific desorption by circularly polarized light

As discussed in section 3.3, the enantiospecific desorption of chiral molecules by circularly polarized light became an interesting objective, because of the utility of this method in various research fields. Generally speaking, purification or enrichment methods of enantiomeric mixtures became popular, over the last decades. The enantiospecific desorption was proven by Horvath and Gellman. They reported that enantiospecific thermal desorption (by heating) of chiral molecules adsorbed on a chiral surface is plausible (*77, 148*). The potential application for such methods lies in the pharmaceutical industry where more than 50% of the products are made of chiral active ingredients. On that account, purifying enantiomeric mixtures has high importance in this industry in order to reduce or even remove the inactive or harmful enantiomer from the mixture (*1*). Developing practical and economical enatio-enrichment methods (*149-152*) as well as an increasing interest to analyze chiral molecules in the gas phase, especially non-volatile molecules (*13, 16, 40, 44, 56, 136, 153, 154*), led to merge both goals into one and propose a new method. It is proposed to remove and bring one of the enantiomers of the mixtures into the gas phase via enantiospecific desorption by circularly polarized light.

The objective here is to show that one can take advantage of the specific response of one enantiomer to the different handedness of circularly polarized light and try to excite one of the enantiomers more than the other one in order to be desorbed. The most promising and simplest system to start with is a racemic mixture due to the fact that it shows negligible optical activity. Thus, tracking the changes of the optical activity of racemic mixtures, which are exposed to circularly polarized light for desorption, can give us the answer to the question, "if enantiospecific desorption by circularly polarized light is plausible". Therefore, a racemic mixture of BINOL was chosen as a first system, which is a 50:50 mixture of two enantiomers. The experimental protocol was conducted in three steps. First, measure the g-value of the sample before desorption. Second, perform laser desorption with one of the handedness of circularly polarized light. Third, probe the g-value of the sample after desorption. In the following two approaches, which have been taken throughout this thesis to show the proof of principle of the enantiospecific desorption by circularly polarized light, are explained.

In the first attempts, the linear CD effects of the racemic mixture were probed. A solution of the racemic mixture was dissolved into methanol and brought onto the surface by drop coating (see section 3.3.1). Two identical samples were prepared for each try. The one, which is so-called

'mother sample', was kept as a reference for the initial optical activity of the prepared samples. Then, the set-up in Fig.33 was employed to desorb molecules from the surface. The dye laser system with nanosecond pulses and 3.6 mJ/m^2 fluence at 670 nm were used for desorption. A PEM converted the linearly polarized light to the circularly polarized light. A rotary stage was used in order to scan the surface by taking 20° rotation per step. The exposure at each step was set to 10-15 minutes. After the desorption procedure was completed, the sample was dissolved into methanol again (for more detail, see section 3.3.1). Then, the optical activity of the desorbed and mother samples was probed by a CD spectrometer (Jasco J-815), as it is presented in Fig.58. The absorption and g-value spectra for the mother sample, enantiopure R-BINOL and four desorbed samples are shown in this figure.
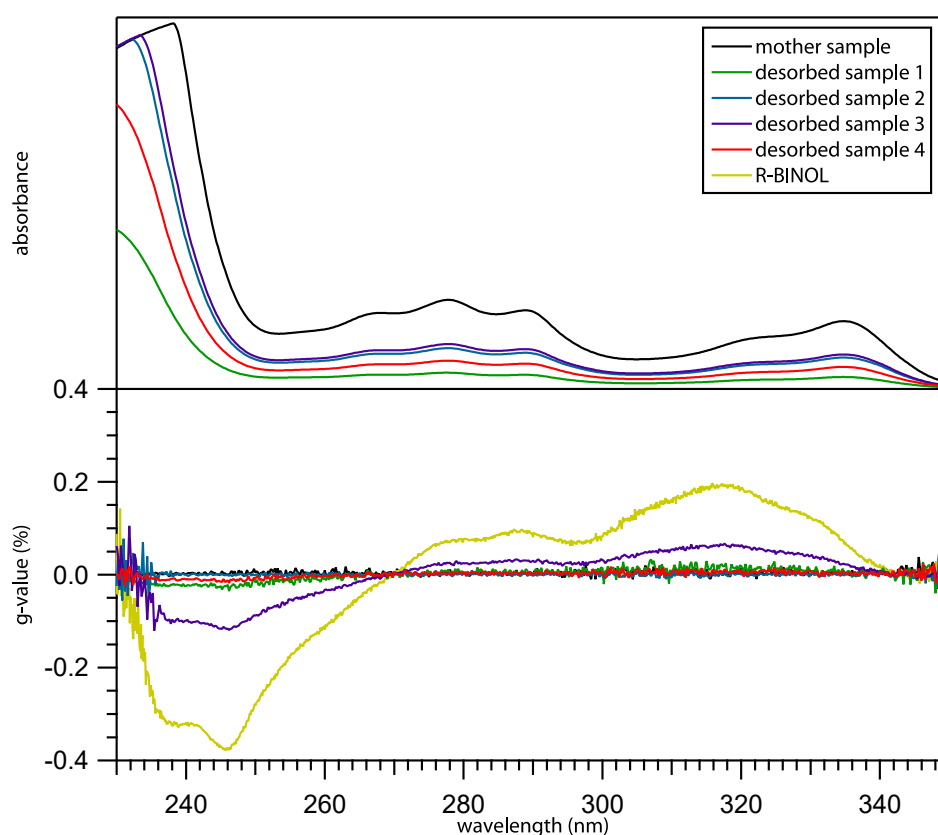
Figure 58- Absorbance (top) and g-value (bottom) of racemic mixtures of BINOL, before (mother sample) and after the desorption by one handedness of circularly polarized light. For comparison, a g-value spectrum of R-BINOL is included in the bottom panel.

As expected, the racemic mixture shows a zero g-value, as seen from the mother sample. Interestingly, the samples which were exposed to the similar handedness of circularly polarized light showed analogous changes in the g-value spectra. They yielded a similar behaviour as R-

BINOL; that means, throughout the desorption process S-BINOL was excited by the handedness of the circularly polarized light more than R-BINOL, resulting in an enantiomeric enrichment towards R-BINOL. Although the changes are not equal in magnitude, they have the very same fundamental origin. These discrepancies might be caused by irreproducibility in sample preparation, scanning of the sample surface, dissolving procedure and laser fluctuation. However, they all pointed out the fact that enantiospecific desorption by applying circularly polarized light is possible.

The obtained results here were not reproduced, because of inconsistencies in sample preparations, desorption and dissolving which strongly affect the reproducibility of this approach. Therefore, new preparation and probing techniques were considered (Patent A and publication D). The measurements of this section were performed in collaboration with Katrin Oberhofer, Dr. Hristo Iglev and Prof. Reinhard Kienberger from the chair of Laser and X-Ray Physics at Technical University of Munich.

To prepare the samples, the racemic mixture of BINOL was evaporated onto the BK7 (achiral) substrate and a deposited film with the thickness of 1.5 μm was achieved, as explained in more detail in the section 3.3.4. The importance of an achiral substrate is to exclude the possible role of the substrate in the enantiospecific desorption process.

Instead of observing the linear optical activity of the sample, a nonlinear CD effect was chosen to be probed before and after the desorption by SHG-CD. SHG was demonstrated to be a very versatile surface sensitive probe, which is based on the nonlinear interaction between light and matter (*155-157*). This is not the first time that SHG is used to probe the changes made by laser excitation on the surface. Hicks et al. used this technique to follow the temperature changes on an Ag (110) surface (*158*) or Shen and his co-workers showed changes of the CO coverage on a Ni (111) surface caused by laser-induced thermal desorption with the help of SHG (*90*). On the other hand, combining SHG with CD to probe the chirality of the surface was proven previously by Byers et al. (*159*). They showed that even small CD effects are recognizable with SHG-CD, thanks to the fundamental origin of the technique (*144*). Interestingly, the weak CD effect in the conventional linear method is drastically enhanced for SHG-CD, by several orders of magnitude on resonance (*29, 160, 161*). Hence, by considering the small chiroptical response expected from the prepared thin film, SHG-CD appeared to be a proper technique to track the changes of the g-value of the sample surface after the desorption by circularly polarized light. The other advantage

of performing SHG for this study is that all three steps of the experiment are done at one spot of the surface. As a result, the achieved g-value directly corresponds to the desorption spot.

The prepared sample was exposed to the circularly polarized sub-50 fs laser pulses with central wavelengths of 600 and 650 nm (0.6-2.5 µJ), generated from a NOPA (see section 3.3.3). The wavelengths were chosen for two-photon absorption of BINOL in order to desorb an intact and neutral molecule (*112*) and also to magnify the CD effects (*58*). The laser influence was kept below the photo-damage threshold of BINOL as reported in the literature (*162*). The femtosecond laser, which was employed here, has an advantage of short pulses. Therefore, the thermal desorption, which conceptually needs more time and happens at a slower rate compared to a quantum mechanical one, could be partly suppressed (*76*).

The set-up presented in Fig.35 was used to conduct the experiments under room temperature conditions. The optical activity of the sample was probed by irritating the surface to both left and right circularly polarized light (LCP and RCP, respectively). Thus, the obtained initial g-value (g_0) is calculated by Eq.59:

$$g = 2 \, \frac{I_{LCP}^{SHG} - I_{RCP}^{SHG}}{I_{LCP}^{SHG} + I_{RCP}^{SHG}}$$

Although no optical activity for the racemic mixture was expected, the observed values deviated from zero in reality. That can be a result of an inhomogeneous surface and a local deviation of the overall racemic mixture at the investigated spots. To compensate this, a relative value $\Delta g = g_i - g_0$ was defined, which will be explained later.

It should be noted that the sample was located in the diverging beam behind the focal point of the lens to prevent any contribution from the substrate to the SHG signal, as proved in Fig.59. By that, a self-focusing and the generation of white light in the substrate were also avoided.

Subsequently, laser desorption by circularly polarized light was performed on the BINOL films, with different desorption times (t_d) of 5, 10, 15, 20, 30, 60 min and so on. Both LCP and RCP lights were used for the desorption. Additionally, laser desorption with linear polarized light at 670 nm was also performed on the racemic sample for comparison and completeness.
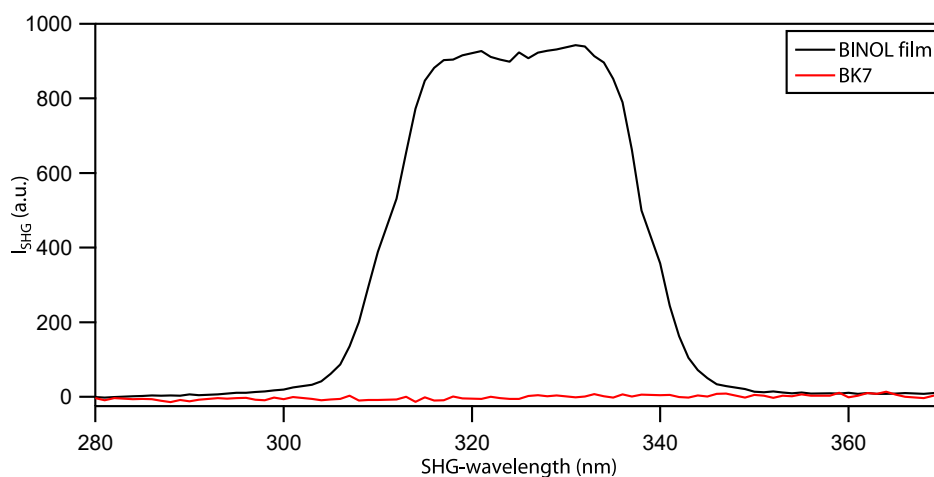
Figure 59- The SHG signal of the bare BK7 substrate and of the substrate coated with a thin film of a racemic mixture of BINOL.
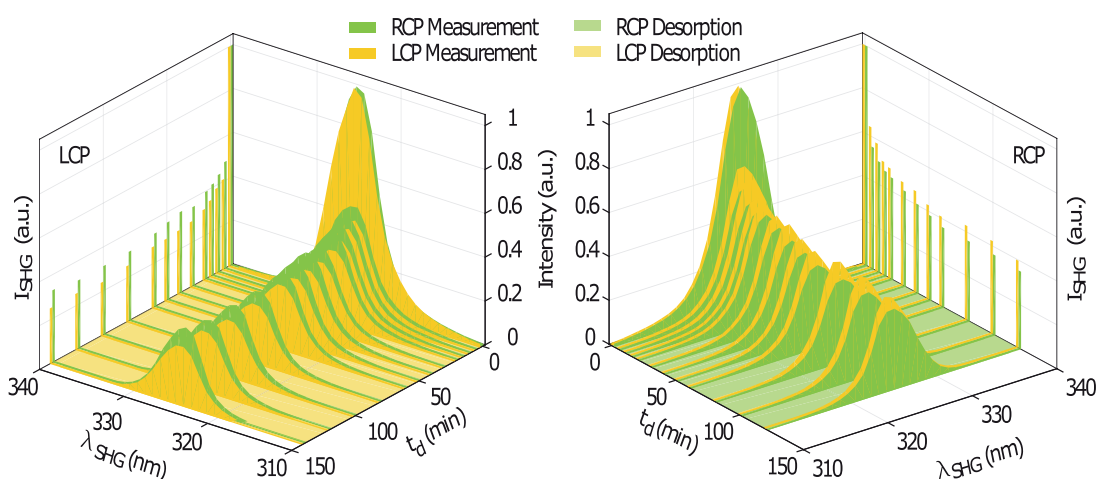
Figure 60- The protocol of the performed experiments. First, the initial g-value of the surface via SHG-CD was probed by LCP (the dark yellow curves in the plots) and RCP (the dark green curves in the plots) light. Then, the desorption was done by both LCP (bright yellow shadow areas in the plots in the left-hand side graph) and RCP (bright green shadow areas in the plots in the right-hand side graph) light. The desorption was performed for different time durations and after each step, SHG-CD of the surface was measured, again. The stick bars projected on the wall of the graphs show the averaged normalized SHG signal intensities for each SHG measurement.

After each desorption time (each step), the optical activity of the film was probed by the analogous procedure which had been performed before the desorption and described above. I_{SHG}

which is reported in Fig.60 stands for the normalized average of the SHG signal intensities, generated by LCP and RCP light from the samples after each desorption step. The experimental protocol from the data perspective, including all the steps, such as recorded data and corresponding desorption time are also depicted in Fig.60. Each shown spectrum is the average over 25-50 spectra.

All intensities (I_{SHG}) are presented in Fig.61 and the corresponding calculated Δg are illustrated in Fig.62. The g-value calculated from SHG signals of LCP and RCP light is denoted here as g_i. The difference between g_i and g_0 is the g-value evolution which is reported in Fig.62 as Δg. The real-time of exposure (t_e), which is a so-called elapse time, is included in the plot. Elapse time stands for the actual interaction time between light and molecules and considers the pulse duration and the repetition rate of the laser system.

The reproducibility of the data is demonstrated by applying the method on different samples and different spots as well as different wavelengths. Although the data points are scattered, they all follow a similar trend. The fluctuation of the data might be caused by the discrepancies in the thickness and homogeneity of the surface as well as fluctuations of the laser intensity.
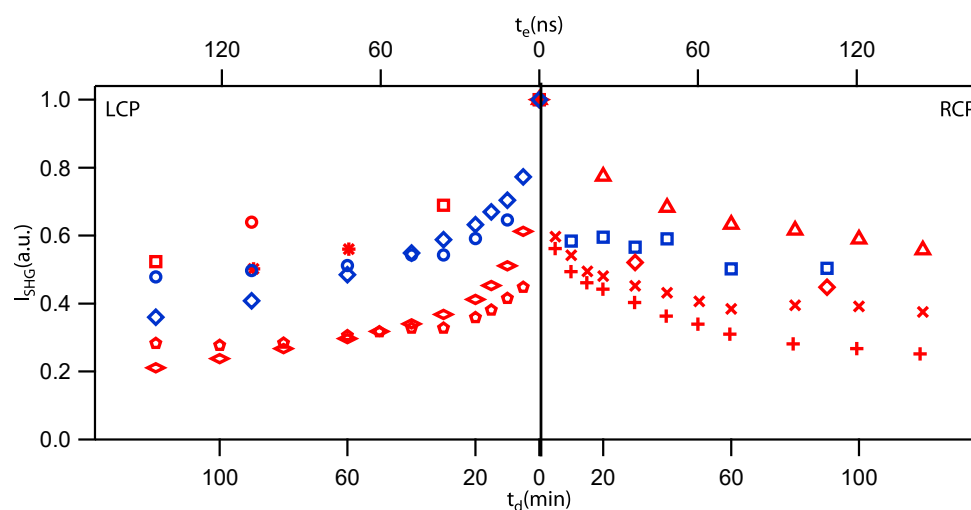
Figure 61- Normalized SHG signal intensities. The presented intensity as I_{SHG} is the averaged of the SHG responses from LCP and RCP light. The measurements were conducted at 600 nm (blue data points) and 650 nm (red data points) and over different samples (different marker symbols). The symmetric behaviour for desorption by LCP (left-hand side) and RCP (right-hand side) was reproducible.
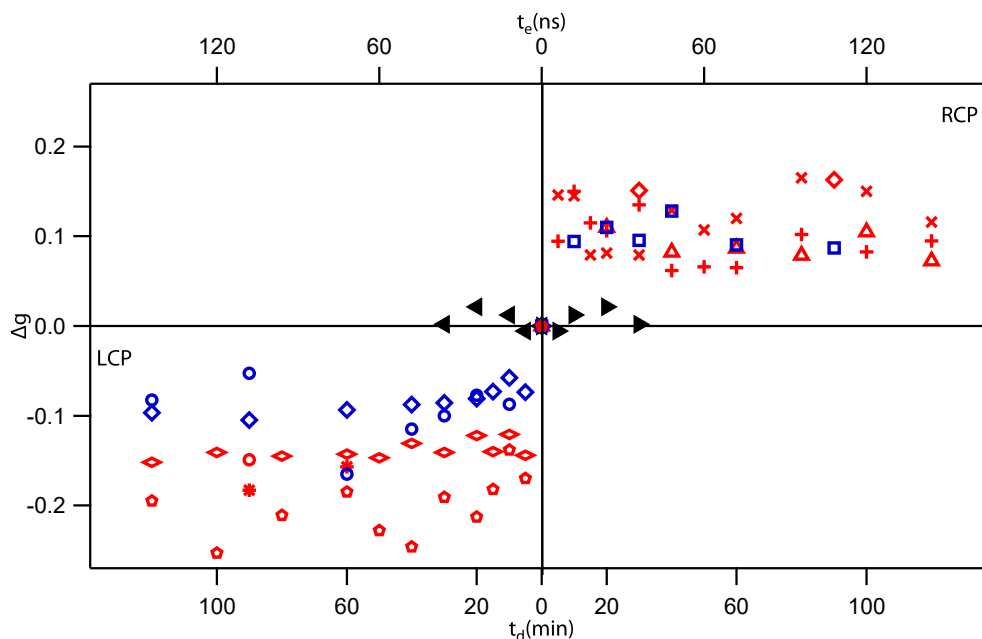
Figure 62- Δg evolution after desorption by LCP (left-hand side) and RCP (right-hand side) light. The blue symbols stand for desorption with 600 nm while the red symbols show desorption with 650 nm. Desorption by linearly polarized light was performed at 670 nm (black symbols). The averaged Δg data recorded from the latter one is mirrored and plotted along with both RCP and LCP light data points in order to make the comparison easier.

As seen in Fig.61, the drop in the intensity of SHG signals for both handedness of circularly polarized light demonstrates that the desorption indeed occurred. An initial fast rate of desorption is concluded by an abrupt drop in the SHG signal intensity within 20 min of desorption time which subsequently became slower and can be seen from the SHG intensities from 20 min onwards. The SHG intensities recorded for BINOL films dropped nearly into half of their amplitude within 120 minutes of desorption. If one follows the behaviour of SHG intensity, plotted in Fig.61, it manifests that the desorption with both handednesses of circularly polarized light is symmetric, regarding the vertical axis. This reveals that the desorption behaviour is regardless of the handedness of the applied light. That can be explained by the fact that the desorption behaviour, which is witnessed here is the sum of the desorption for both R- and S-BINOL in a racemic mixture of the films. Nonetheless, it does not mean necessarily that the partial desorption for these enantiomers is independent of the handedness of circularly polarized light, too. On the contrary, as illustrated in Fig.62, the evolution of the g-value (Δg) is correlated strongly with the handedness of circularly polarized light which was used for desorption. Δg tends to negative values when LCP light was applied, whereas, the other handedness made the

opposite effect on the racemic mixture and Δg values are positive. Moreover, the desorption with linear polarized light did not show any significant effect on the optical activity of the samples, as expected.

The symmetric and antisymmetric behaviours of the desorption and Δg, respectively, were observed for both wavelengths and multiple samples. The appearance of a non-zero Δg in the samples, which were desorbed by circularly polarized light, took only about few minutes and became saturated for longer desorption times. On the other hand, even after 30 min of desorption by linear polarized light, no significant Δg has been observed. The maximum Δg, so-called Δg$_{max}$, arrived at 0.15 which is the averaged value of all Δg$_{max}$ of a different set of data in Fig.62. That indicates a substantial enantiomeric excess (ee) which has been obtained throughout the desorption by circularly polarized light. The enantiomeric excess is defined as:

$$ee \% = \frac{[R] - [S]}{[R] + [S]} \cdot 100 =$$

$$\frac{optical\ activity\ of\ the\ sample = g - value}{optical\ activity\ of\ the\ pure\ enantiomers = averaged\ g_{pure\ anantiomer}} 100 \qquad (81)$$

Where [R] and [S] stand for the amount of each enantiomer in the mixture. The enantiomeric excess can be also calculated based on the recorded SHG-CD signals and derived g-values. Instead of the difference in the amount of both enantiomers at the nominator, one can use the g-value which is calculated for the samples, whereas, the sum of both enantiomers can be replaced by the averaged of the g-values calculated, based on the SHG-CD signals, for the sample of pure enantiomers. Therefore, SHG-CD was performed on the enantiopure samples, which were prepared analogously to the racemic ones. All the conditions for SHG-CD measurements were kept analogous to the previous measurements on the racemic mixture, too. The measured g-values at various positions on the S-BINOL and R-BINOL films are shown in Fig.63. The calculated g-values for each enantiomer yield a strong variation which can be explained by the report of von Weber et al (*163*). They showed that a film of R-/S-BINOL with a thickness of 1.5 μm, is crystallized into domains with a size of 1 mm or smaller. Compared to the spot diameter of the used laser, these domains are small. Therefore, all recorded g-values are the averaged over multiple domains. However, if SHG-CD is performed on these samples within 2-3 hours after the evaporation (*163*), it is likely that crystallization has not started yet.
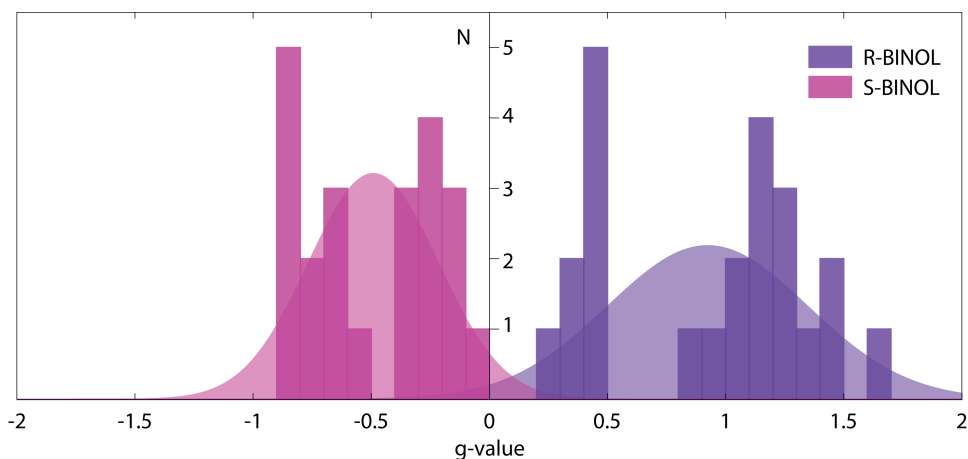
Figure 63- The g-value distribution on the R-BINOL and S-BINOL samples, calculated from SHG-CD measurements.

Based on that, mean g-values of R-and S-BINOL were determined to be 0.92 and -0.49, respectively, which results in an absolute averaged g-value for pure enantiomer as 0.71. Although, this value seems to be in a good agreement with the literature (*29*), no difference between the g-value of R-BINOL and S-BINOL was reported in that literature. The smaller g-value in case of S-BINOL might be correlated to the smaller grain size of the samples. By considering 0.71 as a $g_{pure\ anantiomer}$ (or g_p) in Eq.81, the averaged ee was determined to be 21%.

▪ *Models:*

Because of the sensitivity of the desorption rates on the experimental parameters, the moving average of all data for both wavelengths and samples were calculated, which yields the same behaviour for desorption and Δg, as can be seen in Fig.64. To calculate the moving average, the following equations were used;

$$I_{mean}(t) = \frac{\sum_i w_i I_i(t)}{\sum_i w_i} \tag{82}$$

$$g_{mean}(t) = \frac{\sum_i w_i g_i(t)}{\sum_i w_i} \tag{83}$$

$$w_i(t) = \sum_i exp\left(\frac{-4\log(2).(t_i - t)^2}{100}\right) \tag{84}$$

In order to explain the quantum mechanical nature of the desorption process, a phenomenological rate-equation based model was developed that fits both the absolute desorption I_{SHG} as well as changes in the g-value (Δg). As a first step, it was considered that there are two desorption rates, d_1 and d_2 representing the interaction of S-BINOL with left and right circularly polarized light, respectively. In the case of R-BINOL, d_1 and d_2 are defined vice versa. It should be noted, that these rates depend on the experimental conditions, however, their ratio elucidates the quantum mechanical and thermal contribution in the desorption process. N_S^{LCPL}, N_S^{RCPL}, N_R^{LCPL} and N_R^{RCPL} stand for the number of molecules of the S- and R-enantiomer exposed to LCPL (left circularly polarized light) and RCPL (right circularly polarized light), respectively. One should note that the interaction of molecules in films is regardless of their handedness (*164*). The number of molecules decreases exponentially with desorption time t_d according to the following equations:

$$N_S^{LCPL}(t_d) = \frac{N_0}{1+C_1}(e^{-d_1 \cdot t_d} + C_1) \tag{85}$$

$$N_S^{RCPL}(t_d) = \frac{N_0}{1+C_2}(e^{-d_2 \cdot t_d} + C_2) \tag{86}$$

$$N_R^{LCPL}(t_d) = \frac{N_0}{1+C_2}(e^{-d_2 \cdot t_d} + C_2) \tag{87}$$

$$N_R^{RCPL}(t_d) = \frac{N_0}{1+C_1}(e^{-d_1 \cdot t_d} + C_1) \tag{88}$$

Here N_0 denotes the initial total number of molecules on the surfaces. In the normalized case this is equal to 1. C_1 and C_2 are the remaining non-desorbed molecules after long irradiation times motivated by the fact that the SHG signal did not reach zero during the experiment. C_1 stands for S-BINOL molecules after desorption with left circularly polarized light and R-BINOL molecules with right circularly polarized light, and C_2 stands for S-BINOL molecules with right circularly polarized light and R-BINOL molecules with left circularly polarized light. Furthermore, $RM_1 = \frac{C_1}{1+C_1}$ and $RM_2 = \frac{C_2}{1+C_2}$ represent the ratio of the respective enantiomers on the surface. By these assumptions, the SHG intensities (I_{SHG}) as well as the anisotropy factor (g-value) were calculated according to the linear dependence between the film thickness and the surface SHG efficiency reported in the literatures (*89, 160*).

$$I_{SHG}^{LCPL}(t_d) = \frac{N_S^{LCPL}(t_d) + N_R^{LCPL}(t_d)}{N_S^{LCPL}(0) + N_R^{LCPL}(0)} \tag{89}$$

$$I_{SHG}^{RCPL}(t_d) = \frac{N_S^{RCPL}(t_d) + N_R^{RCPL}(t_d)}{N_S^{RCPL}(0) + N_R^{RCPL}(0)} \tag{90}$$

$$g^{LCPL}(t_d) = g_p \frac{N_S^{LCPL}(t_d) - N_R^{LCPL}(t_d)}{N_S^{LCPL}(t_d) + N_R^{LCPL}(t_d)} \tag{91}$$

$$g^{RCPL}(t_d) = g_p \frac{N_S^{RCPL}(t_d) - N_R^{RCPL}(t_d)}{N_S^{RCPL}(t_d) + N_R^{RCPL}(t_d)} \tag{92}$$

In a first simplified model (red dashed fitting curve in Fig.64), RM_1 and RM_2 values were set to zero. As can be seen, Δg_{max} is saturated after 2 h of measurement. Under the mentioned assumption, the maximum possible g-value of a BINOL film was reached and hence absolute enantio-purification of the film at the irradiated spot (ee = 100%). The generated parameters from this model are summarized in the Tab.5.
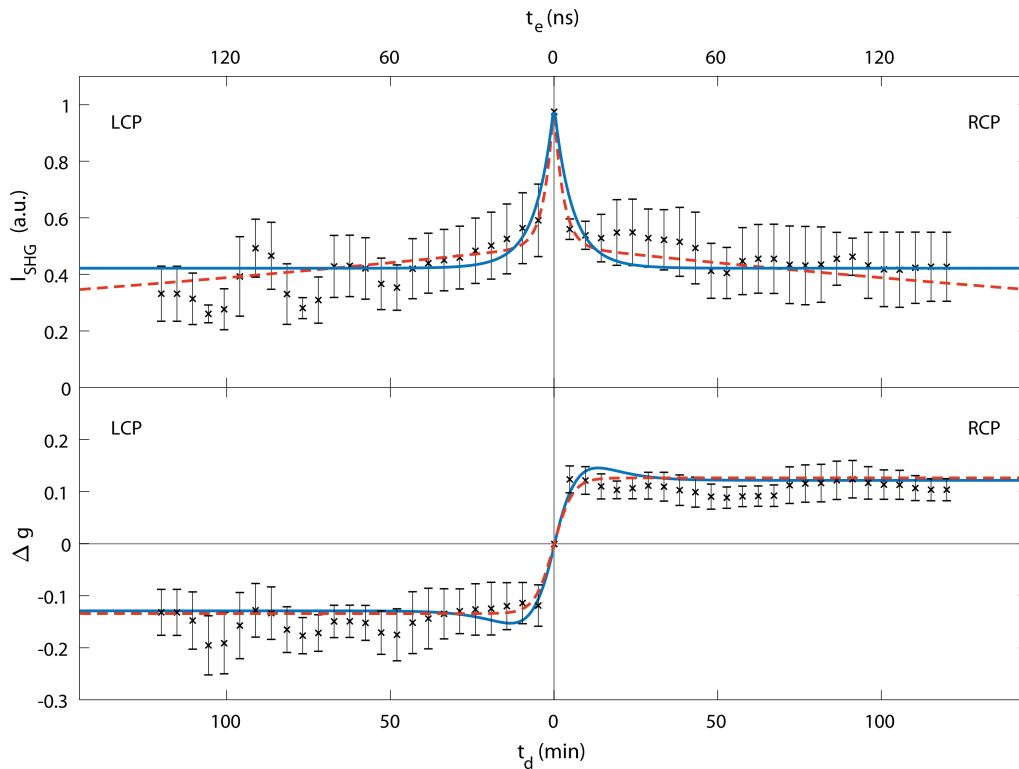

Figure 64- The moving average of all the data obtained at 600 and 650 nm, weighted by Gaussian function. The blue and red lines are the fits according to the two models explained below (see text). The red dashed lines represent the simple model setting no residual molecules, and the blue lines the extended model using g_p = 0.71 from measurements on enantiopure samples.

In order to obtain a conservative estimation of the enantioselective desorption, in the next model, it was assumed that a g-value of the enantiopure samples was 0.71 in accordance with our measurements on enantiopure thin films. Here, RM_1 and RM_2 are 35% and 50 %, which were extracted from the observed SH signals for the longest measurement times, reflecting the different strength of interaction of each enantiomer with left circularly polarized light and right circularly polarized light and the variation in the binding strength of the molecule for different local adsorption and crystallization conformations. As reported in the Tab.5, in this case, $d_2 = 13 \pm 4$ h^{-1} $\cong 1.6 \cdot d_1 = 8 \pm 3$ h^{-1}. The maximum achieved ee of the desorbed samples can be determined by considering $\Delta g_{max} = 0.15$ and g_p, resulting in a conservative estimation of 21% after 13 min of irradiation ($1.78 \cdot 10^6$ laser shots i.e. $t_e = 39$ ns).

Table 5- The summarized parameter extracted from the model.

Figure 3	g_P	d_2 (h^{-1})	d_1 (h^{-1})	RM_1 (%)	RM_2 (%)
Red dashed curve	0.13 ± 0.01	0.15 ± 0.03	21 ± 7	---	---
Blue curve	0.71 ± 0.013	8 ± 3	13 ± 4	35 ± 2	50 ± 2

It should be noted that d_1 and d_2 include contributions from thermal as well as quantum mechanical mechanisms as there was no distinction between the two mechanisms included in the model. For a purely thermal process, it is expected that the value of d_1 and d_2 will be identical. Any deviation from this equality clearly points to the involvements of quantum mechanical mechanisms in the laser desorption process. The values listed in the Tab.5 clearly show that regardless of the chosen approach toward the determination of g_p, d_1 and d_2 are substantially different.

The two proposed models include a quantum mechanical desorption process which expresses itself in a different desorption rate (d_1 and d_2) for one enantiomer if excited either with left or right circularly polarized light. The results of the two models can be summarized as the following: in the first and second model, both I_{SHG} and Δg were fitted simultaneously. In the first model, due to the saturation of Δg, the ratio of the enantiomers on the surface was considered zero and consequently ee % = 100. The extracted values from the fit showed $g_p = 0.13 \pm 0.01$ and a huge difference between two desorption rates d_1 and d_2. Since it is expected to have equal

desorption rates in the case of thermal desorption, the latter discrepancy indicated the dominant role of the quantum mechanical processes. In the second model, the experimentally measured g_p = 0.71 of enantiopure films was used for the fit and led to an ee % = 21 after only 13 min of desorption and again a significant difference between the two desorption rates. The latter is in an agreement with the first model.

- *Conclusion:*

This study indubitably demonstrates that laser desorption with the help of circularly polarized light leads to the enantioselective desorption of different enantiomers of chiral molecules, in this case, BINOL, from achiral surfaces. The behaviour observed for Δg (Fig.62), yields the significant influence of left and right circularly polarized light on the desorption which created Δg in the samples, whilst this phenomenon was not observed for desorption with linear polarized light. Furthermore, quantum mechanical mechanisms of desorption seem to play a great role. Conclusively, enantiospecific desorption by circularly polarized light cannot be considered as pure thermal desorption. The interaction of circularly polarized light with the enantiomers, i.e. quantum mechanical processes should also be taken into account as a non-negligible but even significant process in the enantiospecific desorption by circularly polarized light. All measurements performed in this section point out the fact that enantiomeric enrichment by applying circularly polarized light is possible and can be a suitable replacement of the conventional methods.

5. *Summary and outlook*

Throughout this work, which was divided into three chapters, chiral molecules were investigated by three different techniques.

In the first chapter, R-(+)-1-phenylethanol as a volatile chiral molecule was investigated via (1+1) CD-REMPI-MS. Within this study, the vibronic transitions of $\pi \longrightarrow \pi^*$ of the phenyl ring of R-(+)-1-phenylethanol were investigated. Thanks to the supersonic expansion, the created cooled molecular beam in combination with CD-REMPI-MS technique gave us the possibility to calculate g-values for individual vibronic transitions. In addition, in synergy with the theory, it was revealed that simultaneous comparison between the absorption and the g-value of computed and experimental data is crucial to assign vibrational modes to the observed transitions. The most pronounced example was the transitions related to the out-of-plane and in-plane deformation of ring modes at 534.22 and 543.14 cm^{-1}. In this case, a consideration of only the position and amplitude of the absorption bands caused an ambiguity in assignments. This problem could be resolved after a simultaneous comparison between absorption bands and g-values for both experimental and computed data.

Furthermore, to extend all the techniques, which are able to perform on volatile chiral molecules, to non-volatile chiral molecules, the main apparatus was equipped with a laser desorption source. The design and integration of a new source, as well as the adaption of the main set-up, was the main objective of the second chapter. Despite numerous described experimental challenges, the mass spectrum of BINOL was acquired, successfully. However, the signal stability needs to be improved to be able to perform CD-REMPI measurements on this molecule. Further modifications to the sample preparation and the diameter of the desorption laser are suggested. Moreover, one can differ the sample rod material to inspect the role of the substrate in the desorption process, e.g. semiconductor material or a rod coated with a semiconductor material. Furthermore, the investigation of the intramolecular interaction between non-volatile and volatile molecules in the gas phase is now possible with the new desorption source. That also paves the way for probing the interaction between chiral and achiral molecules and measuring induced circular dichroism (ICD). ICD unlike CD is caused by intramolecular interactions. These interactions are mostly investigated in solutions, where broad absorption bands and vibrationally

unresolved spectra were recorded. In order to obtained well-resolved vibronic transitions of the isolated complexes in the gas phase, a cooled molecular beam of the volatile molecules and desorbed molecules could be investigated. The information acquired via ICD plays a pivotal role in the determination of the structure, configuration and binding characterization of each conformer. The inspection of the binding between chiral and achiral molecules is significantly important in the field of enantioselective synthesis and asymmetric catalysis (*165*).

In the last chapter, the concept of laser desorption was developed further by the usage of circularly polarized light instead of linearly polarized light. The aim was to desorb one enantiomer of chiral molecules with one of the handedness of circularly polarized light more than the other enantiomer which leads to the enantiomeric enrichment of a racemic mixture. To probe such a phenomenon, a racemic mixture of BINOL was used and both handednesses of the circularly polarized light impinged on the surface in individual experiments. To inspect the changes made by each handedness, SHG-CD was carried out. The evolution of g-values of the desorbed surface, demonstrated the different responses of the enantiomers to the different handedness of circularly polarized light, implying enantiospecific desorption by circularly polarized light. This approach seems promising for the application in pharmaceutical research or even industry, where enantiomeric enrichment matters significantly. The enantiomeric excess obtained throughout our experiments is small, nevertheless, yields the capacity of the method to be modified further for the enantiomeric enrichment purpose. This method could be also valuable in the heterogeneous asymmetric catalysis, by which the separation of non-volatile reaction products is plausible. In addition, enantiospecific desorption indicates the fact that laser desorption is not only ruled by the thermal process but also affected greatly by quantum mechanical mechanisms. In order to have more insights into the contributions of these mechanisms, more experiments need to be performed. The comparison between different substrates and various wavelengths (resonant/non-resonant) may also help with a profound understanding of the mechanism behind enantiospecific desorption.

6.   The list of the patent and publications

A. Patent: A. Kartouzian, U. Heiz, F. Mortaheb, K. Oberhofer, J. Riemensberger, H. Iglev, R. Kienberger, Method for enantiomeric enrichment. *Deutsches Patent- und Markenamt* **10 2018 117 346.6** (submitted 2018).

B. J. Lepelmeier, J. L. A. Gomez, F. Mortaheb, U. Boesl, U. Heiz, A. Kartouzian, Chiroptical inversion for isolated vibronic transitions of supersonic beam-cooled molecules. *Physical Chemistry Chemical Physics* **19**, 21297-21303 (2017).

C. F. Santoro, F. Mortaheb, J. Lepelmeier, U. Boesl, U. Heiz, A. Kartouzian, High-resolution absorption and electronic circular dichroism spectra of (R)-(+)-1-phenylethanol. Confident interpretation based on the synergy between experiments and computations. *ChemPhysChem* **19**, 715-723 (2018).

D. F. Mortaheb, K. Oberhofer, J. Riemensberger, F. Ristow, R. Kienberger, U. Heiz, H. Iglev, A. Kartouzian, Enantiospecific desorption by circularly polarized light, (to be submitted).

Publication C

High-Resolution Absorption and Electronic Circular Dichroism Spectra of (R)-(+)-1-Phenylethanol. Confident Interpretation Based on the Synergy between Experiments and Computations

Fabrizio Santoro,*[a] Farinaz Mortaheb,[b] Jörn Lepelmeier,[b] Ulrich Boesl,[b] Ulrich Heiz,[b] and Aras Kartouzian*[b]

Using density functional theory and its time-dependent extension for excited states, the $S_0 \rightarrow S_1$ high-resolution vibronic absorption and electronic circular dichroism spectra of (R)-(+)-1-phenylethanol are computed and compared to experimental spectra measured in jet-cooled conditions in the region within 1000 cm^{-1} of the 0–0 transition. The agreement between theory and computation is satisfactory and allows a confident assignment of several experimental bands in terms of funda-
mentals of different modes. Cases are documented for which the analysis of optical anisotropy factors, owing to their signed nature, remarkably enhances the possibility of a robust assignment of the experimental absorption bands. Computational analysis shows that the experimental spectra are dominated by Herzberg–Teller contributions and that the electronic circular dichroism spectrum and the anisotropy factors are also strongly modulated by the effect of Duschinsky mixings.

1. Introduction

Computational methods are sufficiently developed to provide important help in the interpretation of the results of several different spectroscopies.[1] For chiral molecules, the comparison between chiroptical spectra and computational predictions is now the method of choice for the assignment of absolute configurations.[2–4] In the field of electronic spectroscopy, recent advances have made standard the possibility to go beyond a pure "vertical" approach,[5] and to predict the entire lineshape of the spectra accounting for vibronic contributions. These methods can be combined with convenient computational methods such as density functional theory (DFT) and its time-dependent (TD) extension (TD-DFT) for excited states; in this way they can be applied also to large systems if they are somewhat rigid. The recently reported possibility to introduce anharmonic corrections further improves the accuracy of the simulations,[6] whereas the usage of internal coordinates allows

remarkable progress to be made also for large molecules characterized by soft modes.[7–10]

In his seminal work,[11] Weigang highlighted that, for weak transitions, the electronic circular dichroism (ECD) spectra in the region of a single electronic state can actually be characterized by bands with different signs. This is an effect of interstate couplings and intensity-borrowing mechanisms. The vibronic methodologies developed in the last 15 years have been demonstrated to be able to reliably reproduce this effect in a number of systems, such as ketones with isotopically engendered chirality,[12] methylcyclopentanone,[13] alkyl derivatives of benzene,[14] dimethyloxirane[15,16] and helicenes.[17] In all these cases, computations were compared with experimental spectra in solution, characterized by a limited vibronic resolution.

High-resolution vibronic spectra measured in supersonic jets yield much more detailed information but they are also more challenging for computational simulations. In comparing calculations to these experimental data, one usually considers the position and intensity of the predicted bands and looks for pattern similarities to obtain the best match.[18,19] However, both the positions and intensities of the calculated transitions will be slightly off compared to the experimental data, due to the inherent property of the models considered for the calculations and the assumptions that are made.[20] In congested spectra, even the order of the energies of neighboring bands can be altered.[21–23]

In this work we demonstrate that in the case of chiral molecules, measuring optical anisotropy factors can enhance confidence in the assignment of peaks in high-resolution spectra. On the theoretical side, no new calculation costs would be im-

[a] Dr. F. Santoro
Istituto di Chimica dei Composti Organometallici
Consiglio Nazionale delle Ricerche
Area della Ricerca, via G. Moruzzi 1
I-56124 Pisa (Italy)
E-mail: fabrizio.santoro@iccom.cnr.it

[b] F. Mortaheb, J. Lepelmeier, Prof. U. Boesl, Prof. U. Heiz, Dr. A. Kartouzian
Catalysis Research Center
Technische Universität München
Chair of Physical Chemistry
Lichtenbergstr. 4, 85748 Garching (Germany)
E-mail: aras.kartouzian@tum.de

Supporting Information and the ORCID identification number(s) for the author(s) of this article can be found under:
https://doi.org/10.1002/cphc.201701254.

posed, because the information necessary to determine the optical anisotropy factors (the amplitude and direction of magnetic and electric dipole moments) are already available from the calculations that would be performed to determine the position and intensity of the bands.

As a test case, we chose jet-cooled (R)-(+)-1-phenylethanol (Figure 1). Some of us recently showed that the anisotropy fac-
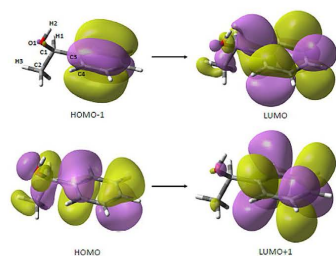

Figure 1. Relevant Kohn–Sham orbitals computed at the ground-state equilibrium geometry of the most stable conformer optimized at the CAM-B3LYP/TZVP level of theory.

tors (g values) of the vibronic bands associated with the lowest electronic transition, known as L_b according to Platt nomenclature, have variable signs and amplitudes, depending on the excited vibrational modes.[24] In this contribution we first present, at different levels, theoretical calculations of the vibronic spectra of the system, and discuss the most suitable model. On the basis of these calculations we provide a confident assignment of many of the observed bands. Furthermore, we focused on a pair of adjacent vibronic peaks and repeated the experimental measurements of Ref. [24]. Comparison of experimental and theoretical findings clearly demonstrates the benefit of including g values in the analysis and assignment of these transitions.

Theoretical and Experimental Details

Computations

Electronic computations were performed using DFT for the ground state (GS) and its TD-DFT extension for the lowest excited state (ES). We adopted the CAM-B3LYP/aug-cc-pVTZ level of theory, but to study the effect of different functionals and different basis sets we also repeated the calculations with CAM-B3LYP, B3LYP, and M062X in combination with the TZVP basis set. Different conformers were located with a two-dimensional relaxed scan along the H2–O1–C1–H1 and C4–C3–C1–H1 dihedral angles (see Figure 1 for atom labels) followed by optimization of the candidate minima. Vibronic calculations were performed with the time-independent method[25,26] implemented in our code FCclasses.[27] We adopted the adiabatic Hessian (AH) model,[28] where both GS and ES potential energy surfaces are represented by a quadratic expansion around their respective equilibrium geometries. The AH model allowed to include the effect of displacements, frequency changes and Duschinsky mixings. The importance of frequency changes and Duschinsky mixings have been investigated by comparison with the predictions of a simplified model, adiabatic shift (AS),[28]

where the ES potential energy surface is expanded around the same ES equilibrium geometry. However, it is assumed that it shares the same normal modes and frequencies of GS. The electronic μ and magnetic $\mathbf{m}$ transition dipoles were linearly expanded as a function of the normal coordinates, and calculations were performed either retaining only the constant terms of the expansion, (Franck–Condon, FC, approximation) or considering also their linear terms (Herzberg–Teller, HT, approximation). In the discussion that follows, a calculation including both FC and HT contributions is termed FCHT. Because in principle μ and $\mathbf{m}$ are not linear functions of the normal coordinates, results might be different for linear expansions around the geometry of the initial (i) state (i.e. GS) or of the final (f) state (i.e. ES).[28] Therefore, in order to check the reliability of the HT approximation, for CAM-B3LYP/aug-cc-pVTZ we repeated the calculations with both an HT expansion around i (HTi) and around f (HTf) equilibrium geometries. For comparison with experiments, g values spectra, that is, the ratio of ECD and ABS intensities were computed as well. Calculations were performed at 0 K in the gas phase.

Experimental Details

The experimental set-up used in this work consisted of a vacuum chamber comprising a pulsed general valve, ion source, a linear Wiley–McLaren time-of-flight mass spectrometer, multichannel plates, and a dye laser system. The pulsed general valve with a 0.2 mm aperture was used to generate a supersonic beam. It was pulsed synchronously with the dye laser system with a 30 Hz repetition rate. Argon, with a backpressure of 2.8 bar, was used as the carrier gas for supersonic beam expansion. All measurements were performed under vacuum conditions and with a background pressure of 4×10^{-6} mbar. Under these conditions, a molecular jet with a temperature of less than 10 K was achieved. The dye laser system used here was pumped by a Nd:YAG laser and gave a spectral linewidth of 0.04 cm^{-1}. The desired wavelength to investigate the transition $\pi \rightarrow \pi^*$ of (R)-(+)-1-phenylethanol (259–266 nm) was generated by the frequency-doubled emission of coumarin 153 dissolved in ethanol (1.6 g L^{-1}). To create circularly polarized light for CD–resonance-enhanced multiphoton ionization, a quarter-wave plate was located in the laser path to the vacuum chamber. The produced supersonic molecular beam is guided through the ionization region where it is exposed to the laser beam. The ions created here are accelerated and fly through the TOF apparatus and are detected at a multichannel plate.

In order to apply the twin-peak method, it is necessary to have a double laser beam overlap with the molecular beam. This can be achieved by reflecting the laser pulse back into the ionization region with a mirror on the opposite site of the vacuum chamber with an angle of 0°. Reflection switches the handedness of the circularly polarized light from left to right and vice versa. Accordingly, a single laser pulse can be used to generate ions by both circular polarizations at two different spots of the molecular beam. These ions can be detected separately in a single mass spectrum. Further details on the experimental setup and data treatment can be found in Refs. [24], [29] and [30].

2. Theoretical Results

The conformational analysis (details are provided in the Supporting Information) revealed the existence of five stable conformers and predicted that only the most stable one (Figure 1) is populated at the low temperature of the molecular jet (<

Table 1. Vertical transition energies E_v [eV], oscillator strength f (dimensionless), rotatory strength R [10^{-40} cgs] (calculated within the length gauge) for the most stable conformer of (R)-(+)-1-phenylethanol.

	S1			S2			S3			S4		
	E_v[a]	f	R	E_v	f	R	E_v	f	R	E_v	f	R
CAM-B3LYP/aug-cc-pVTZ	5.45	0.0003	−0.47	6.05	0.036	−0.06	6.30	0.005	6.31	6.52	0.0005	−2.55
CAM-B3LYP/TZVP	5.49	0.0004	−0.52	6.13	0.029	−0.06	6.96	0.44	40.53	7.02	0.42	10.90
B3LYP/TZVP	5.31	0.0006	−0.60	5.88	0.047	0.004	6.34	0.022	8.12	6.38	0.051	5.92
M062X/TZVP	5.53	0.0007	−0.68	6.29	0.036	−0.16	7.01	0.57	35.48	7.03	0.43	11.85

[a] E_{00} values corresponding to the $S_0 \rightarrow S_1$ transition are 5.18, 5.21, 5.02 and 5.24 eV, respectively, according to CAM-B3LYP/aug-cc-pVTZ, CAM-B3LYP/TZVP, B3LYP/TZVP and M06-2X/TZVP.

10 K). Therefore in the following, we consider this conformer only. In Table 1 we report the vertical excitation energy (E_v), and the oscillator (f) and rotatory (R) strengths for the first four lowest singlet excited states (S_1–S_4) of the system as predicted by the functionals CAM-B3LYP, B3LYP and M06-2X in combination with the TZVP basis set. For CAM-B3LYP, results with the larger aug-cc-pVTZ basis sets are also provided. Vibronic calculations focused on the $S_0 \rightarrow S_1$ transition. Therefore in the Table we also report the transition energy between the ground vibrational states of S_0 and S_1 (E_{00}).

A similar description of S_1 is provided by all the adopted computational methods. With the smaller TZVP basis set it is a symmetric combination, with approximately equal weights of HOMO-1→LUMO and HOMO→LUMO+1 transitions (see Figure 1). With the more diffuse basis set aug-cc-pVTZ, additional contributions appear. In all cases, S_1 is characterized by a small oscillator strength and a small negative rotatory strength. As expected, CAM-B3LYP and M062X predict larger E_v values for S_1 than B3LYP. For CAM-B3LYP, the increase of the basis set from TZVP to aug-cc-pVTZ leads to small changes. The experimental E_{00} value is 4.66 eV,[24] therefore the B3LYP result (TZVP) is blueshifted by 0.36 eV, whereas the best CAM-B3LYP estimate (aug-cc-pVTZ) is off by 0.52 eV. The description of S_2 is also rather similar for the three functionals. In particular it is a weak absorber and has a small rotatory strength. According to CAM-B3LYP/TZVP and M06-2X/TZVP, S_3 and S_4 have large oscillator strengths and large and positive rotatory strengths. Therefore S_1 might borrow absorption and ECD intensity from these two states with a HT mechanism. B3LYP yields quite different predictions for S_3 and S_4, which are much more stable and have small f, whereas S_5, S_6 and S_7 (at 6.85, 6.94 and 6.97 eV) have large f (0.22, 0.43, 0.39) and R (61.87, −44.13, −31.00) and are likely involved in HT mechanisms. The picture is more complex also if diffuse basis sets are adopted. CAM-B3LYP/aug-cc-pvTZ in fact predicts the existence of Rydberg-like states S_3–S_5 with weak oscillator strengths that have intermediate energies between S_1–S_2 and a group of strongly absorbing ($f = 0.08$, 0.24, 0.39, 0.31) states, S_5–S_8, with $E_v = 6.66$, 6.83, 6.87, and 6.96 eV, likely involved in the HT mechanism. Although B3LYP shows the best performance on the energy of S_1 state, it is known that it is not fully adequate for describing high-lying energy states, which are important for a reliable description of HT effects.

In Figure 2 we initially compare FC, FCHTf and FCHTi stick spectra, adopting the CAM-B3LYP/aug-cc-pVTZ level of theory with the AH model for absorption (ABS), with ECD spectra. HT effects have a huge impact on the spectra. In particular they are responsible for the intensity of the bands at approximately 400–600 cm^{-1} and for the appearance of bands with alternating signs in the ECD spectrum. The FCHTf and FCHTi predictions for ABS and ECD spectra are very similar, which supports the reliability of a FC+HT approximation, that is, of a first-order expansion of the transition dipoles. On this basis, for the following analysis we selected the FCHTf model. In the Supporting Information we report the computed spectra obtained with all the adopted levels of theory. In particular we analyze the effect of the basis set comparing the results of CAM-B3LYP/aug-cc-pVTZ and CAM-B3YP/TZVP, and the effect of the functionals comparing the predictions of CAM-B3LYP with those of B3LYP and M06-2X in combination with the TZVP basis set. We note that preliminary M06-2X calculations were already reported in Ref. [24] to help the qualitative interpretation of spectra, without however attempting an explicit calculation of the vibronic transitions. In general, results obtained at different levels of theory are rather similar, thus supporting the robustness of our predictions, and all are in reasonable agreement with experimental data.

In Ref. [14] we showed that the CAM-B3LYP/TZVP level of theory provides a good description of the FC and HT contributions of the L_b transition of closely related alkylbenzene derivatives [(R)-PhCH(CH$_3$)tBu and (R)-PhCH(CH$_3$)iPr]. Consistent with those results, in the following section we focus our discussion on the CAM-B3LYP results. Moreover, we mainly consider the results that, according to theory, should be more reliable, that is, those obtained with the larger basis set.

2.1. Comparison with Experiment in a Supersonic Jet

In this section we compare the computed stick transitions to experimental spectra measured in supersonic jets. We consider both absorption and the anisotropy factor g obtained by the ratio of the ECD and ABS intensities. In experiments, g was measured only for selected bands having non-negligible ABS intensities.[24] Due to the inherent inaccuracies in any computational model it is not possible to establish a one-to-one correspondence between experimental and computed bands only based on the matching of the frequencies; therefore it was not
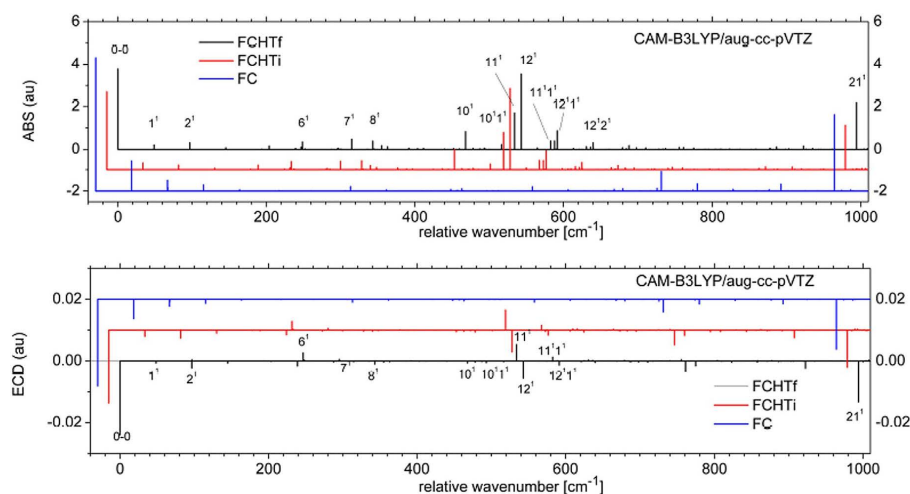
114

Figure 2. ABS (top) and ECD (bottom) spectra computed at the CAMB3LYP/aug-cc-pVTZ level of theory with the AH model and FCHTf, FCHTi and FC approximations for the transition dipoles. The FCHTf bands have been assigned as x^x where x indicates the excited-state normal mode and x the number of quanta ($n^x m^y$ are combination bands). For better visualization, an offset along both the x and y axes has been applied to FC ([−30, −2] for ABS and [−30, 0.02] for ECD) and FCHTi ([−15, −1] for ABS and [-15, 0.01] for ECD) results.

possible to be sure to compute the *g* factors of the bands corresponding to those analyzed in the experiment. Conversely, reporting the *g* factors for all the vibronic bands computed in ABS and ECD spectra would create spectra that are too congested (very weak ABS intensities can correspond to very large *g* values). Moreover, it is expected that for weak ABS bands (in most of the cases not considered in the experiment) the inherent inaccuracy of ABS and ECD intensities can actually give rise to very large numerical errors in the *g* values. Therefore, for computations, we decided to set a threshold on the ABS intensity and to report the *g* value for all the bands for which ABS intensity is larger than a given fraction (specifically 5%) of the most intense one. This procedure might cause the appearance/disappearance of bands unseen/seen in the experiment. The *g* values for bands selected with different threshold values (from 0.1% to 10%) are reported in the Supporting Information.

Although we focus on CAM-B3LYP/aug-cc-pVTZ results, as mentioned above and shown in the Supporting Information, similar comments would also hold for the other combinations of DFT functionals and basis sets we checked. A visual comparison of computed and experimental spectra is reported in Figure 3. All but one of the bands presented in the experimental spectra are taken from Ref. [24]. Motivated by the computational findings that are presented in this work the band E2 has been measured additionally and is included in the spectrum shown in Figure 3.

Our calculations correctly predicted that the ABS spectrum is characterized by a strong 0–0 band, weak bands in the region 250–350 cm^{-1}, a cluster of bands dominated by a central peak at 450–550 cm^{-1} and a band at approximately 900–1000 cm^{-1}. Computed bands are slightly blueshifted, and the largest error

was apparent for the one centered at approximately 994 cm^{-1}, which was observed at 927 cm^{-1} by experiment. Interestingly, the intensities of the strong bands observed at approximately 500 cm^{-1} are almost entirely attributed to HT effects (compare FC and FCHT computations in Figures 2). The negative *g* values of the 0–0 band and of the band centered at 994 cm^{-1} (computed result) are correctly reproduced, as well as the positive *g* value of the band centered at approximately 250 cm^{-1}. In Figure 3, fundamental and overtone computed bands are assigned the label n^x where n is the ES normal mode and x is its quantum number. Similarly, for combination bands of modes n and m with quantum x and y we adopted the label $n^x m^y$. Modes not explicitly reported are in their ground state. The most relevant ES modes are sketched in Figure 4.

Based on these calculations we can revisit the assignment of the main bands attempted in Ref. [24] using literature data. The band at 927 cm^{-1} observed by experiment is due to the fundamental of mode 21, a ring breathing mode, thus confirming the previous assignment. Similarly, the band centered at 242 cm^{-1} in the experimental (248 cm^{-1} in the calculation) is due to the torsion of the rotation of the CH$_3$ group. The band centered at 462 cm^{-1} in the experiment was assigned to a CH$_3$ bending in Ref. [24]. The computed band at 468 cm^{-1} (10^1) approximately reproduces the relative ABS experimental intensity with respect to the band maximum and exhibits the same sign for the anisotropy factor, although its value is strongly underestimated. We thus assigned the experimental band to 10^1 and confirmed that it has a contribution from the bending of CH$_3$, although it is strongly coupled with the C—C—O bending.

Significant discrepancies with the experimental data were also found: 1) the position and relative intensity of the experimental absorption band at approximately 330 cm^{-1} appears to
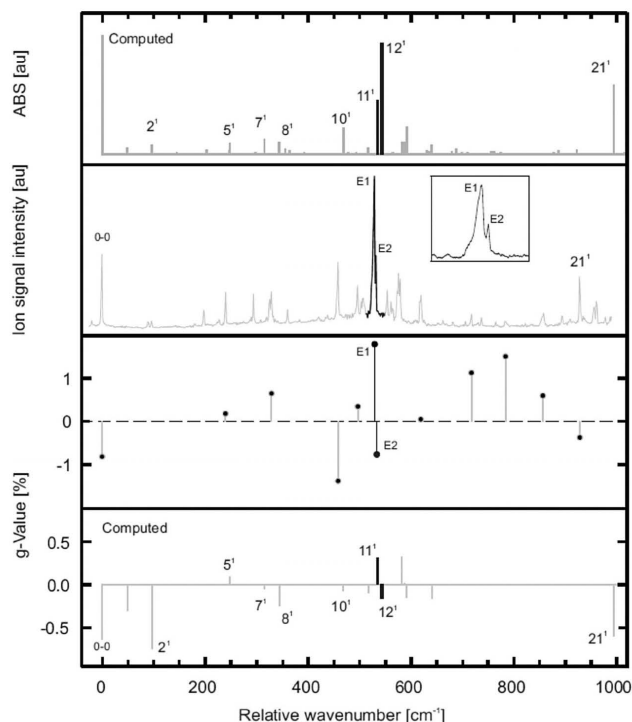
Figure 3. Comparison of experimental (central panels) and theoretical (top and bottom panels) spectra computed at the CAM-B3LYP/aug-cc-pVTZ level of theory.

be nicely reproduced by computed band 8^1. In Ref. [24] it was assigned to a ring deformation, and actually mode 8 is a deformation of the ring coupled with H—C—OH torsion. However, the experimental band has a positive g value, whereas the computed 8^1 has a negative g. The same is true for the neighbor 7^1 band. These findings indicate that the assignment based only on the ABS spectrum might not be sufficiently robust, highlighting the importance to consider g values too. In this specific case, after comparing g values, we concluded that we could not provide a confident assignment for this experimental band. It is possible that our calculations predict too strong of a coupling between the ring deformation and the H—C—OH torsion and that this is the cause of the wrong g sign of the theoretical band.

The importance of the measurement and calculation of the g factors for the proper assignment of the bands can be further emphasized by focusing on the computed transitions 11^1 and 12^1, positioned at relative wavenumbers of 534.22 and 543.15 cm^{-1}, which correspond to the fundamentals of an out-of-plane and an in-plane deformation of the ring, respectively. By considering only the position and absorption intensity of the predicted bands, one might conclude that the experimentally observed transition at 528.92 cm^{-1} (E1) and its shoulder at 531.83 cm^{-1} (E2), which are the two most intense bands in this

region, correspond to 12^1 and to 11^1, respectively. The main discrepancy with the experimental data would be attributed to an inaccuracy on the computed frequencies that swaps the bands, and could be explained with the approximations in the level of electronic theory or the lack of proper anharmonic corrections.

However, by including g values of the bands into the assignment process, we arrive at a different conclusion. The sign and even the relative amplitude of the calculated g values for 11^1 and 12^1 bands are in good agreement with the experimental data for E1 and E2. Thus it is more likely that the order of the theoretically predicted bands is indeed correct and that E1 has a main contribution from the out-of-plane deformation (mode 11) and E2 from the in-plane one (mode 12). M06-2X, B3LYP and CAM-B3LYP spectra computed with the TZVP basis set supported this conclusion (see the Supporting Information). In view of these new results, the discrepancies in the relative ABS intensities cannot be explained simply on the basis of errors in the frequencies. On the contrary, inaccuracies in the wavefunctions (ultimately responsible for the intensities) must play a role.

This approach demonstrates how including ECD data as part of a comparison of experimental and theoretical results might provide new tools for assigning transition bands, thus helping
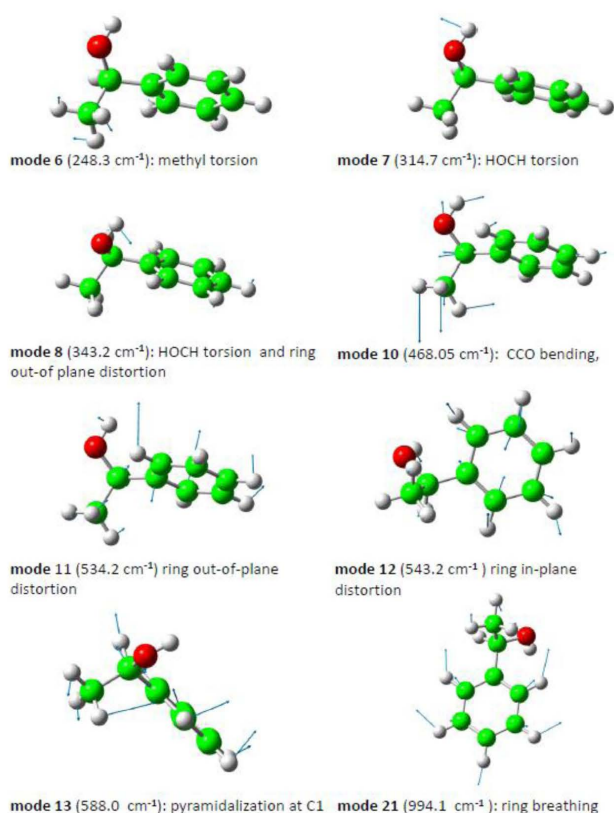
116

mode 6 (248.3 cm⁻¹): methyl torsion

mode 7 (314.7 cm⁻¹): HOCH torsion

mode 8 (343.2 cm⁻¹): HOCH torsion and ring out-of plane distortion

mode 10 (468.05 cm⁻¹): CCO bending,

mode 11 (534.2 cm⁻¹) ring out-of-plane distortion

mode 12 (543.2 cm⁻¹) ring in-plane distortion

mode 13 (588.0 cm⁻¹): pyramidalization at C1   mode 21 (994.1 cm⁻¹): ring breathing

Figure 4. Excited-state modes relevant for ABS, ECD or g spectra computed at the CAM-B3LYP/aug-cc-pVTZ level of theory.

to gain a better understanding of the correlation between theory and experiment.

2.1.1. The Importance of Frequency Changes and Duschinsky Mixings for a Satisfactory Comparison with Experiment

In the previous sections we highlighted the existence of large HT effects on the absorption, ECD and g spectra. Here we describe the relevance of frequency changes and Duschinsky mixings between GS and ES modes. To that end, we used the FCHTf model and compared AH spectra with those obtained with the simpler AS model (Figure 5), for which it is assumed that the ES has the same normal modes and frequencies of the GS. Figure 5 clearly shows that frequency changes and Duschinsky mixings have a remarkable effect on ABS and even more on ECD and g spectra. The effect of frequency changes is evidenced by the fact that in general AS bands are more blue-shifted with respect to the 0–0 than the corresponding AH bands. The effect of Duschinsky mixings is even more remarkable as they introduce significant changes in the relative intensities.

Let us focus on the bands at approximately 500–550 cm⁻¹. ES modes 11 and 12 are characterized by strong Duschinsky mixings. Four GS modes are necessary to project them more than 90%. ES mode 11 is projected on GS modes 11, 10 and 12 with weights 0.33, 0.29 and 0.28, respectively. By contrast, ES mode 12 is projected by 0.63, 0.13 and 0.10 on GS modes 12, 13 and 11, respectively. In the ABS spectrum obtained with the FCHTf│AS model, that is, neglecting Duschinsky and frequency changes, the strongest band has the same formal assignment 12¹ as in the AH model but now it corresponds to a GS mode that falls at a higher frequency and this justifies the blueshift with respect to the AH results.

The most striking change is that, the positive and negative ECD peaks at approximately 500 cm⁻¹ observed with the AH model are almost completely quenched in the AS model. A weak ECD activity is shown by band 10¹. However, because it has an even weaker ABS intensity, this results in a large and negative g value, which has no counterpart in the experimental data.

To find a rationale for these results, we report an expression for the ECD intensity of a fundamental n^1, where n is the ES
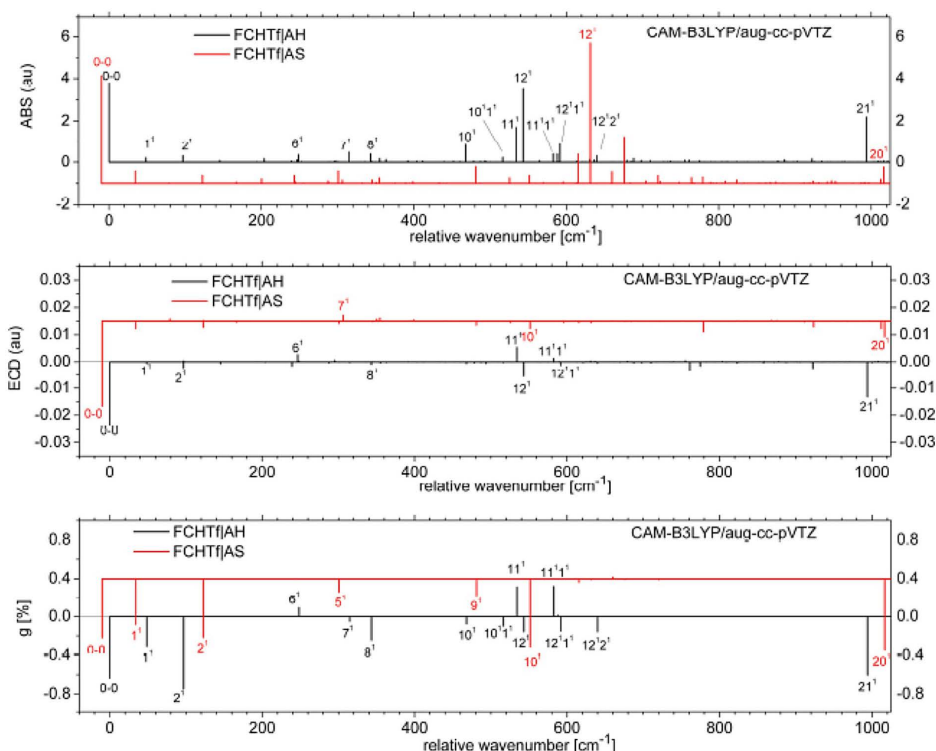
117

Figure 5. Comparison of experimental (central panel) and theoretical (top and bottom panels) spectra computed at the CAM-B3LYP/aug-cc-pVTZ level of theory.

normal mode Q_n (dimensionless coordinates) [Eq. (1)]:

$$I_n^1 \propto \langle 0_{GS}|\mu|(0+1_n)_{ES}\rangle \langle (0+1_n)_{ES}|\mathcal{I}\mathbf{m}|0_{GS}\rangle = \mathbf{a}\cdot\mathbf{b} \tag{1}$$

where [Eq. (2)]:

$$\mathbf{a} = \mu_0\langle 0_{GS}|(0+1_n)_{ES}\rangle + \left(\frac{\langle 0_{GS}|0_{ES}\rangle}{\sqrt{2}} + \langle 0_{GS}|(0+2_n)_{ES}\rangle\right)\left(\frac{\partial\mu}{\partial Q_n}\right) +$$

$$\sum_{j\neq n}\frac{\langle 0_{GS}|(0+1_n+1_j)_{ES}\rangle}{\sqrt{2}}\left(\frac{\partial\mu}{\partial Q_j}\right)$$

$$\mathbf{b} = \mathcal{I}\mathbf{m}_0\langle(0+1_n)_{ES}|0_{GS}\rangle + \left(\frac{\langle 0_{GS}|0_{ES}\rangle}{\sqrt{2}} + \langle(0+2_n)_{ES}|0_{GS}\rangle\right)\left(\frac{\partial\mathcal{I}\mathbf{m}}{\partial Q_n}\right) +$$

$$\sum_{j\neq n}\frac{\langle(0+1_n+1_j)_{ES}|0_{GS}\rangle}{\sqrt{2}}\left(\frac{\partial\mathcal{I}\mathbf{m}}{\partial Q_j}\right) \tag{2}$$

In the above equations, $\mathcal{I}$ indicates the imaginary part, $\mathbf{0}_{GS}$ and $\mathbf{0}_{ES}$ are the ground vibrational states of the GS and ES, respectively, and $(0+1)_{ES}$ is a state of the ES in which all the modes are in their ground state except mode i, which has

1 quantum. To simplify the discussion we only consider one term in Equation (1), which is dominant if HT modes are only slightly displaced, so that overlaps different from $\langle \mathbf{0}_{GS}|\mathbf{0}_{ES}\rangle$ are small [Eq. (3)]:

$$I_n^1 \simeq \frac{|\langle 0_{GS}|0_{ES}\rangle|^2}{2}\left(\frac{\partial\mu}{\partial Q_n}\right)\left(\frac{\partial\mathcal{I}\mathbf{m}}{\partial Q_n}\right) \tag{3}$$

In this approximation, the intensity of fundamental n^1 and its sign are determined by the scalar product of the derivatives of the transition electric and magnetic dipoles. ABS intensities can be easily obtained from Equation (3) by simply substituting $\mathcal{I}\mathbf{m}$ with $\boldsymbol{\mu}$.

We considered the FCHTf|AH calculations. The largest derivatives of $\boldsymbol{\mu}$ are along ES modes 12 (module 0.79 au) and 11 (module 0.57 au), and in fact 12^1 is the strongest ABS band in that frequency region. The modules of the corresponding derivatives of $\mathcal{I}\mathbf{m}$ are 0.0057 au (12) and 0.0095 au (11), which are, respectively, the 20th and 12th in order of decreasing modules. Modes 12 and 11 show the largest scalar products of the derivatives of $\boldsymbol{\mu}$ and $\mathcal{I}\mathbf{m}$, which are −0.00033 and 0.00036 au, respectively, because the angle between the two

118

transition dipoles derivatives is 138° for 12 and 48° for 11. As a consequence 12^1 and 11^1 have ECD intensities of similar magnitude and opposite sign (negative for 12^1, and positive for 11^1).

The relevant modes in AS calculations are GS modes, because ES modes are assumed to be identical to GS modes. For GS modes, we find that the largest derivatives of μ are along GS modes 12 (module 0.85 au) and 11 (module 0.47 au). Therefore, also for the AS results, 12^1 is stronger than 11^1 in ABS. In ECD, the modules of the corresponding derivatives of $\mathcal{I}m$ are 0.0050 au (12) and 0.0140 au (11), which are, respectively the 20th and third in order of decreasing modules. However in this case the angles of the derivatives are very close to 90°, being precisely 92.6° (12) and 90.2° (11), and this explains why the ECD intensity of 12^1 and 11^1 practically vanishes according to AS calculations.

This analysis explains why accounting for Duschinsky mixings improves so remarkably the comparison with experiment. It also suggests that in high-resolution ECD the intensity (and therefore the g value) of the individual vibronic lines can be the result of a subtle balance of many effects, so that different combinations of the same (quasi-degenerate) modes might alter the angles between the vectors of the transition electric and magnetic dipole derivatives and therefore result in strong or very weak ECD activity.

A similar scenario might apply to the ECD intensity of the fundamentals of ES modes 5–8. In fact they also exhibit strong Duschinsky mixings.

Before concluding this section it is worth recalling that Duschinsky mixings have no effect on the sum of the ECD intensities over all the possible vibronic transitions,[13] that is, the integral of the ECD spectrum is equal for FCHTf|AH and FCHTf|AS calculations. On the contrary, here we demonstrated that they can redistribute such intensity over the different vibronic transitions, thus having a drastic impact on high-resolution spectra.

3. Conclusions

In this contribution we computed the absorption and ECD vibronic spectra of (R)-(+)-1-phenylethanol and compared them to high-resolution experimental measurements obtained in jet-cooled conditions. The agreement is fairly satisfactory and allowed us to give a firm assignment of many experimental bands in terms of the involved normal modes and their quanta. Our results highlight that the absolute and relative intensities of the observed bands are strongly affected by HT borrowing mechanisms. In absorption they strongly enhance some transitions and in ECD they cause the appearance of bands with opposite signs. Also, frequency changes and Duschinsky mixings play a relevant role and introduce key improvements for the position and relative intensities of several bands.

We document cases in which the simultaneous comparison of computed and experimental data for both ABS and g anisotropy factors is important to support (or evidence inconsistencies in) the assignments made considering ABS spectra only.

The case of the doublet of bands E1 and E2 with different ABS intensities at around 530 cm^{-1} provides a nice example.[24] Based on ABS data only, they would be assigned, respectively, to the fundamentals of an in-plane ring deformation (mode 12) and an out-of-plane deformation (mode 11), concluding that their order is simply swapped due to inaccuracies in the computed frequencies. The simultaneous analysis of the g values, measured for E2 for the first time in this contribution, provides a different picture. The order seems essentially correct such that E1 has a remarkable contribution from the fundamental of mode 11 and E2 from the fundamental of mode 12, and errors in the relative ABS intensities depend on inaccuracies in the wavefunctions. To support this hypothesis, we showed that by neglecting Duschinsky mixings (which of course modify the ES vibrational wavefunctions) we obtained completely different spectra in the frequency region of E1 and E2, with different absorption intensities and practically no band with a significant positive g value. This analysis indicates that, in this frequency region, the observed intensities are actually determined by a subtle balance of many factors including the exact composition of the normal modes and the vibrational wavefunctions. In this specific case, the inclusion of Duschinsky mixing leads to a net improvement of the agreement with experiment, although a significant error in the relative ABS intensities survives. However, it can be imagined that, in systems of similar complexity, the same subtle balance can result in significant discrepancies with the experimental data. These might be caused, for instance, by perturbations on the final wavefunctions due to inaccuracies in equilibrium geometries or Hessians, or by errors in the transition dipoles. It is also possible that anharmonic corrections on the vibrational wavefunctions play a significant role. For the E1–E2 bands, for instance, possible Fermi resonances could mix states 11^1, 12^1 and 5^2, 6^2, or 7^2. For the latter band, M06-2X actually predicts a significant negative g value (see the Supporting Information). The development of computationally effective, full anharmonic approaches able to correct both the energies and the vibrational wavefunctions appears necessary for a more accurate treatment of these cases.

Conflict of Interest

The authors declare no conflict of interest.

Keywords: Franck–Condon principle · Herzberg–Teller theory · high-resolution spectra · optical anisotropy factors · vibronic calculations

[1] *Computational Strategies for Spectroscopy* (Ed.: V. Barone), Wiley, Chichester, **2012**.

[2] P. L. Polavarapu, *Chiroptical Spectroscopy: Fundamentals and Applications*, CRC, Boca Raton, **2016**.

[3] G. Pescitelli, T. Bruhn, *Chirality* **2016**, *28*, 466.

[4] M. Srebro-Hooper, J. Autschbach, *Annu. Rev. Phys. Chem.* **2017**, *68*, 399.

[5] F. Santoro, D. Jacquemin, *WIREs Comput. Mol. Sci.* **2016**, *6*, 460.

[6] F. Egidi, D. B. Williams-Young, A. Baiardi, J. Bloino, G. Scalmani, M. J. Frisch, L. Xiaosong, V. Barone, *J. Chem. Theory Comput.* **2017**, *13*, 2789.

[7] R. Borrelli, A. Peluso, *J. Chem. Phys.* **2006**, *125*, 194308.

[8] A. Baiardi, J. Bloino, V. Barone, *J. Chem. Phys.* **2016**, *144*, 084114.

[9] J. Cerezo, F. Santoro, *J. Chem. Theory Comput.* **2016**, *12*, 4970.

[10] A. Baiardi, J. Bloino, V. Barone, *J. Chem. Theory Comput.* **2017**, *13*, 2804.

[11] O. E. Weigang, Jr., *J. Chem. Phys.* **1965**, *43*, 3609.

[12] M. Dierksen, S. Grimme, *J. Chem. Phys.* **2006**, *124*, 174301.

[13] a) N. Lin, Y. Luo, F. Santoro, X. Zhao, A. Rizzo, *Chem. Phys. Lett.* **2008**, *464*, 144; b) N. Lin, F. Santoro, X. Zhao, A. Rizzo, V. Barone, *J. Phys. Chem. A*, **2008**, 112, 12401; c) N. Lin, F. Santoro, A. Rizzo, Y. Luo, X. Zhao, V. Barone *J. Phys. Chem. A*, **2009**, 113, 4198.

[14] G. Pescitelli, V. Barone, L. Di Bari, A. Rizzo, F. Santoro, *J. Org. Chem.* **2013**, *78*, 7398.

[15] M. Nooijen, *Int. J. Quantum Chem.* **2006**, *106*, 2489.

[16] A. Baiardi, J. Bloino, V. Barone, *J. Chem. Theory Comput.* **2013**, *9*, 4097.

[17] Y. Liu, J. Cerezo, G. Mazzeo, N. Lin, X. Zhao, G. Longhi, S. Abbate, F. Santoro, *J. Chem. Theory Comput.* **2016**, *12*, 2799.

[18] F. Madeja, M. Havenith, *J. Chem. Phys.* **2002**, *117*, 7162.

[19] J. A. Stearns, C. Seaiby, O. V. Boyarkin, T. R. Rizzo, *Phys. Chem. Chem. Phys.* **2009**, *11*, 125.

[20] Y. Cheng, Y. Liu, *Chin. J. Chem.* **2017**, *35*, 733.

[21] D. W. Arnold, S. E. Bradforth, T. N. Kitsopoulos, D. M. Neumark, *J. Chem. Phys.* **1991**, *95*, 8753.

[22] J. Bloino, M. Biczysko, O. Crescenzi, V. Barone, *J. Chem. Phys.* **2008**, *128*, 244105.

[23] E. Stendardo, F. J. A. Ferrer, F. Santoro, R. Improta, *J. Chem. Theory Comput.* **2012**, *8*, 4483.

[24] J. Lepelmeier, J. L. Alonso-Gomez, F. Mortaheb, U. Boesl, U. Heiz, A. Kartouzian, *Phys. Chem. Chem. Phys.* **2017**, *19*, 21297.

[25] F. Santoro, R. Improta, A. Lami, J. Bloino, V. Barone, *J. Chem. Phys.* **2007**, *126*, 084509.

[26] F. Santoro, V. Barone, *Int. J. Quantum Chem.* **2010**, *110*, 476.

[27] F. Santoro, FCclasses a Fortran 77 code, http://www.pi.iccom.cnr.it/fcclasses, last accessed November 12, 2017.

[28] F. J. A. Ferrer, F. Santoro, *Phys. Chem. Chem. Phys.* **2012**, *14*, 13549.

[29] J. Lepelmeier, K. Titze, A. Kartouzian, U. Boesl, U. Heiz, *ChemPhysChem* **2016**, *17*, 4052.

[30] U. Boesl, A. Kartouzian, *Annu. Rev. Anal. Chem.* **2016**, *9*, 343.

120

7. *Appendix*
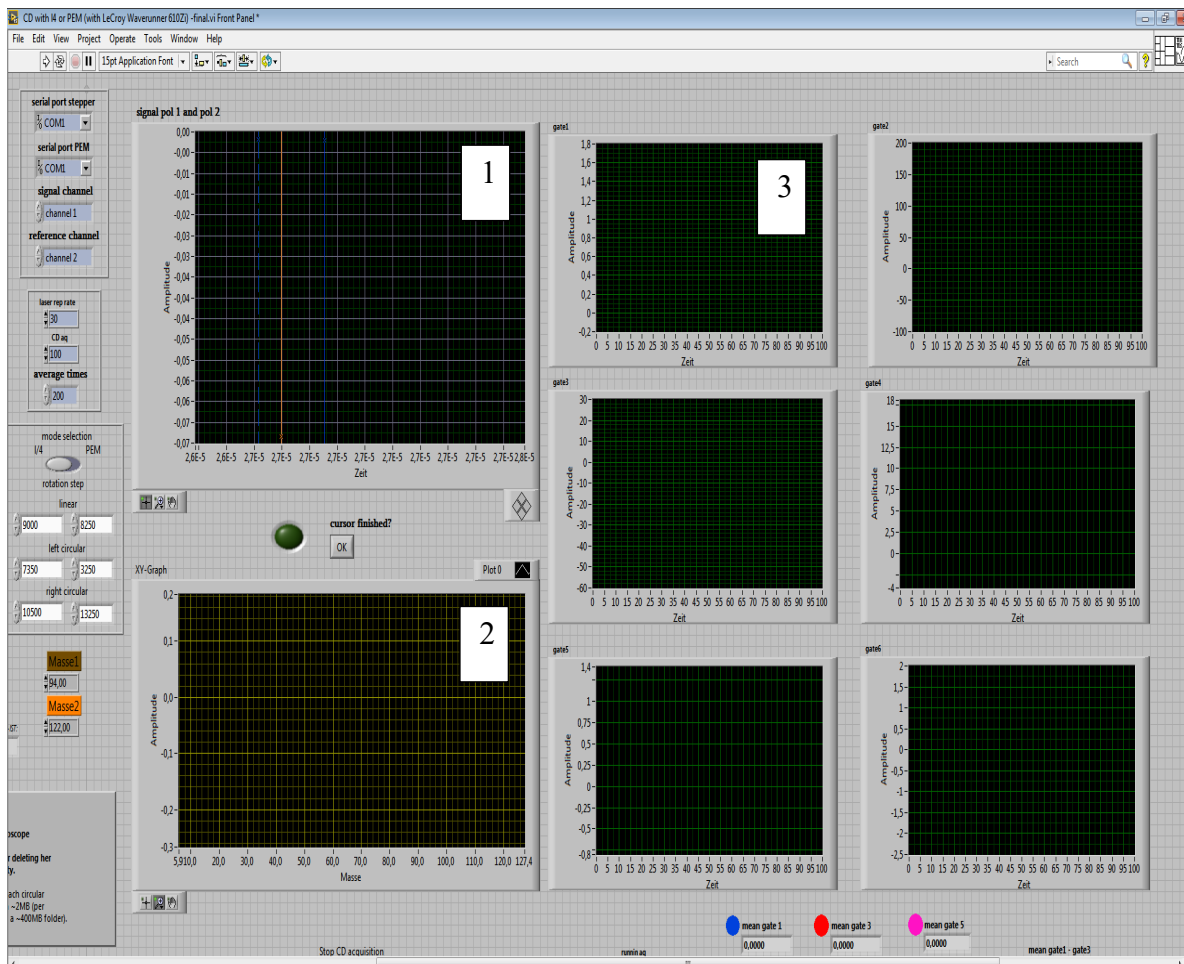
Figure 65- The front panel of the LabView program of CD-REMPI-MS. CD measurements were conducted via this program. The parameters such as repetition rate of the laser, the iteration numbers and number of shots per data point, which are required to conduct the measurements, could be set here. The program also controls the delay time or motor position for the PEM or the QWP, respectively. 1) this window shows the first mass spectrum acquisition, where by the means of cursors one can choose the right mass for the further g-value calculations. 2) this window reports the calibrated mass spectrum based on the defined masses.1 and 2. 3) these windows (gate1,2,3..) show the calculated g-values for the corresponding defined masses.
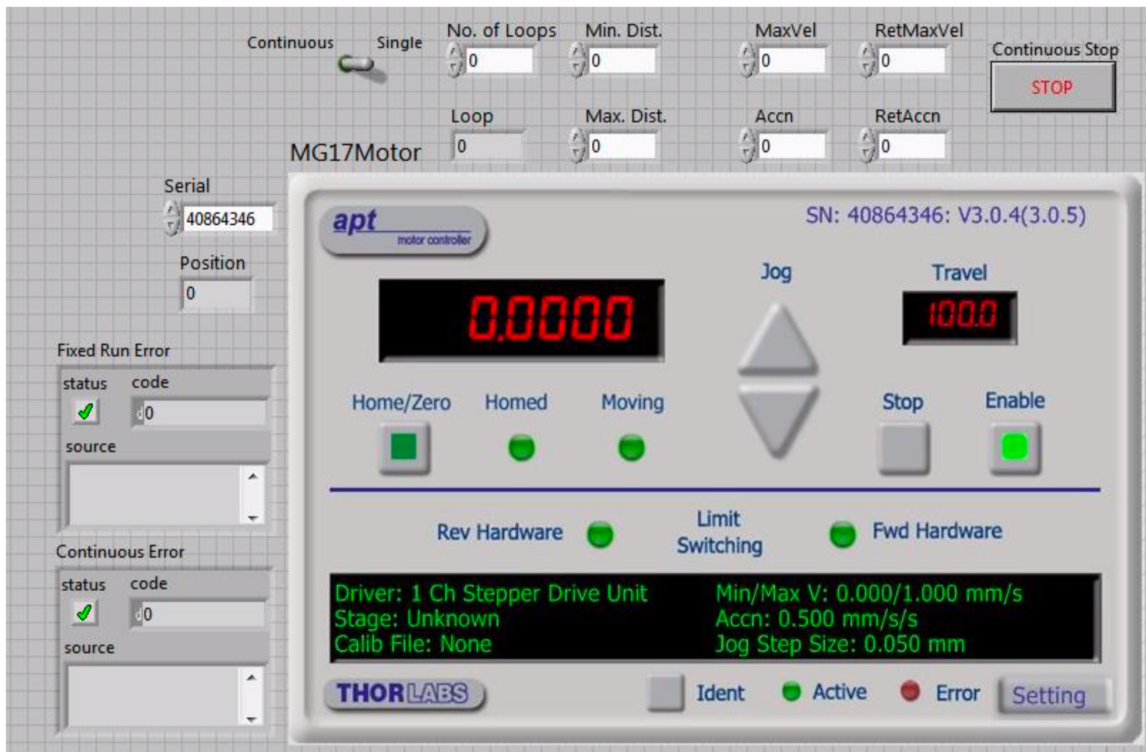
Figure 66- The developed LabView program with the APT software to control the stepper motor. The parameters such as maximum velocity, acceleration, travel distance, number of the loops (in the case of the single mode), the velocity and acceleration for the homing function are regulatable via this program.
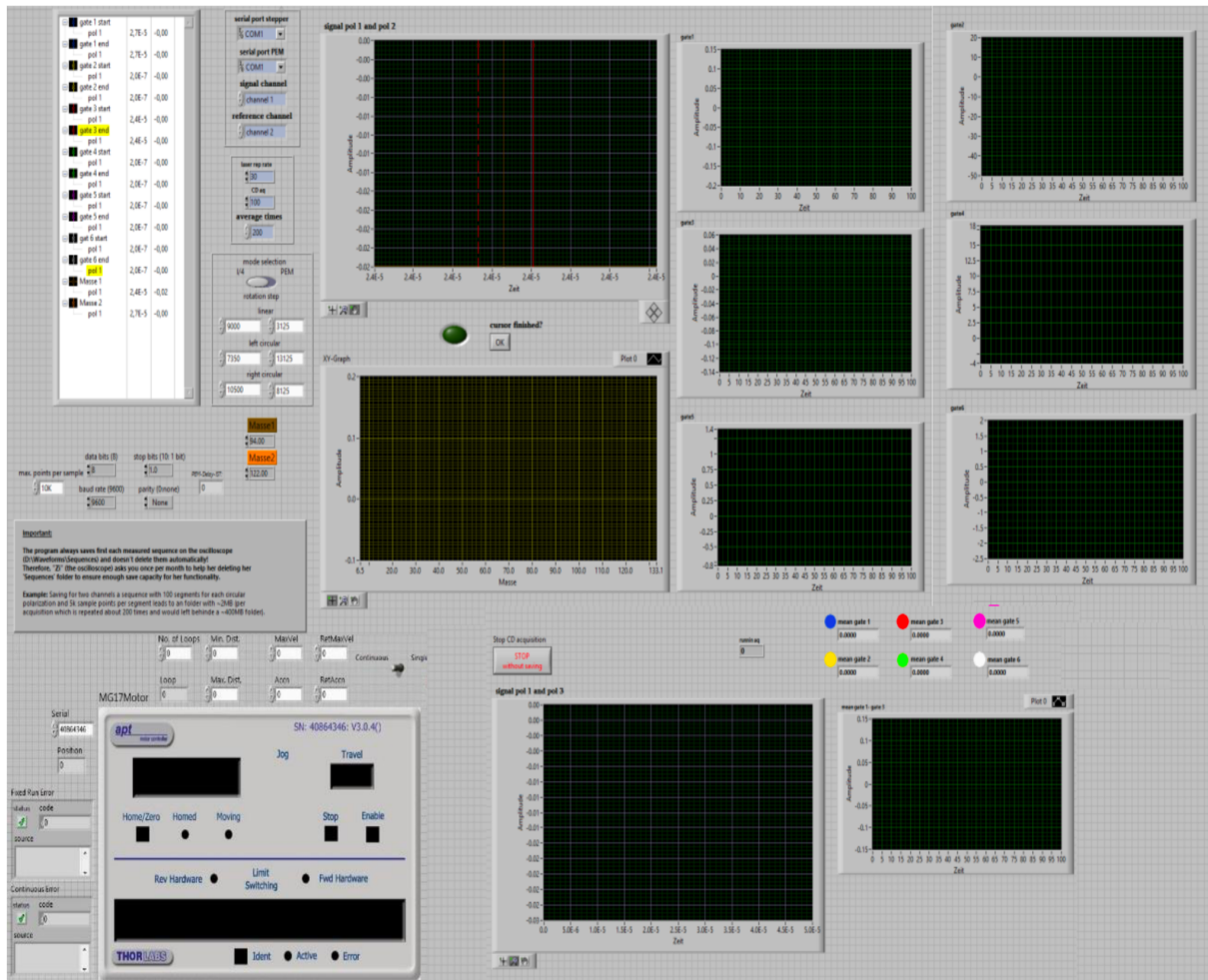
Figure 67- The front panel of the modified LabView program with the implemented program of the motor for CD-REMPI-MS measurement.

This Agreement between Mrs. Farinaz Mortaheb ("You") and John Wiley and Sons ("John Wiley and Sons") consists of your license details and the terms and conditions provided by John Wiley and Sons and Copyright Clearance Center.

|	
License Number	4581430226917
License date	May 03, 2019
Licensed Content Publisher	John Wiley and Sons
Licensed Content Publication	ChemPhysChem
Licensed Content Title	High-Resolution Absorption and Electronic Circular Dichroism Spectra of (R)-( )-1-Phenylethanol. Confident Interpretation Based on the Synergy between Experiments and Computations
Licensed Content Author	Fabrizio Santoro, Farinaz Mortaheb, Jörn Lepelmeier, et al
Licensed Content Date	Feb 16, 2018
Licensed Content Volume	19
Licensed Content Issue	6
Licensed Content Pages	9
Type of use	Dissertation/Thesis
Requestor type	Author of this Wiley article
Format	Print and electronic
Portion	Full article
Will you be translating?	No
Title of your thesis / dissertation	Linear and nonlinear chiroptical activity in the gas phase and at surfaces
Expected completion date	Jun 2019
Expected size (number of pages)	140
Requestor Location	Mrs. Farinaz Mortaheb Lichtenbergstraße 4
	Garching b. Munich, Bavaria 85748 Germany Attn: Mrs. Farinaz Mortaheb
Publisher Tax ID	EU826007151
Total	0.00 EUR

**ELSEVIER LICENSE
TERMS AND CONDITIONS**

May 03, 2019

This Agreement between Mrs. Farinaz Mortaheb ("You") and Elsevier ("Elsevier") consists of your license details and the terms and conditions provided by Elsevier and Copyright Clearance Center.

License Number	4581431413851
License date	May 03, 2019
Licensed Content Publisher	Elsevier
Licensed Content Publication	Chemical Physics Letters
Licensed Content Title	A matrix-free laser desorption method for production of nucleobase clusters and their hydrates
Licensed Content Author	Hiroyuki Saigusa,Azusa Tomioka,Takumi Katayama,Eijiro Iwase
Licensed Content Date	Jan 25, 2006
Licensed Content Volume	418
Licensed Content Issue	1-3
Licensed Content Pages	7
Start Page	119
End Page	125
Type of Use	reuse in a thesis/dissertation
Intended publisher of new work	other
Portion	figures/tables/illustrations
Number of figures/tables/illustrations	1
Format	both print and electronic
Are you the author of this Elsevier article?	No
Will you be translating?	No
Original figure numbers	Figure 1
Title of your thesis/dissertation	Linear and nonlinear chiroptical activity in the gas phase and at surfaces
Expected completion date	Jun 2019
Estimated size (number of pages)	140
Requestor Location	Mrs. Farinaz Mortaheb Lichtenbergstraße 4
	Garching b. Munich, Bavaria 85748 Germany Attn: Mrs. Farinaz Mortaheb
Publisher Tax ID	GB 494 6272 12
Total	0.00 EUR

8. Bibliography

1.   L. A. Nguyen, H. He, C. Pham-Huy, Chiral drugs: an overview. *International journal of biomedical science : IJBS* **2**, 85-100 (2006).

2.   S. W. Smith, Chiral Toxicology: It's the Same Thing…Only Different. *Toxicological Sciences* **110**, 4-30 (2009).

3.   R. Noyori, Asymmetric Catalysis: Science and Opportunities (Nobel Lecture). *Angewandte Chemie International Edition* **41**, 2008-2022 (2002).

4.   A. Zehnacker, M. A. Suhm, Chirality recognition between neutral molecules in the gas phase. *Angewandte Chemie International Edition* **47**, 6970-6992 (2008).

5.   A. Hutt, J. Valentova, The chiral switch: the development of single enantiomer drugs from racemates. *Acta Facultatis Pharmaceuticae Universitatis Comenianae* **50**, 23 (2003).

6.   R. Noyori, *Asymmetric catalysis in organic synthesis*. (1994).

7.   W. S. Knowles, Asymmetric hydrogenation. *Accounts of Chemical Research* **16**, 106-112 (1983).

8.   M. Heitbaum, F. Glorius, I. Escher, Asymmetric heterogeneous catalysis. *Angewandte Chemie International Edition* **45**, 4732-4762 (2006).

9.   M. T. Reetz, K. M. Kühling, H. Hinrichs, A. Deege, Circular dichroism as a detection method in the screening of enantioselective catalysts. *Chirality: The Pharmacological, Biological, and Chemical Consequences of Molecular Asymmetry* **12**, 479-482 (2000).

10.   C. Blons *et al.*, Asymmetric Sequential Cu-Catalyzed 1,6/1,4-Conjugate Additions of Hard Nucleophiles to Cyclic Dienones: Determination of Absolute Configurations and Origins of Enantioselectivity. *Chemistry – A European Journal* **23**, 7515-7525 (2017).

11.   P. Horsch, G. Urbasch, K.-M. Weitzel, Analysis of chirality by femtosecond laser ionization mass spectrometry. *Chirality* **24**, 684-690 (2012).

12.   J. Lepelmeier, K. Titze, A. Kartouzian, U. Boesl, U. Heiz, Mass-selected circular dichroism of supersonic-beam-cooled [D4]-(R)-(+)-3-methylcyclopentanone. *ChemPhysChem* **17**, 4052-4058 (2016).

13.   J. Lepelmeier *et al.*, Chiroptical inversion for isolated vibronic transitions of supersonic beam-cooled molecules. *Physical Chemistry Chemical Physics* **19**, 21297-21303 (2017).

14.   R. J. Cotter, Laser desorption chemical ionization mass spectrometry. *Analytical Chemistry* **52**, 1767-1770 (1980).

15. U. Boesl, J. Grotemeyer, K. Walter, E. W. Schlag, A high-resolution Time-of-Flight Mass Spectrometer with laser desorption and a laser ionization source. *Instrumentation Science & Technology* **16**, 151-171 (1987).

16. M. Karas, F. Hillenkamp, Laser desorption ionization of proteins with molecular masses exceeding 10,000 daltons. *Analytical chemistry* **60**, 2299-2301 (1988).

17. U. Boesl, R. Weinkauf, C. Weickhardt, E. W. Schlag, Laser ion sources for time-of-flight mass spectrometry. *International Journal of Mass Spectrometry and Ion Processes* **131**, 87-124 (1994).

18. D. Burke, D. J. Henderson, Chirality: a blueprint for the future. *British Journal of Anaesthesia* **88**, 563-576 (2002).

19. K.-H. Ernst, Molecular chirality in surface science. *Surface Science* **613**, 1-5 (2013).

20. B. D. Vineyard, W. S. Knowles, M. J. Sabacky, G. L. Bachman, D. J. Weinkauff, Asymmetric hydrogenation. Rhodium chiral bisphosphine catalyst. *Journal of the American Chemical Society* **99**, 5946-5952 (1977).

21. E. Hecht, Optics 2nd edition. *Optics 2nd edition by Eugene Hecht Reading, MA: Addison-Wesley Publishing Company, 1987*, (1987).

22. E. Hecht, *Optics*. (Pearson Education, 2016).

23. N. Berova, K. Nakanishi, R. W. Woody, R. Woody, *Circular dichroism: principles and applications*. (John Wiley & Sons, 2000).

24. A. Rodger, B. Nordén, B. Nordén, *Circular dichroism and linear dichroism*. (Oxford University Press, USA, 1997), vol. 1.

25. R. W. Woody, in *Methods in Enzymology*. (Academic Press, 1995), vol. 246, pp. 34-71.

26. W. Moffitt, Optical rotatory dispersion of helical polymers. *The Journal of Chemical Physics* **25**, 467-478 (1956).

27. T. Petralli-Mallow, T. M. Wong, J. D. Byers, H. I. Yee, J. M. Hicks, Circular dichroism spectroscopy at interfaces: a surface second harmonic generation study. *The Journal of Physical Chemistry* **97**, 1383-1388 (1993).

28. T. Verbiest *et al.*, Nonlinear optical activity and biomolecular chirality. **116**, 9203-9205 (1994).

29. J. D. Byers, H. I. Yee, T. Petralli-Mallow, J. M. Hicks, Second-harmonic generation circular-dichroism spectroscopy from chiral monolayers. *Physical Review B* **49**, 14643-14647 (1994).

30. C. Toro *et al.*, Two-photon absorption circular dichroism: A new twist in nonlinear spectroscopy. **16**, 3504-3509 (2010).

31.   K. Ding, Development of homogeneous and heterogeneous asymmetric catalysts for practical enantioselective reactions. *Pure and applied chemistry* **78**, 293-301 (2006).

32.   M. S. d. Vries, P. Hobza, Gas-phase spectroscopy of biomolecular building blocks. *Annual Review of Physical Chemistry* **58**, 585-612 (2007).

33.   G. Mainfray, G. Manus, Multiphoton ionization of atoms. *Reports on Progress in Physics* **54**, 1333 (1991).

34.   J. H. Gross, *Mass spectrometry: a textbook*. (Springer Science & Business Media, 2006).

35.   M. Guilhaus, Principles and instrumentation in Time-of-flight Mass Spectrometry. *JOURNAL OF MASS SPECTROMETRY* **30**, 1532 (1995).

36.   G. Mainfray, C. Manus, Resonance effects in multiphoton ionization of atoms. *Appl. Opt.* **19**, 3934-3940 (1980).

37.   D. M. Lubman, *Lasers and mass spectrometry*. (Oxford University Press, 1990).

38.   U. Boesl, Multiphoton excitation and mass-selective ion detection for neutral and ion spectroscopy. *The Journal of Physical Chemistry* **95**, 2949-2962 (1991).

39.   T. Streibel, R. Zimmermann, Resonance-enhanced multiphoton ionization mass spectrometry (REMPI-MS): Applications for process analysis. *Annual Review of Analytical Chemistry* **7**, 361-381 (2014).

40.   U. Boesl, A. Kartouzian, Mass-selective chiral analysis. *Annual Review of Analytical Chemistry* **9**, 343-364 (2016).

41.   R. E. Smalley, L. Wharton, D. H. Levy, Molecular optical spectroscopy with supersonic beams and jets. *Accounts of Chemical Research* **10**, 139-145 (1977).

42.   P. S. H. Fitch, L. Wharton, D. H. Levy, The fluorescence excitation spectrum of free base phthalocyanine cooled in a supersonic expansion. *The Journal of Chemical Physics* **69**, 3424-3426 (1978).

43.   D. S. Zakheim, P. M. Johnson, Rate equation modelling of molecular multiphoton ionization dynamics. *Chemical Physics* **46**, 263-272 (1980).

44.   U. Boesl, A. Bornschlegl, C. Logé, K. Titze, Resonance-enhanced multiphoton ionization with circularly polarized light: chiral carbonyls. *Analytical and Bioanalytical Chemistry* **405**, 6913-6924 (2013).

45.   D. M. Lubman, C. T. Rettner, R. N. Zare, How isolated are molecules in a molecular beam? *The Journal of Physical Chemistry* **86**, 1129-1135 (1982).

46.   W. Christen, K. Rademann, U. Even, Supersonic beams at high particle densities: model description beyond the ideal gas approximation. *The Journal of Physical Chemistry A* **114**, 11189-11201 (2010).

47.   L. Valyi, *Atom and ion sources*. (John Wiley and Sons, Ltd, United States, 1977).

48.   A. Amirav, U. Even, J. Jortner, Cooling of large and heavy molecules in seeded supersonic beams. *Chemical Physics* **51**, 31-42 (1980).

49.   W. Kuhn, The physical significance of optical rotatory power. *Transactions of the Faraday Society* **26**, 293-308 (1930).

50.   U. Boesl von Grafenstein, A. Bornschlegl, Circular dichroism laser mass spectrometry: Differentiation of 3-methylcyclopentanone enantiomers. *ChemPhysChem* **7**, 2085-2087 (2006).

51.   R. Li, R. Sullivan, W. Al-Basheer, R. M. Pagni, R. N. Compton, Linear and nonlinear circular dichroism of R-(+)-3-methylcyclopentanone. *The Journal of Chemical Physics* **125**, 144304 (2006).

52.   K. E. Gunde, G. W. Burdicka, F. S. Richardson, Chirality-dependent two-photon absorption probabilities and circular dichroic line strengths: theory, calculation and measurement. *Chemical Physics* **208**, 195-219 (1996).

53.   A. Rizzo, N. Lin, K. Ruud, Ab initio study of the one-and two-photon circular dichroism of R-(+)-3-methyl-cyclopentanone. *The Journal of chemical physics* **128**, 164312 (2008).

54.   N. Lin, Y. Luo, F. Santoro, X. Zhao, A. Rizzo, Vibronically-induced change in the chiral response of molecules revealed by electronic circular dichroism spectroscopy. *Chemical Physics Letters* **464**, 144-149 (2008).

55.   C. Logé, A. Bornschlegl, U. Boesl, Twin mass peak ion source for comparative mass spectrometry: Application to circular dichroism laser MS. *International Journal of Mass Spectrometry* **281**, 134-139 (2009).

56.   C. Logé, A. Bornschlegl, U. Boesl, Progress in circular dichroism laser mass spectrometry. *Analytical and Bioanalytical Chemistry* **395**, 1631 (2009).

57.   C. Logé, U. Boesl, Multiphoton ionization and circular dichroism: New experimental approach and application to natural products. *ChemPhysChem* **12**, 1940-1947 (2011).

58.   C. Loge, U. Boesl, Laser mass spectrometry with circularly polarized light: two-photon circular dichroism. *Physical Chemistry Chemical Physics* **14**, 11981-11989 (2012).

59.   F. E. Hernández, A. Rizzo, Two-photon polarization dependent spectroscopy in chirality: A novel experimental-Theoretical approach to study optically active systems. *Molecules* **16**, 3315-3337 (2011).

60.   F. Gunzer, S. Krüger, J. Grotemeyer, Photoionization and photofragmentation in mass spectrometry with visible and UV lasers. *Mass Spectrometry Reviews* **38**, 202-217 (2019).

61.   C. N. McEwen, B. S. Larsen, Fifty years of desorption ionization of nonvolatile compounds. *International Journal of Mass Spectrometry* **377**, 515-531 (2015).

62.   D. Menzel, in *Interactions on metal surfaces*. (Springer, 1975), pp. 101-142.

63.   N. Teschmit *et al.*, Characterizing and optimizing a laser-desorption molecular beam source. *The Journal of Chemical Physics* **147**, 144204 (2017).

64.   A. Vertes, R. Gijbels, F. Adams, *Laser ionization mass analysis*. (Wiley New York, 1993), vol. 124.

65.   R. F. Haglund, Microscopic and mesoscopic aspects of laser-induced desorption and ablation. *Applied Surface Science* **96-98**, 1-13 (1996).

66.   M. Taherkhani, The University of Manchester (United Kingdom), (2010).

67.   R. B. Hall, S. J. Bares, A. M. DeSantolo, F. Zaera, Pulsed laser-induced desorption studies of the kinetics of ethylene dehydrogenation on Ni(100). *Journal of Vacuum Science & Technology A* **4**, 1493-1498 (1986).

68.   R. B. Hall, Pulsed-laser-induced desorption studies of the kinetics of surface reactions. *The Journal of Physical Chemistry* **91**, 1007-1015 (1987).

69.   P. A. Redhead, Thermal desorption of gases. *Vacuum* **12**, 203-211 (1962).

70.   J. P. Cowin, D. J. Auerbach, C. Becker, L. Wharton, Measurement of fast desorption kinetics of D2, from tungsten by laser induced thermal desorption. *Surface Science* **78**, 545-564 (1978).

71.   G. W. Fabel, S. M. Cox, D. Lichtman, Photodesorption from 304 stainless steel. *Surface Science* **40**, 571-582 (1973).

72.   D. Menzel, R. Gomer, Desorption from metal surfaces by low-energy electrons. **41**, 3311-3328 (1964).

73.   D. Menzel, Desorption induced by electronic transitions: Some recent progress. *Nuclear Instruments and Methods in Physics Research Section B: Beam Interactions with Materials and Atoms* **13**, 507-517 (1986).

74.   R. O. Adams, E. E. Donaldson, Photodesorption. **42**, 770-774 (1965).

75.   P. R. Antoniewicz, Model for electron- and photon-stimulated desorption. *Physical Review B* **21**, 3811-3815 (1980).

76.   T. J. Chuang, Laser-induced gas-surface interactions. *Surface Science Reports* **3**, 1-105 (1983).

77.   J. D. Horvath, A. J. Gellman, Enantiospecific desorption of R- and S-Propylene oxide from a chiral Cu(643) surface. *Journal of the American Chemical Society* **123**, 7953-7954 (2001).

78.   I. Ali, H. Y. Aboul-Enein, *Chiral separations by liquid chromatography and related technologies*. (CRC Press, 2003).

79. B. S. Sekhon, Enantioseparation of chiral drugs—an overview. *Int J Pharm Technol Res* **2**, 1584-1594 (2010).

80. S. Andersson, S. G. Allenmark, Preparative chiral chromatographic resolution of enantiomers in drug discovery. *Journal of Biochemical and Biophysical Methods* **54**, 11-23 (2002).

81. T. Toyo'oka, Resolution of chiral drugs by liquid chromatography based upon diastereomer formation with chiral derivatization reagents. *Journal of Biochemical and Biophysical Methods* **54**, 25-56 (2002).

82. Y. Shen, Surface studies by optical second harmonic generation: An overview. *Journal of Vacuum Science & Technology B: Microelectronics Processing and Phenomena* **3**, 1464-1466 (1985).

83. Y. R. Shen, Surface properties probed by second-harmonic and sum-frequency generation. *Nature* **337**, 519-525 (1989).

84. Y. R. Shen, Optical Second Harmonic Generation at Interfaces. **40**, 327-350 (1989).

85. S. Mukamel, *Principles of nonlinear optical spectroscopy*. (Oxford university press New York, 1995), vol. 29.

86. L. Schneider, W. Peukert, Second harmonic generation spectroscopy as a method for in situ and online characterization of particle surface properties. **23**, 351-359 (2006).

87. N. Bloembergen, P. S. Pershan, Light waves at the boundary of nonlinear media. *Physical Review* **128**, 606-622 (1962).

88. W. Jang, Second harmonic generation study of photodynamics and adsorption/desorption on rutile TiO surfaces. (1994).

89. J. Dadap, T. Heinz, Lasers in physics: Second-harmonic spectroscopy.

90. X. Zhu, T. Rasing, Y. J. C. P. L. Shen, Laser-induced thermal desorption of CO on Ni (111): Determination of pre-exponential factor and heat of desorption. **155**, 459-462 (1989).

91. M. Kauranen, T. Verbiest, J. J. Maki, A. Persoons, Second-harmonic generation from chiral surfaces. *The Journal of Chemical Physics* **101**, 8193-8199 (1994).

92. J. J. Maki, M. Kauranen, A. Persoons, Surface second-harmonic generation from chiral materials. *Physical Review B* **51**, 1425-1434 (1995).

93. T. P. Petralli-Mallow, A. L. Plant, M. L. Lewis, J. M. Hicks, Cytochrome c at model membrane surfaces: exploration via second harmonic generation-circular dichroism and surface-enhanced resonance raman spectroscopy. *Langmuir* **16**, 5960-5966 (2000).

94. J. M. Hicks, T. Petralli-Mallow, Nonlinear optics of chiral surface systems. *Applied Physics B* **68**, 589-593 (1999).

95. V. Vogel, What do nonlinear optical techniques have to offer the biosciences? *Current Opinion in Colloid & Interface Science* **1**, 257-263 (1996).

96. G. J. Simpson, Structural origins of circular dichroism in surface second harmonic generation. *The Journal of Chemical Physics* **117**, 3398-3410 (2002).

97. D. C. Hooper *et al.*, Strong rotational anisotropies affect nonlinear chiral metamaterials. *Advanced Materials* **29**, 1605110 (2017).

98. W. C. Wiley, I. H. McLaren, Time-of-Flight Mass Spectrometer with improved resolution. *Review of Scientific Instruments* **26**, 1150-1157 (1955).

99. C. Q. Jiao, D. R. A. Ranatunga, W. E. Vaughn, B. S. Freiser, A pulsed-leak valve for use with ion trapping mass spectrometers. *Journal of the American Society for Mass Spectrometry* **7**, 118-122 (1996).

100. L. Abad, D. Bermejo, V. J. Herrero, J. Santos, I. Tanarro, Performance of a solenoid-driven pulsed molecular-beam source. *Review of Scientific Instruments* **66**, 3826-3832 (1995).

101. B. Mamyrin, V. Karataev, D. Shmikk, V. Zagulin, The massreflect ron, a new non-magnetic time-of-flight mass spectrometer with high resolution. *Zh. Eksp. Teor. Fiz* **64**, 82-89 (1973).

102. U. Boesl, Time-of-flight mass spectrometry: Introduction to the basics. **36**, 86-109 (2017).

103. M. Graus, M. Müller, A. Hansel, High resolution PTR-TOF: Quantification and formula confirmation of VOC in real time. *Journal of the American Society for Mass Spectrometry* **21**, 1037-1044 (2010).

104. J. L. Wiza, Microchannel plate detectors. *Nucl. Instrum. Methods* **162**, 587-601 (1979).

105. G. Montaudo, M. S. Montaudo, C. Puglisi, F. Samperi, Determination of absolute mass values in MALDI-TOF of polymeric materials by a method of self-calibration of the spectra. *Analytical Chemistry* **66**, 4366-4369 (1994).

106. F. Drewnick *et al.*, A new Time-of-Flight Aerosol Mass Spectrometer (TOF-AMS)—Instrument description and first field deployment. *Aerosol Science and Technology* **39**, 637-658 (2005).

107. C. B. Moore, *Chemical and biochemical applications of lasers.* (Elsevier, 2012), vol. 1.

108. E. Hecht, Optics 4th edition. *Optics, 4th Edition, Addison Wesley Longman Inc, 1998*, (1998).

109. G. Meijer, M. S. de Vries, H. E. Hunziker, H. R. J. A. P. B. Wendt, Laser desorption jet-cooling of organic molecules. **51**, 395-403 (1990).

110. E. Alonso-Gil, Technical university of Munich, Technical university of Munich (2015).

132

111. F. Piuzzi, I. Dimicoli, M. Mons, B. Tardivel, Q. Zhao, A simple laser vaporization source for thermally fragile molecules coupled to a supersonic expansion: application to the spectroscopy of tryptophan. *Chemical Physics Letters* **320**, 282-288 (2000).

112. H. Saigusa, A. Tomioka, T. Katayama, E. Iwase, A matrix-free laser desorption method for production of nucleobase clusters and their hydrates. *Chemical Physics Letters* **418**, 119-125 (2006).

113. J. Zhang, L. Pei, W. Kong, Zero kinetic energy photoelectron spectroscopy of tetracene using laser desorption for vaporization. *The Journal of Chemical Physics* **128**, 104301 (2008).

114. D. E. Powers, S. G. Hansen, M. E. Geusic, D. L. Michalopoulos, R. E. Smalley, Supersonic copper clusters. *The Journal of Chemical Physics* **78**, 2866-2881 (1983).

115. S. Maruyama, L. R. Anderson, R. E. Smalley, Direct injection supersonic cluster beam source for FT-ICR studies of clusters. *Review of Scientific Instruments* **61**, 3686-3693 (1990).

116. M. Taherkhani, M. Riese, M. BenYezzar, K. Müller-Dethlefs, A novel experimental system of high stability and lifetime for the laser-desorption of biomolecules. **81**, 063101 (2010).

117. Y. W. T. Ryan, "Automation of a laser desorption apparatus," (Department of chemistry, Chair of physical chemistry, Technical University of Munich, 2019).

118. P. F. Moulton, Spectroscopic and laser characteristics of Ti:Al2O3. *J. Opt. Soc. Am. B* **3**, 125-133 (1986).

119. U. Megerle, I. Pugliesi, C. Schriever, C. F. Sailer, E. Riedle, Sub-50 fs broadband absorption spectroscopy with tunable excitation: putting the analysis of ultrafast molecular dynamics on solid ground. *Applied Physics B* **96**, 215-231 (2009).

120. A. von Weber, M. Jakob, E. Kratzer, A. Kartouzian, U. Heiz, In situ second-harmonic generation circular dichroism with submonolayer sensitivity. *ChemPhysChem* **20**, 134-141 (2019).

121. M. Cervantes, Brewster angle prisms: a review. *Optics & Laser Technology* **20**, 297-300 (1988).

122. Y. Zhou *et al.*, Occurrence of glycosidically conjugated 1-phenylethanol and its hydrolase β-Primeverosidase in tea (Camellia sinensis) flowers. *Journal of Agricultural and Food Chemistry* **62**, 8042-8050 (2014).

123. G. A. Burdock, *Fenaroli's handbook of flavor ingredients*. (CRC press, 2016).

124. H. Yun, Y.-H. Yang, B.-K. Cho, B.-Y. Hwang, B.-G. Kim, Simultaneous synthesis of enantiomerically pure (R)-1-phenylethanol and (R)-α-methylbenzylamine from racemic α-methylbenzylamine using ω-transaminase/alcohol dehydrogenase/glucose dehydrogenase coupling reaction. *Biotechnology letters* **25**, 809-814 (2003).

125. A. G. Guidoni *et al.*, Chirality and intermolecular forces: studies using R2PI experiments in supersonic beams. *Physical Chemistry Chemical Physics* **2**, 4139-4142 (2000).

126. K. Shin-ya *et al.*, Absolute configuration and conformation analysis of 1-phenylethanol by matrix-isolation infrared and vibrational circular dichroism spectroscopy combined with density functional theory calculation. *The Journal of Physical Chemistry A* **111**, 8598-8605 (2007).

127. N. M. M. Nibbering, T. J. De Boer, Mass spectometry of aralkyl compounds with a functional group—VI1: Mass spectra of 1-phenylethyanol-1, 2-phenylethanol-1 and 1-phenylpropanol-2. *Organic Mass Spectrometry* **1**, 365-390 (1968).

128. M. A. Duncan, T. G. Dietz, R. E. Smalley, Efficient multiphoton ionization of metal carbonyls cooled in a pulsed supersonic beam. *Chemical Physics* **44**, 415-419 (1979).

129. T. R. Rizzo, Y. D. Park, L. Peteanu, D. H. Levy, Electronic spectrum of the amino acid tryptophan cooled in a supersonic molecular beam. *The Journal of chemical physics* **83**, 4819-4820 (1985).

130. F. Madeja, M. Havenith, High resolution spectroscopy of carboxylic acid in the gas phase: observation of proton transfer in (DCOOH) 2. *The Journal of chemical physics* **117**, 7162-7168 (2002).

131. J. A. Stearns, C. Seaiby, O. V. Boyarkin, T. R. Rizzo, Spectroscopy and conformational preferences of gas-phase helices. *Physical Chemistry Chemical Physics* **11**, 125-132 (2009).

132. Y. Cheng, Y. Liu, Theoretical simulation of the vibrationally resolved UV absorption spectrum of acryloyl fluoride. *Chinese Journal of Chemistry* **35**, 733-741 (2017).

133. D. W. Arnold, S. Bradforth, T. Kitsopoulos, D. M. Neumark, Vibrationally resolved spectra of C2–C11 by anion photoelectron spectroscopy. *The Journal of chemical physics* **95**, 8753-8764 (1991).

134. J. Bloino, M. Biczysko, O. Crescenzi, V. Barone, Integrated computational approach to vibrationally resolved electronic spectra: Anisole as a test case. *The Journal of chemical physics* **128**, 244105 (2008).

135. E. Stendardo, F. Avila Ferrer, F. Santoro, R. Improta, Vibrationally resolved absorption and emission spectra of dithiophene in the gas phase and in solution by first-principle quantum mechanical calculations. *Journal of chemical theory and computation* **8**, 4483-4493 (2012).

136. F. Santoro *et al.*, High-resolution absorption and electronic circular dichroism spectra of (R)-(+)-1-phenylethanol. Confident interpretation based on the synergy between experiments and computations. *ChemPhysChem* **19**, 715-723 (2018).

137. S. L. Chin, Multiphoton ionization of molecules. *Physical Review A* **4**, 992-996 (1971).

138. M. Posthumus, P. Kistemaker, H. Meuzelaar, M. Ten Noever de Brauw, Laser desorption-mass spectrometry of polar nonvolatile bio-organic molecules. *Analytical Chemistry* **50**, 985-991 (1978).

139. R. B. Van Breemen, M. Snow, R. J. Cotter, Time-resolved laser desorption mass spectrometry. I. Desorption of preformed ions. *International Journal of Mass Spectrometry and Ion Physics* **49**, 35-50 (1983).

140. J. Grotemeyer, U. Boesl, K. Walter, E. W. Schlag, A general soft ionization method for mass spectrometry: Resonance-enhanced multi-photon ionization of biomolecules. *Organic Mass Spectrometry* **21**, 645-653 (1986).

141. R. Tembreull, D. M. Lubman, Pulsed laser desorption with resonant two-photon ionization detection in supersonic beam mass spectrometry. *Analytical Chemistry* **58**, 1299-1303 (1986).

142. X. Ni, X. Li, Z. Li, J.-P. Cheng, Equilibrium acidities of BINOL type chiral phenolic hydrogen bonding donors in DMSO. *Organic Chemistry Frontiers* **3**, 1154-1158 (2016).

143. L. Pu, 1,1'-Binaphthyl dimers, oligomers, and polymers: Molecular recognition, asymmetric catalysis, and new materials. *Chemical Reviews* **98**, 2405-2494 (1998).

144. J. D. Byers, J. M. Hicks, Electronic spectral effects on chiral surface second harmonic generation. *Chemical physics letters* **231**, 216-224 (1994).

145. I. Hanazaki, H. Akimoto, Optical rotatory power of 2, 2'-dihydroxy-1, 1'-binaphthyl and related compounds. *Journal of the American Chemical Society* **94**, 4102-4106 (1972).

146. C. Toro *et al.*, Two-photon absorption circular-linear dichroism on axial enantiomers. *Chirality* **22**, E202-E210 (2010).

147. G. R. Kinsel, J. Lindner, J. Grotemeyer, E. W. Schlag, Absorption effects in laser desorption of neutral organic molecules. *The Journal of Physical Chemistry* **95**, 7824-7830 (1991).

148. J. D. Horvath, A. J. Gellman, Enantiospecific desorption of chiral compounds from chiral Cu(643) and achiral Cu(111) surfaces. *Journal of the American Chemical Society* **124**, 2384-2392 (2002).

149. E. R. Francotte, Enantioselective chromatography as a powerful alternative for the preparation of drug enantiomers. *Journal of Chromatography A* **906**, 379-397 (2001).

150. I. Ali, H. Y. Aboul-Enein, A. Ghanem, Enantioselective toxicity and carcinogenesis. *Current Pharmaceutical Analysis* **1**, 109-125 (2005).

151. X. He *et al.*, Enantioselective effects of o, p′-DDT on cell invasion and adhesion of breast cancer cells: chirality in cancer development. *Environmental science & technology* **49**, 10028-10037 (2015).

152. A. A. Basheer, Chemical chiral pollution: impact on the society and science and need of the regulations in the 21st century. *Chirality* **30**, 402-406 (2018).

153. M. Karas, D. Bachmann, U. Bahr, F. Hillenkamp, Matrix-assisted ultraviolet laser desorption of non-volatile compounds. *International journal of mass spectrometry and ion processes* **78**, 53-68 (1987).

154. K. Tanaka *et al.*, Protein and polymer analyses up to m/z 100 000 by laser ionization time-of-flight mass spectrometry. *Rapid communications in mass spectrometry* **2**, 151-153 (1988).

155. Y. R. Shen, Surface studies by optical second harmonic generation: An overview. *Journal of Vacuum Science & Technology B: Microelectronics Processing and Phenomena* **3**, 1464-1466 (1985).

156. Y. R. Shen, Surfaces probed by nonlinear optics. *Surface Science* **299-300**, 551-562 (1994).

157. J. E. Sipe, V. Mizrahi, G. I. Stegeman, Fundamental difficulty in the use of second-harmonic generation as a strictly surface probe. *Physical Review B* **35**, 9091-9094 (1987).

158. J. M. Hicks, L. E. Urbach, E. W. Plummer, H.-L. Dai, Can pulsed laser excitation of surfaces be described by a Ttermal model? *Physical Review Letters* **61**, 2588-2591 (1988).

159. J. D. Byers, H. I. Yee, J. M. Hicks, A second harmonic generation analog of optical rotatory dispersion for the study of chiral monolayers. *The Journal of Chemical Physics* **101**, 6233-6241 (1994).

160. P. Heister *et al.*, Orientational changes of supported chiral 2, 2′-dihydroxy-1, 1′ binaphthyl molecules. *Physical Chemistry Chemical Physics* **16**, 7299-7306 (2014).

161. A. Ozcelik *et al.*, Device-Compatible Chiroptical Surfaces through Self-Assembly of Enantiopure Allenes. *Langmuir* **34**, 4548-4553 (2018).

162. S. Guy *et al.*, Chiral organic thin films: How far pulsed laser deposition can conserve chirality. *Thin Solid Films* **520**, 6440-6445 (2012).

163. A. von Weber *et al.*, Circular dichroism and isotropy – polarity reversal of ellipticity in molecular films of 1,1'-Bi-2-Naphtol. *ChemPhysChem* **20**, 62-69 (2019).

164. M. A. Kriech, J. C. Conboy, Using the intrinsic chirality of a molecule as a label-free probe to detect molecular adsorption to a surface by second harmonic generation. *Appl. Spectrosc.* **59**, 746-753 (2005).

165. A. Hong *et al.*, Isomer-Specific Induced Circular Dichroism Spectroscopy of Jet-Cooled Phenol Complexes with (−)-Methyl l-Lactate. *The journal of physical chemistry letters* **9**, 476-480 (2018).